UNIVERSITÄT
BAYREUTH

Controlled fabrication of microfibers using microfluidic devices

DISSERTATION

zur Erlangung des akademischen Grades
eines Doktors der Naturwissenschaften (Dr. rer. nat.)
an der Fakultät für Biologie, Chemie und Geowissenschaften
der Universität Bayreuth

vorgelegt von

Ron Eddie Hofmann

aus Coburg

Bayreuth, 2020

Die vorliegende Arbeit wurde in der Zeit von November 2013 bis November 2019 in Bayreuth am Lehrstuhl für Physikalische Chemie I unter Betreuung von Herrn Professor Dr. Stephan Förster angefertigt.

Vollständiger Abdruck der von der Fakultät für Biologie, Chemie und Geowissenschaften der Universität Bayreuth genehmigten Dissertation zur Erlangung des akademischen Grades eines Doktors der Naturwissenschaften (Dr. rer. nat.).

Dissertation eingereicht am: 25.11.2019

Zulassung durch die Promotionskommission: 04.12.2019

Wissenschaftliches Kolloquium: 14.09.2020

Amtierender Dekan: Prof. Dr. Matthias Breuning

Prüfungsausschuss:

Prof. Dr. Stephan Förster   (Gutachter)
Prof. Dr. Markus Retsch   (Gutachter)
Prof. Dr. Seema Agarwal   (Vorsitz)
Prof. Dr. Stephan Gekle

Für meine Familie

Table of Contents

Abbreviations and Symbols

Abbreviations

μSBS	microfluidic solution blow spinning
μTAS	micro-total-analysis system
2D	two-dimensional
2PP	two-photon polymerization
3D	three-dimensional
ABS	acrylonitrile butadiene styrene
ATR	attenuated total reflection
BSA	bovine serum albumin
CAD	computer-aided design
CNC	computer numerical control
COC	cyclic olefin copolymer
CROP	cationic ring-opening polymerization
DLP	digital light projector
DMEM	Dulbecco's Modified Eagle's Medium
DMF	N,N-dimethylformamide
DMF	digital microfluidics
DMSO	dimethyl sulfoxide
DSC	differential scanning calorimetry
ESI	electronic supplementary information
FDM	fused deposition modeling
FEM	finite element method
FTIR	Fourier transform infrared spectroscopy
GBL	γ-butyrolactone
GDVN	gas dynamic virtual nozzle
GISAXS	grazing-incidence small-angle X-ray scattering
HFIP	hexafluoroisopropanol
HFP	hexafluoropropylene
I.D.	inner diameter
i3DP	inkjet 3D printing
LOC	lab-on-a-chip
MC	main channel
MEMS	microelectromechanical systems
MPS	microphysiological systems

NMP	N-methyl-2-pyrrolidone
O.D.	outer diameter
PA	polyamide
PBS	phosphate buffered saline
PC	polycarbonate
PCL	poly(caprolactone)
PDMS	poly(dimethylsiloxane)
PEEK	polyether ether ketone
PEG	polyethylene glycol
PET	poly(ethylene terephthalate)
PFA	paraformaldehyde
PGMEA	propylene glycol methyl ether acetate
PLA	poly(lactic acid)
PMMA	poly(methyl methacrylate)
PP	polypropylene
PPS	poly(phenylene sulfide)
PS	polystyrene
PTFE	poly(tetrafluoroethylene)
PVDF	poly(vinylidene fluoride)
RMS	root mean square (quadratic mean)
SAXS	small-angle X-ray scattering
SBS	solution blow spinning
SC	side channel
SD	standard deviation
SEM	scanning electron microscopy
SLA	stereolithography
STL	standard triangulation language
SU-8	negative photoresist containing EPON SU-8
TES	2-[(2-Hydroxy-1,1-bis(hydroxymethyl)ethyl)amino]-ethane-sulfonic acid
TFE	tetrafluoroethylene
TGA	thermogravimetric analysis
THV	fluoroplastic terpolymer THV 221 (3M Dyneon)
USAXS	ultra-small-angle X-ray scattering
UV	ultraviolet
VDF	vinylidene fluoride
WAXS	wide-angle X-ray scattering
XRD	X-ray diffraction

Symbols

c_w	air channel width
a_l	aperture length
a_w	aperture width
l	characteristic length
f_{AD}	correction factor
f_{BC}	correction factor
f_J	correction factor
A	cross-sectional area
De	Deborah number
d_f	diameter of the free fiber
d_j	diameter of the jet
d_{spool}	diameter of the spool
d_s	diameter of the spooled fiber
η	dynamic viscosity
$\Delta\rho$	electron density difference
t_{evap}	evaporation time
ε	extensibility / strain
$\dot{\varepsilon}$	extensional rate
$P(\mathbf{q})$	form factor
$\mathbf{F}_\eta$	friction force
$\mathbf{f}_\eta$	frictional force density
R	gas constant (R = 8.314 J/K·mol)
g	gravitational acceleration constant (g = 9.81 m/s^2)
$\mathbf{F}_g$	gravitational force
$\mathbf{f}_g$	gravitational force density
h_n	height of the channel
a	lamellar spacing
l_f	length of fiber
ρ	mass density
D	mass diffusion coefficient
∇	nabla operator
n_h	nozzle height
n_w	nozzle width
S	orientational order parameter
Pe	Péclet number

Δp	pressure difference
$\mathbf{F}_p$	pressure force
$\mathbf{f}_p$	pressure force density
f_j	proportionality factor
τ_p	relaxation time
Re	Reynolds number
v_{spool}	rotational frequency (cycles per second)
$I(\mathbf{q})$	scattering intensity
$\mathbf{q}$	scattering vector
$\dot{\gamma}$	shear rate
e_j	specific energy inside jet
e_n	specific energy inside nozzle
v_s	spooling rotational velocity / drawing speed
σ	strength / stress
$S(\mathbf{q})$	structure factor
T	temperature
t	time
τ_{flow}	time scale of the process
v_n	velocity inside the nozzle
v_f	velocity of the fiber
v_j	velocity of the jet
V	volume
ϕ_C	volume fraction of the cylinders
ϕ_D	volume fraction of the disks
ϕ_T	volume fraction of THV
V_f	volume of fiber
V_j	volume of jet
V_0	volume of polymer solution
V_T	volume of THV
Q	volumetric flow rate
Q^*	volumetric flow rate after evaporation of the solvent
$\mathbf{k}_0$	wave vector in incident direction
$\mathbf{k}_s$	wave vector of scattered wave
Wi	Weissenberg number
w_n	width of the channel
d_s	working distance
E	Young's modulus

List of Publications

This thesis is based on publications [1], [2] and [3], that are adapted as chapters 4, 5 and 6:

[1]   Christian Haynl, <u>Eddie Hofmann</u>, Kiran Pawar, Stephan Förster, Thomas Scheibel*
"*Microfluidics-Produced Collagen Fibers Show Extraordinary Mechanical Properties*"
Nano Lett., 2016, **16**, 5917–5922.

[2]   <u>Eddie Hofmann</u>, Kilian Krüger, Christian Haynl, Thomas Scheibel, Martin Trebbin, Stephan Förster*
"*Microfluidic nozzle device for ultrafine fiber solution blow spinning with precise diameter control*"
Lab Chip, 2018, **18**, 2225–2234.

[3]   <u>Eddie Hofmann</u>, Kilian Krüger, Martin Dulle, Xiaojian Liao, Andreas Greiner, Stephan Förster*
"*Controlling polymer microfiber structure by micro solution blow spinning*"
Macromol. Chem. Phys., 2020, **221**, 1900453.

Further publications that were prepared in collaboration with fellow scientists and are not part of this thesis:

[4]   Mathias Schlenk, <u>Eddie Hofmann</u>, Susanne Seibt, Sabine Rosenfeldt, Lukas Schrack, Markus Drechsler, Andre Rothkirch, Wiebke Ohm, Josef Breu, Stephan Gekle, Stephan Förster*
"*Parallel and Perpendicular Alignment of Anisotropic Particles in Free Liquid Microjets and Emerging Microdroplets*"
Langmuir, 2018, **34**, 4843−4851.

[5]   Maria Herbst, <u>Eddie Hofmann</u>, Stephan Förster*
"*Nucleation and growth kinetics of ZnO nanoparticles studied by in situ microfluidic SAXS/WAXS/UV-Vis-experiments*"
Langmuir, 2019, **35**, 11702−11709.

[6]   Alessandro Jager, <u>Eddie Hofmann</u>, Mathias Schlenk, Eliezer Jager, Ewa Pavlova, Jiri Panek, Petr Stepanek, Stephan Förster*
        "New insights in the production of polymer nanoparticles by hydrodynamic flow focusing nanoprecipitation using microfluidic devices"
        to be submitted

[7]   Claudia S. Wagner, Andrea Fortini, <u>Eddie Hofmann</u>, Thomas Lunkenbein, Matthias Schmidt, Alexander Wittemann*
        "*Particle nanosomes with tailored silhouettes*"
        Soft Matter, 2012, **8**, 1928–1933.

Summary

Microfibers are of great interest in a wide variety of research fields because of their high surface-area-to-volume ratio and unique mechanical properties. Accordingly, they are basis of diverse applications in tissue engineering, biomedicine, filtration, and sensor technology. The multidisciplinary field of microfluidics deals with the behavior and manipulation of fluids confined to such small dimensions that surface forces, energy dissipation, and diffusive mixing start to dominate the system. Microfluidics has already proven its potential in various research areas such as modern medicine, biology and chemistry.
The scope of this thesis is to explore the options, select suitable approaches and exhaust the possibilities of utilizing microfluidic devices for spinning of microfibers. Microfluidics offers some key advantages associated with laminar flow and provide unique control over the entire spinning process.

Two different methods of conventional fiber spinning were identified and adapted for microfluidic spinning of microfibers. Both approaches, which are variants of wet and dry spinning, have in common that a spinning solution of a natural or synthetic polymer is ejected through a spinneret. When the solvent is removed or exchanged by the surrounding medium, this causes the polymer to solidify and form a mechanically stable fiber. The macromolecules are aligned within the nozzle by shear and elongational forces. When collecting the fiber on a rotating spool, the mechanical properties can be further enhanced by additional stretching.

Microfluidics offers a high degree of control of all relevant spinning parameters and the possibility to optimize the nozzle design. Computer-aided design software allows to design almost any channel geometry, which can be created using lithographic techniques. This allows not only to fabricate fibers of uniform diameter and endless length in a steady and controlled process, but also to gain insights on the formation of fibrous microstructure by applying suitable characterization methods.

Collagen microfibers are in the focus of biomedical research projects. In this thesis it could be shown that microfibers can be produced from pure type I collagen in a microfluidic wet spinning process using hydrodynamic flow focusing and an asymmetric channel architecture. Irreversible clogging of the channels by the assembling collagen could be prevented by reducing wall adhesion with an elaborate channel geometry, which ultimately results in a continuous and adjustable process. These microfluidically produced collagen fibers stand out due to their exceptional small diameter, while their tensile strength and

Young's modulus exceed that of classical wet-spun fibers and even natural tendon. Cell culture tests showed directional axon growth of neuronal NG108-15 cells along the microfiber axis, which qualifies these fibers for a potential application in peripheral nerve repair.

The second approach for microfluidic fiber spinning is a special variant of dry spinning, which is called micro solution blow spinning (μSBS). Here, the spinneret is replaced by a microfluidic nozzle device, which allows to produce ultrafine fibers of virtual endless length having precise diameter control. The gas dynamic virtual nozzle (GDVN) principle is applied to generate a fine liquid jet by three-dimensional air focusing of the spinning solution. When the polymer solution is ejected from the nozzle, the solvent evaporates, and the solid polymer fiber remains. The ejected fibers can either be sprayed directly onto a substrate as a nonwoven mesh or collected on a rotating spool as filament yarn. From hydrodynamic considerations and mass balance, equations were derived which allow to quantitatively predict and control the diameter of the jetted polymer solution and the resulting fiber.

In the last part of this thesis, micro solution blow spinning is combined with small- and wide-angle X-ray scattering (SAXS, WAXS) to directly relate the macroscopic spinning conditions to the molecular structure of the resulting fibers. Having precise control of the jet diameter and velocity also gives excellent control of the fiber diameter and the internal macromolecular alignment. Using the software *Scatter*, 2D-SAXS patterns were simulated and compared with the measured ones to determine the orientational order parameter. It was shown that the elongation rate is the decisive parameter that transduces the macroscopic flow properties to the local macromolecular structure and orientation and thus determines the mechanical properties of the resulting fiber. The well-defined shish–kebab crystal structure of the fluorinated terpolymer THV transforms into an extended chain crystal structure upon plastic deformation in tensile tests.

In summary, this thesis contributes to the methodical advancement of microfluidic devices for the purpose of spinning microfibers and the fundamental understanding of structure formation in the process of fiber spinning.

Zusammenfassung

Mikrofasern sind aufgrund ihres hohen Oberflächen-Volumen-Verhältnisses und ihrer einzigartigen mechanischen Eigenschaften für eine Vielzahl von Forschungsgebieten von großem Interesse. Folglich bilden sie die Basis für verschiedenartige Anwendungen in den Bereichen der Gewebetechnik, Biomedizin, Filtration und Sensorik.

Das multidisziplinäre Feld der Mikrofluidik beschäftigt sich mit dem Verhalten und der Manipulation von Fluiden, die auf so kleine Dimensionen beschränkt sind, dass Oberflächenkräfte, Energiedissipation und diffusive Vermischung das System dominieren. Die Mikrofluidik konnte ihr Potenzial bereits in verschiedenen Forschungsbereichen wie der modernen Medizin, der Biologie und der Chemie beweisen.

Die vorliegende Arbeit beschäftigt sich damit, die Optionen zu erforschen, geeignete Ansätze auszuwählen und die Möglichkeiten auszuschöpfen, wie Mikrofluidiksysteme für das Spinnen von Mikrofasern genutzt werden können. Die Mikrofluidik bietet einige entscheidende Vorteile, die mit der laminaren Strömung einhergehen und eine einzigartige Kontrolle über den gesamten Spinnprozess ermöglichen.

Zwei verschiedene Methoden des konventionellen Faserspinnens wurden identifiziert und für das mikrofluidische Spinnen von Mikrofasern angepasst. Diese beiden Ansätze, die Varianten des Nass- und Trockenspinnens sind, haben gemeinsam, dass eine Spinnlösung eines natürlichen oder synthetischen Polymers durch eine Spinndüse ausgestoßen wird. Sobald das Lösungsmittel entfernt oder durch das umgebende Medium ausgetauscht wird, verfestigt sich das Polymer und bildet eine mechanisch stabile Faser. Die Makromoleküle richten sich durch Scher- und Dehnungskräfte innerhalb der Düse aus. Die mechanischen Eigenschaften können durch zusätzliches Strecken der Faser bei der Aufnahme auf einer rotierenden Spule weiter verbessert werden.

Die Mikrofluidik bietet ein hohes Maß an Kontrolle über alle relevanten Spinnparameter und die Möglichkeit das Düsendesign zu optimieren. Computergestützte Konstruktionssoftware ermöglicht es, fast beliebige Kanalgeometrien zu entwerfen und diese mit Hilfe von lithografischen Techniken herzustellen. So können nicht nur Fasern mit gleichmäßigem Durchmesser und endloser Länge in einem kontinuierlichen und kontrollierten Prozess hergestellt werden, sondern durch geeignete Charakterisierungsmethoden auch Erkenntnisse über die Bildung von Mikrostrukturen in Fasern gewonnen werden.

Kollagen-Mikrofasern stehen im Mittelpunkt biomedizinischer Forschungsvorhaben. Es konnte in dieser Arbeit gezeigt werden, dass Mikrofasern aus reinem Typ-I-Kollagen in einem mikrofluidischen Nassspinnverfahren unter Verwendung hydrodynamischer Strömungsfokussierung und einer asymmetrischen Kanalarchitektur hergestellt werden können. Irreversibles Zusetzen der Kanäle durch sich verfestigendes Kollagen konnte verhindert werden, indem mit einer durchdachten Kanalgeometrie die Wandanhaftungen reduziert wurden, was letztendlich zu einem kontinuierlichen und steuerbaren Prozess führte. Diese mikrofluidisch-erzeugten Kollagenfasern zeichnen sich durch ihren außergewöhnlich kleinen Durchmesser aus, wobei ihre Zugfestigkeit und ihr Elastizitätsmodul die entsprechenden Werte klassisch hergestellter Nassspinnfasern und sogar die der natürlichen Sehnen übertreffen. Zellkulturversuche zeigten ein gerichtetes Axonwachstum neuronaler NG108-15-Zellen entlang der Mikrofaserachse, was diese Fasern für eine mögliche Anwendung bei der Reparatur peripherer Nerven qualifiziert.

Der zweite Ansatz für mikrofluidisches Faserspinnen ist eine spezielle Variante des Trockenspinnens, das als Mikrolösungsblasspinnverfahren (engl. *micro solution blow spinning*, µSBS) bezeichnet wird. Hierbei wird als Spinndüse ein mikrofluidischer Düsenchip verwendet, der es erlaubt, ultrafeine Endlosfasern unter präziser Steuerung des Durchmessers herzustellen. Das Prinzip der gasdynamischen virtuellen Düse (engl. *gas dynamic virtual nozzle*, GDVN) wird angewendet, um einen feinen Flüssigkeitsstrahl der Spinnlösung durch dreidimensionale Luftfokussierung zu erzeugen. Sobald die Polymerlösung aus der Düse ausgestoßen wird, verdunstet das Lösungsmittel und eine stabile Polymerfaser bleibt zurück. Die ausgestoßenen Fasern können entweder direkt als Vliesstoff auf ein Substrat aufgesprüht oder als Filamentgarn auf einer rotierenden Spule aufgefangen werden. Aus hydrodynamischen Überlegungen und der Massenbilanz konnten Gleichungen abgeleitet werden, die es ermöglichen, den Durchmesser des Polymerlösungsstrahls und den Durchmesser der resultierenden Faser quantitativ vorherzusagen und zu steuern.

Im letzten Teil dieser Arbeit wird das Mikrolösungsblasspinnverfahren mit Klein- und Weitwinkel-Röntgenstreuung (SAXS, WAXS) kombiniert, um die makroskopischen Spinnbedingungen unmittelbar mit der Molekularstruktur der resultierenden Fasern in Beziehung zu setzen. Die präzise Steuerung des Strahldurchmessers und der Strahlgeschwindigkeit ermöglicht es ebenfalls eine ausgezeichnete Kontrolle auf den Faserdurchmesser und die interne makromolekulare Ausrichtung auszuüben. Mit Hilfe der Software *Scatter* wurden zweidimensionale SAXS-Streubilder simuliert und mit den gemessenen Streubildern verglichen, um den Orientierungsordnungsparameter zu bestimmen. Es konnte gezeigt werden, dass die Dehnungsrate der ausschlaggebende Parameter ist, der die makroskopischen Fließeigenschaften in die lokale Struktur und

Orientierung der Makromoleküle überträgt und damit die mechanischen Eigenschaften der resultierenden Faser bestimmt. Die gut definierte Schaschlikspieß-Kristallstruktur (engl. *shish–kebab crystal structure*) des Fluorterpolymers THV wandelt sich im Zugversuch durch plastische Verformung zu einer gestrecktkettigen Kristallstruktur (engl. *extended chain crystal structure*) um.

Zusammenfassend lässt sich sagen, dass diese Arbeit zur systematischen Weiter-entwicklung von Mikrofluidik-Chips für das Spinnen von Mikrofasern und zum grund-legenden Verständnis der Strukturbildung im Faserspinnprozess beiträgt.

1 Introduction

1.1 Introduction to microfluidics

Microfluidics deals with the behavior of fluids on the sub-millimeter scale and manipulates them in a targeted and precise manner. It is a cross-disciplinary field at the intersection of microengineering, chemistry, physics, nanotechnology, biochemistry, and biotechnology.[1] A characteristic of microfluidic devices or flow configurations is that at least one dimension is in the micrometer range.[2] For most cases, the standard continuum description of transport processes is suited for flows of small molecule liquids.[2] However, surface effects that often can be neglected at the macro-scale become increasingly dominant in microfluidics as size is diminished.[1,2] Typically, the flow at small Reynolds numbers is laminar in microfluidic devices and diffusive mixing is prevalent as turbulences and eddies are absent.[3,4]

Since molecular diffusion is quite slow on a larger length scale, mixing in microchannels can be enhanced by active or passive micromixers.[5,6] Active micromixers improve the mixing performance by applying external forces to the sample flows to accelerate the diffusion process, while passive micromixers increase the contact area and contact time between the different mixing species.[7]

There are several ways to manipulate liquids in microfluidic configurations, for example by pressure gradients, capillary effects, electric fields, magnetic fields, centrifugal forces, and acoustic streaming.[6,8–12] Forces can be can be applied macroscopically by external fields, or can be generated locally within the microchannel by integrated components.[6]

The rise of microfluidics began in the early 1990s as an advancement from microelectro-mechanical systems (MEMS), since many of the patterning techniques used in silicon-based microelectronics industry could be transferred to the manufacture of microfluidic devices.[1] These devices were not limited to electronical and mechanical parts, but could also handle fluids by including channels, valves, pumps, filters, separators, and mixers.[6]

In the following years, silicon and glass got replaced by elastomeric or thermoplastic materials for most applications.[2] Poly(dimethylsiloxane) (PDMS) became one of the standard materials, as soft-lithographic methods, based on rapid prototyping and replica molding, provide faster and less expensive routes than the conventional etching methods for glass and silicon.[13–16]

Researchers were driven by the vision of entire chemical laboratories on the surface of silicon or polymer chips.[1] These lab-on-a-chip devices (LOC) or micro-total-analysis systems (μTAS) integrate one or several laboratory functions on a single chip of a few square centimeters to achieve automation and high-throughput screening.[17–19] Lab-on-a-

chip device should take care of all lab processes for analysis, but should also integrate pre- and post-treatment steps, including additional cleaning and separation steps. Typical advantages are the small sample quantities required, the routine operation by untrained personnel, and compactness of the system, which allows for transportability and massive parallelization.[4]

A recent application of microfluidics with high potential are organ-, body-, and disease-on-a-chip systems, which are also known as microphysiological systems (MPS).[20] Analogous to lab-on-a-chip systems, different functions are integrated in a microfabricated device and form a complex system, in this case to simulate special tasks of tissue, complete human organs or even multi-organ systems.[20] So far, organ-on-a-chip devices have been presented, which, for example, imitate functions of heart,[21] lung,[22] eye,[23] kidney,[24] stomach,[25] gut,[26] or skin.[27] These devices incorporate cell cultures, membranes and sensors to create physiologically based pharmacokinetic model systems.[20] One major goal is to improve the drug development process and toxicity studies by determining drug efficacy and safety in advance of clinical testing.[28] This could help to select which compounds enter clinical trials and thereby increasing significantly the chances that a drug will successfully exit clinical trials as an approved drug.[20]

Microfluidic devices can even be used for educational purposes, as its applicability for performing acid-base titrations by undergraduate students in university analytical chemistry laboratories has been demonstrated.[29]

There are different subcategories of microfluidics. Three of the most common are explained in further detail, which are continuous-flow microfluidics, droplet-based microfluidics,[30] and paper-based microfluidics.[31]

Continuous-flow microfluidics rely on the control of a steady state liquid flow and can be used for the synthesis of nanoparticles and liposomes, or the separation of microparticles, cells and DNA.[32–34] In the steady state, each position in the channel corresponds to a certain reaction time, which allows to study nucleation and growth kinetics by performing in-situ measurements.[34,35] Due to the well-defined flow conditions, continuous-flow microfluidics is also used in this thesis to produce microfibers, while having precise control over the fiber diameter.[36,37]

In contrast, droplet-based microfluidics manipulates discrete volumes of fluids in immiscible phases. This is more like a batch process, as each individual droplet can be used as a reaction vessel, which is generated first, then mixed, optionally fused, stored, analyzed and even sorted afterwards. This technology is also known as digital microfluidics (DMF).[30,38]

The goal behind paper-based microfluidics is to fabricate inexpensive, lightweight, and user-friendly medical diagnostic devices.[31] The sample is transported along the chip by capillary forces caused by the porous structure between the cellulose fibers of the paper-

based substrate. Current applications include glucose, protein and Escherichia coli detection.[31,39,40]

Several advantages of microfluidics arise from scaling down standard laboratory setups by the factor of 1000 or more, and make microfluidics an emerging and rapidly evolving field.[1] As only small amounts of sample are required, which can be expensive, difficult to access or even hazardous, less waste is generated as well.[41] Mass production and commercialization can lead to lower fabrication costs and allow the use of cost-effective disposable chips.[42] Microfluidics offers fast analysis and response times due to short diffusion distances and high surface-volume-ratios. The thermal control in microfluidic devices is excellent, as heat transfer is fast and heat capacities are small.[41] Magnetic and electric fields are more effective at short distance, making compact and portable microfluidic systems ideal for applications as sensors and detectors.

The objective of this thesis is to use microfluidics with all its advantages for the spinning of microfibers, that have plenty of applications in tissue engineering, drug delivery, guided cell culture, and as wound dressing.[43–46] Continuous-flow microfluidics is eminently suited to fabricate fibers of virtual endless length, when a steady state has formed. Hydrodynamic flow focusing offers defined conditions regarding concentration and shear forces in the microchannel, which can easily be adjusted and optimized for fiber spinning. Additionally, the formation of fibrous microstructure can be studied by applying suitable methods like X-ray scattering. Two spinning methods, based on dry and wet spinning, will be presented in this work, which shows the potential of microfluidic fiber spinning.

1.2 References

1   H. Bruus, *Theoretical microfluidics*, Oxford Univ. Press, Oxford, 2011, vol. 18.

2   H. A. Stone and S. Kim, *AIChE Journal*, 2001, **47**, 1250–1254.

3   T. M. Squires and S. R. Quake, *Rev. Mod. Phys.*, 2005, **77**, 977–1026.

4   G. M. Whitesides, *Nature*, 2006, **442**, 368–373.

5   Y. K. Suh and S. Kang, *Micromachines*, 2010, **1**, 82–111.

6   H. A. Stone, A. D. Stroock and A. Ajdari, *Annual Review of Fluid Mechanics*, 2004, **36**, 381–411.

7   C.-Y. Lee, C.-L. Chang, Y.-N. Wang and L.-M. Fu, *International journal of molecular sciences*, 2011, **12**, 3263–3287.

8   M. G. Pollack, R. B. Fair and A. D. Shenderov, *Appl. Phys. Lett.*, 2000, **77**, 1725–1726.

9   H. H. Bau, J. Zhong and M. Yi, *Sensors and Actuators B: Chemical*, 2001, **79**, 207–215.

10   R. D. Johnson, I. H. Badr, G. Barrett, S. Lai, Y. Lu, M. J. Madou and L. G. Bachas, *Analytical chemistry*, 2001, **73**, 3940–3946.

11   M. Amasia, M. Cozzens and M. J. Madou, *Sensors and Actuators B: Chemical*, 2012, **161**, 1191–1197.

12   D. Mark, S. Haeberle, G. Roth, F. von Stetten and R. Zengerle, *Chemical Society reviews*, 2010, **39**, 1153–1182.

13   J. C. McDonald, D. C. Duffy, J. R. Anderson, D. T. Chiu, H. Wu, O. J. A. Schueller and G. M. Whitesides, *Electrophoresis*, 2000, 27–40.

14   Y. Xia and G. M. Whitesides, *Annu. Rev. Mater. Sci.*, 1998, **28**, 153–184.

15   Y. Xia and G. M. Whitesides, *Angewandte Chemie International Edition*, 1998, **37**, 550–575.

16   J. C. McDonald and G. M. Whitesides, *Acc. Chem. Res.*, 2002, **35**, 491–499.

17   A. Manz, N. Graber and H. M. Widmer, *Sensors and Actuators B: Chemical*, 1990, **1**, 244–248.

18   N. Convery and N. Gadegaard, *Micro and Nano Engineering*, 2019, **2**, 76–91.

19   L. R. Volpatti and A. K. Yetisen, *Trends in biotechnology*, 2014, **32**, 347–350.

20   M. L. Shuler, *Lab on a chip*, 2018, **19**, 9–10.

21   A. Agarwal, J. A. Goss, A. Cho, M. L. McCain and K. K. Parker, *Lab on a chip*, 2013, **13**, 3599–3608.

22   D. D. Huh, *Annals of the American Thoracic Society*, 2015, **12 Suppl 1**, S42-4.

23   D. Bennet, Z. Estlack, T. Reid and J. Kim, *Lab on a chip*, 2018, **18**, 1539–1551.

24   J. Lee and S. Kim, *Current drug metabolism*, 2018, **19**, 577–583.

25   K. K. Lee, H. A. McCauley, T. R. Broda, M. J. Kofron, J. M. Wells and C. I. Hong, *Lab on a chip*, 2018, **18**, 3079–3085.

26   R. Villenave, S. Q. Wales, T. Hamkins-Indik, E. Papafragkou, J. C. Weaver, T. C. Ferrante, A. Bahinski, C. A. Elkins, M. Kulka and D. E. Ingber, *PloS one*, 2017, **12**, e0169412.

27   G. Sriram, M. Alberti, Y. Dancik, B. Wu, R. Wu, Z. Feng, S. Ramasamy, P. L. Bigliardi, M. Bigliardi-Qi and Z. Wang, *Materials Today*, 2018, **21**, 326–340.

28   B. Zhang and M. Radisic, *Lab on a chip*, 2017, **17**, 2395–2420.

29   J. Greener, E. Tumarkin, M. Debono, A. P. Dicks and E. Kumacheva, *Lab on a chip*, 2012, **12**, 696–701.

30   S.-Y. Teh, R. Lin, L.-H. Hung and A. P. Lee, *Lab on a chip*, 2008, **8**, 198–220.

31   A. W. Martinez, S. T. Phillips and G. M. Whitesides, *PNAS*, 2008, **105**, 19606–19611.

32   A. Jahn, J. E. Reiner, W. N. Vreeland, D. L. DeVoe, L. E. Locascio and M. Gaitan, *J Nanopart Res*, 2008, **10**, 925–934.

33   N. Pamme, *Lab on a chip*, 2007, **7**, 1644–1659.

34   M. Herbst, E. Hofmann and S. Förster, *Langmuir*, 2019, **35**, 11702–11709.

35   S. Seibt, S. With, A. Bernet, H.-W. Schmidt and S. Förster, *Langmuir: the ACS journal of surfaces and colloids*, 2018, **34**, 5535–5544.

36   E. Hofmann, K. Krüger, C. Haynl, T. Scheibel, M. Trebbin and S. Förster, *Lab on a chip*, 2018, **18**, 2225–2234.

37   C. Haynl, E. Hofmann, K. Pawar, S. Förster and T. Scheibel, *Nano letters*, 2016, **16**, 5917–5922.

38   S. L. S. Freire, *Sensors and Actuators A: Physical*, 2016, **250**, 15–28.

39   T. S. Park and J.-Y. Yoon, *IEEE Sensors J.*, 2015, **15**, 1902–1907.

40   A. W. Martinez, S. T. Phillips, M. J. Butte and G. M. Whitesides, *Angewandte Chemie (International ed. in English)*, 2007, **46**, 1318–1320.

41   R. M. Guijt, A. Dodge, G. W. K. van Dedem, N. F. de Rooij and E. Verpoorte, *Lab on a chip*, 2003, **3**, 1–4.

42   R. S. Pawell, D. W. Inglis, T. J. Barber and R. A. Taylor, *Biomicrofluidics*, 2013, **7**, 56501.

43   A. S. Hoffman, *Advanced Drug Delivery Reviews*, 2002, **54**, 3–12.

44   F. Sharifi, A. C. Sooriyarachchi, H. Altural, R. Montazami, M. N. Rylander and N. Hashemi, *ACS Biomater. Sci. Eng.*, 2016, **2**, 1411–1431.

45   R. Vasita and D. S. Katti, *International journal of nanomedicine*, 2006, **1**, 15–30.

46   C. M. Hwang, Y. Park, J. Y. Park, K. Lee, K. Sun, A. Khademhosseini and S. H. Lee, *Biomedical microdevices*, 2009, **11**, 739–746.

2 Fundamentals

2.1 Hydrodynamic fundamentals for microfluidics

2.1.1 Navier-Stokes equation

The Navier-Stokes equation is the central relationship of fluid dynamics and describes the motion of a viscous fluid. The solution of the Navier-Stokes equation gives a vector field of the flow velocity, which assigns to every point in a fluid at any moment in time a vector whose direction and magnitude correspond to the velocity of the fluid at that point in space and at that moment in time.

The Navier-Stokes equation is based on the assumption that a fluid is a continuous material rather than discrete particles. Furthermore, all fields of interest are differentiable, which are namely pressure, density, flow velocity and temperature.

The Navier-Stokes equation can be described as the continuum version of Newton's second law of motion on a per unit volume basis.[1]

$$\mathbf{F} = m \cdot \mathbf{a} \tag{1}$$

Due to the continuum hypothesis, the mass m becomes the density ρ of the volume element and the force $\mathbf{F}$ changes to the force density $\mathbf{f}$.[2]

$$\frac{\mathbf{F}}{V} = \mathbf{f} = \frac{m}{V} \cdot \mathbf{a} = \rho \cdot \frac{d\mathbf{v}}{dt} \tag{2}$$

As acceleration $\mathbf{a}$ is defined as the derivative of velocity $\mathbf{v}$ with respect to time t, the force density $\mathbf{f}$ can be expressed as:

$$\mathbf{f} = \rho \cdot \frac{d\mathbf{v}}{dt} = \rho \cdot \frac{d}{dt} \mathbf{v}(x(t), y(t), z(t), t) \tag{3}$$

The velocity $\mathbf{v}(x(t), y(t), z(t), t)$ of the fluid is a function of time and space, whereby the x-, y- and z-coordinates themselves change over time. Accordingly, the total derivative of the velocity can be described by the total differential, which is the sum of the partial differentials with respect to all the independent variables:[2]

$$\mathbf{f} = \rho \left(\frac{\partial \mathbf{v}}{\partial x}\bigg|_{y,z,t} \frac{dx}{dt} + \frac{\partial \mathbf{v}}{\partial y}\bigg|_{x,z,t} \frac{dy}{dt} + \frac{\partial \mathbf{v}}{\partial z}\bigg|_{x,y,t} \frac{dz}{dt} + \frac{\partial \mathbf{v}}{\partial t}\bigg|_{x,y,z} \right) \tag{4}$$

The derivative of x with respect to t is the velocity in x-direction v_x, respectively v_y for the derivative of y, and v_z for the derivative of z.

$$\mathbf{f} = \rho \left(\frac{\partial \mathbf{v}}{\partial x}\bigg|_{y,z,t} v_x + \frac{\partial \mathbf{v}}{\partial y}\bigg|_{x,z,t} v_y + \frac{\partial \mathbf{v}}{\partial z}\bigg|_{x,y,t} v_z + \frac{\partial \mathbf{v}}{\partial t}\bigg|_{x,y,z} \right) \tag{5}$$

The acceleration term in eq. (5) can be written as

$$\mathbf{f} = \rho \frac{d\mathbf{v}}{dt} = \rho \left((\mathbf{v} \cdot \nabla)\mathbf{v} + \frac{\partial \mathbf{v}}{\partial t} \right) \tag{6}$$

by applying the nabla operator, whose definition is given in eq. (7).[2]

$$\nabla = \left(\frac{\partial}{\partial x}, \frac{\partial}{\partial y}, \frac{\partial}{\partial z} \right) = \mathbf{e_1} \frac{\partial}{\partial x} + \mathbf{e_2} \frac{\partial}{\partial y} + \mathbf{e_3} \frac{\partial}{\partial z} \tag{7}$$

When rewriting the term $\mathbf{v} \cdot \nabla$ as in eqs. (8-10), the connection between eq. (5) and eq. (6) becomes apparent:

$$\mathbf{v} \cdot \nabla = \mathbf{v} \cdot \mathbf{e_1} \frac{\partial}{\partial x} + \mathbf{v} \cdot \mathbf{e_2} \frac{\partial}{\partial y} + \mathbf{v} \cdot \mathbf{e_3} \frac{\partial}{\partial z} \tag{8}$$

$$\mathbf{v} \cdot \nabla = \begin{pmatrix} v_x \\ v_y \\ v_z \end{pmatrix} \cdot \begin{pmatrix} 1 \\ 0 \\ 0 \end{pmatrix} \frac{\partial}{\partial x} + \begin{pmatrix} v_x \\ v_y \\ v_z \end{pmatrix} \cdot \begin{pmatrix} 0 \\ 1 \\ 0 \end{pmatrix} \frac{\partial}{\partial y} + \begin{pmatrix} v_x \\ v_y \\ v_z \end{pmatrix} \cdot \begin{pmatrix} 0 \\ 0 \\ 1 \end{pmatrix} \frac{\partial}{\partial z} \tag{9}$$

$$\mathbf{v} \cdot \nabla = v_x \frac{\partial}{\partial x} + v_y \frac{\partial}{\partial y} + v_z \frac{\partial}{\partial z} \tag{10}$$
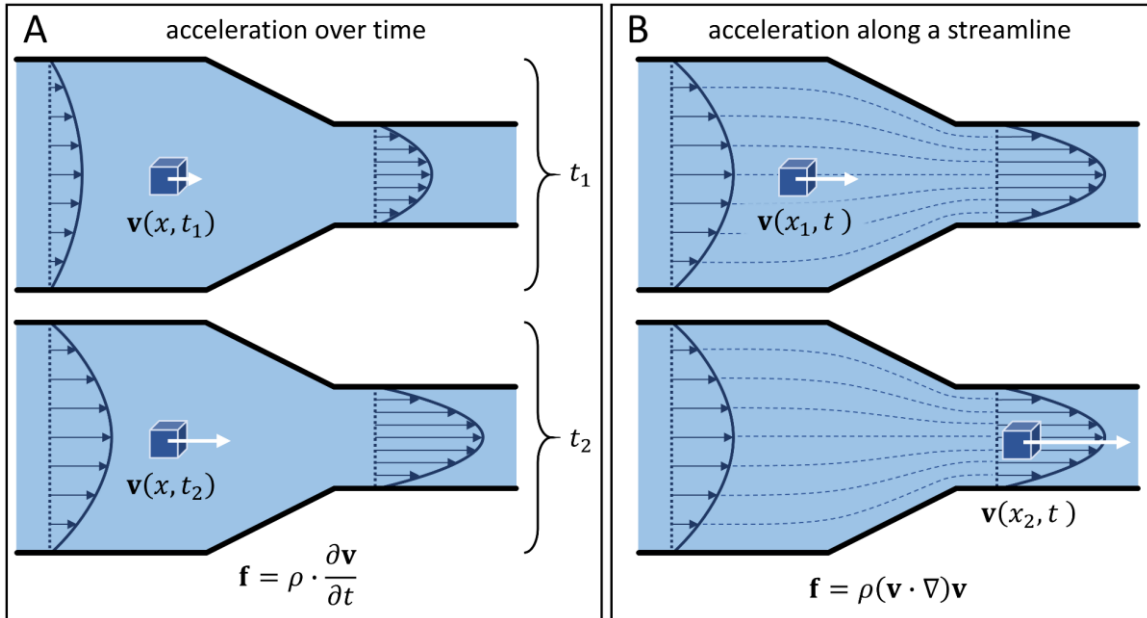

Figure 1: The change of momentum of a fluid element can be based on (A) the acceleration over time at a given location or on (B) the acceleration along a streamline due to the changing cross-section of the channel. This illustration shows a simplified version of the three-dimensional reality as just one dimension is considered (x-direction).

The acceleration term of eq. (6) can be divided into two parts, which are illustrated in Fig. 1: $\rho \cdot \partial \mathbf{v} / \partial t$ describes the acceleration over time and $\rho(\mathbf{v} \cdot \nabla)\mathbf{v}$ describes the acceleration along a streamline due to mass conservation.

The change of momentum of each infinitesimal volume element is caused by different forces, acting either on the surface or on the whole volume of the fluid element. The vector of the surface forces can either point orthogonally on the surface of the volume element or parallel to the plane of the surface.

The force which acts in normal direction on the surface of the volume element dV is the pressure force $\mathbf{F}_p$:[2]

$$\mathbf{f}_p = \frac{d\mathbf{F}_p}{dV} = -\nabla p \tag{11}$$

Additionally, a tangential force arises from the fluid sheets sliding past each other. This friction force $\mathbf{F}_\eta$ is caused by the viscosity η of the fluid and damps the motion of the fluid:[2]

$$\mathbf{f}_\eta = \frac{d\mathbf{F}_\eta}{dV} = \eta \nabla^2 \mathbf{v} \tag{12}$$

The forces, which act on the volume itself, are the body forces like the centrifugal force, the electrostatic force or the gravitational force $\mathbf{F}_g$. Usually, only the gravitational force $\mathbf{F}_g$ is considered in the Navier-Stokes equation:[2]

$$\mathbf{f}_g = \frac{d\mathbf{F}_g}{dV} = \rho \mathbf{g} \tag{13}$$

The force density $\mathbf{f}$ in the Navier-Stokes equation is the sum of all mentioned individual force densities (pressure $\mathbf{f}_p$, friction $\mathbf{f}_\eta$, gravitation $\mathbf{f}_g$):

$$\mathbf{f} = \mathbf{f}_p + \mathbf{f}_\eta + \mathbf{f}_g \tag{14}$$

This leads to the Navier-Stokes equation for incompressible fluids:[2,3]

$$\rho \left((\mathbf{v} \cdot \nabla)\mathbf{v} + \frac{\partial \mathbf{v}}{\partial t} \right) = -\nabla p + \eta \nabla^2 \mathbf{v} + \rho \mathbf{g} \tag{15}$$

The inertial acceleration terms are described by the left-hand part of the equation and the right-hand side summarizes the forces acting on the fluid.

Some simplifications to the Navier-Stokes equation can be made in microfluidics, as the inertial forces are usually small compared to the viscous forces and the nonlinear term can be neglected, which results in the time-dependent linear Stokes equation:[4,5]

$$\rho \frac{\partial \mathbf{v}}{\partial t} = -\nabla p + \eta \nabla^2 \mathbf{v} + \rho \mathbf{g} \tag{16}$$

When a steady state has developed, the fluid system can be described by the Stokes equation:

$$0 = -\nabla p + \eta \nabla^2 \mathbf{v} + \rho \mathbf{g} \tag{17}$$

In all cases, the mass continuity equation needs to be satisfied, which describes the conservation of mass for hydrodynamics:[6]

$$\frac{\partial \rho}{\partial t} + \nabla \cdot (\rho \mathbf{v}) = 0 \tag{18}$$

For incompressible fluids like water, the density along the streamline remains constant over time:

$$\frac{\partial \rho}{\partial t} = 0 \tag{19}$$

Therefore, the mass of the fluid, which flows in and out of a defined volume must be the same over a certain time, simplifying eq. (18) to:[3]

$$\nabla \cdot \mathbf{v} = 0 \tag{20}$$

2.1.2 Dimensionless numbers

The importance of physical phenomena, that occur in microfluidic devices, must be judged between competing phenomena.[4] Therefore, dimensionless numbers are defined, which express the ratio of these phenomena and give a sense for the classification of a system in the fluidic parameter space.[4]

Important representatives for these dimensionless numbers are the Reynolds number (Re), relating inertia forces to viscous forces, the Péclet number (Pe), relating convection to diffusion, the Weissenberg number (Wi) and the Deborah number (De), both describing the time-wise response of viscoelastic fluids to deformation.

Reynolds number

The Reynolds number is the most characteristic dimensionless number for microfluidics, since microfluidic devices normally operate at low Reynolds numbers. Flows at low Reynolds numbers contradict the day-to-day human experience with moving fluids.[4]

Just like any solid object, a moving fluid has momentum and inertial forces counteract any change in motion. When a fluid moves inside a channel, not every fluid element is moving at the same speed. The outer layers are slowed down by the channel walls, while the fluid in the middle of the channel can flow freely, which creates shear between the fluid layers. The viscosity of a fluid is a measure of its resistance to this deformation. When inertial forces of the fluid overcome the viscous forces, the fluid layers no longer flow in an orderly manner next to each other and the flow becomes turbulent.

The Reynolds number is defined as the ratio of inertial forces to viscous forces

$$Re = \frac{\text{inertial forces}}{\text{viscous forces}} = \frac{\rho \cdot v \cdot l}{\eta} \tag{21}$$

where ρ is the density of the fluid, v is the flow velocity, η is the dynamic viscosity, and l is the characteristic length.[5,7]

Different flow regimes can be distinguished by the Reynolds number. Laminar flow occurs at low Reynolds numbers, where viscous forces are dominant, and the flow is characterized by a smooth and constant fluid motion. The Reynolds number can be estimated for microfluidic devices and water as typically used solvent. With channel dimensions in the range of 10-100 µm and typical velocities between 1 µm/s and 1 cm/s, the Reynolds number ranges between 10^{-5} and 1. Accordingly, the flow in microfluidic devices is laminar in almost all cases. When the Reynolds number increases, the laminar flow transitions into an unpredictable and irregular turbulent flow. This flow transition happens in stages and the critical Reynolds numbers are different for every geometry.

In summary, the Reynolds number is used to predict the transition from laminar to turbulent flow. Moreover, similar flow situations of different scale can be compared.

Péclet number

The Péclet number is especially important at low Reynolds numbers, where mixing is only based on diffusion. Turbulent mixing is very fast due to random eddies that continuously fold fluid elements, thereby reducing the diffusion distance.[4] In contrast, mixing in laminar flows can take a very long time, depending on the distance the molecules have to travel by diffusion.

Considering a T-junction, where two different solutions are brought together and flow next to each other, the Péclet number is a measure for the distance, compared to the channel width, that both fluids travel along the channel, until they are mixed homogeneously by diffusion.

The Péclet number, which expresses the relative importance of convection to diffusion, is defined as

$$Pe = \frac{\text{convection}}{\text{diffusion}} = \frac{v \cdot l}{D} \tag{22}$$

where v is the flow velocity, l is the characteristic length, and D is the mass diffusion coefficient.[4]

Deborah number

The Deborah number distinguishes how a particular material will behave over a given timeframe, when experiencing a deformation.[8] For example, in microfluidics, when the channel diameter is reduced over a certain length, the flow accelerates and experiences elongational stress over the time it takes to pass through this channel segment.

The Deborah number De compares the relaxation time τ_p to the time scale of the process τ_{flow}:[8,9]

$$De = \frac{\tau_p}{\tau_{flow}} \tag{23}$$

If the timeframe is long compared to the relaxation time of the material, then a viscous, fluid-like behavior is observed. Conversely, if the time scale of the process is much shorter than the relaxation time, the material cannot respond to the stimulus in time and behaves as a solid.[8]

However, the Deborah number alone is insufficient to fully characterize effects due to viscoelasticity. In steady flows, the Deborah number becomes zero regardless of the relaxation time.[8]

Weissenberg number

In flows with a constant deformation history, the Weissenberg number indicates the degree of anisotropy or orientation generated by the deformation. For example, when a polymer solution flows through a tapering of a microfluidic channel and experiences extensional stress, the polymer molecules become stretched and aligned in flow direction.

The Weissenberg number Wi relates the polymer relaxation time τ_p to the flow deformation time, which correlates with either the inverse extensional rate $\dot{\varepsilon}$ or inverse shear rate $\dot{\gamma}$.[4,8]

$$Wi = \frac{\text{elastic forces}}{\text{viscous forces}} = \tau_p \cdot \dot{\varepsilon} \quad \text{or} \quad Wi = \tau_p \cdot \dot{\gamma} \tag{24}$$

For small Wi, the polymer relaxes, before the flow deforms it significantly.[4] Conversely, for large Wi, the polymer chains are deformed significantly, as their relaxation rate is slower than the deformation rate.

2.2 Fundamentals of microfluidic fiber spinning

2.2.1 Hydrodynamic flow focusing

There are two major subcategories of chip-based microfluidics, which are droplet-based microfluidics and continuous-flow microfluidics. As droplet-based microfluidics manipulates discrete volumes of immiscible fluids, it represents a batch process. Since fibers are anisotropic objects where one dimension is significantly larger than the other, they are produced in a continuous process. One basic principle of continuous-flow microfluidics is hydrodynamic flow focusing. One kind of fluid flows through the main channel of a microfluidic device and a second fluid enters at a cross junction from the sides. The inner fluid is focused into a smaller stream by the outer fluid, which flows side by side. A time-independent steady state is developed by the liquid flow. At low Reynolds numbers, the mass transfer perpendicular to the flow direction only takes place by diffusion, so an interdiffusion layer is formed at the interface between the fluid of the main channel and the fluid of the side channels. When the focused fluid contains a dissolved species, a concentration gradient can be observed, that gets wider as the fluids flow along the channel. A finite element method (FEM) simulation of the concentration of a dissolved species for hydrodynamic flow focusing can be seen in Fig. 2B. If there is a chemical reaction happening, each x-position in the main channel shows a distinct time-wise progression of the reaction. Fresh material always needs the same time to reach the corresponding channel position.
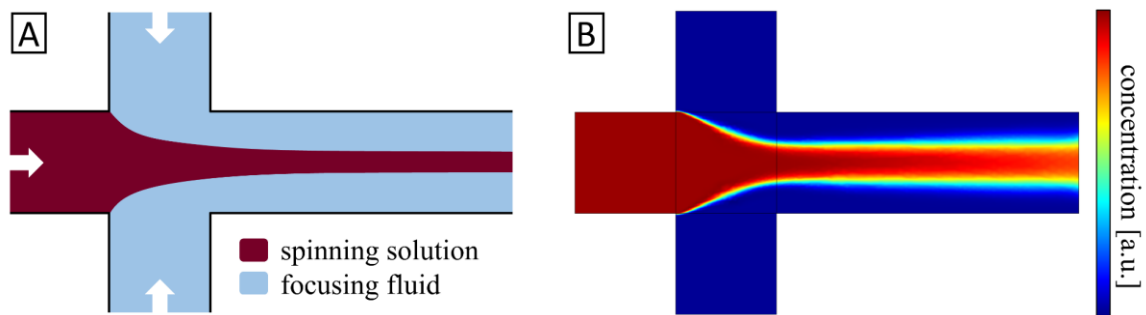

Figure 2: (A) Hydrodynamic flow focusing is shown exemplarily for wet spinning of fibers, where the spinning solution is focused by a focusing fluid, that enters from the side channels. (B) The concentration of a dissolved species can be simulated for every point in the channel by FEM simulations.

When taking microfluidic wet spinning as example, the fluid in the main channel, that gets focused, is the spinning solution. In the two-dimensional layout of the channels, shown in Fig. 2, the spinning solution is just confined from the sides but is still in contact to the bottom and the top of the channel. This can lead to deposits on the channel walls, which over time could clog the channel. To avoid this, three-dimensional channel geometries can be used, in which the spinning solution is not only focused from the sides, but also from above and below. Fig. 3 shows three-dimensional CAD models of a symmetrical and an asymmetrical channel layout. Both geometries generate a sheath flow of the focusing fluid

around the inner spinning solution and thus prevent contact with all four walls of the main channel. Additionally, the asymmetric version induces a spinning motion of the focused fluid, which can possibly lead to a twisted fiber.
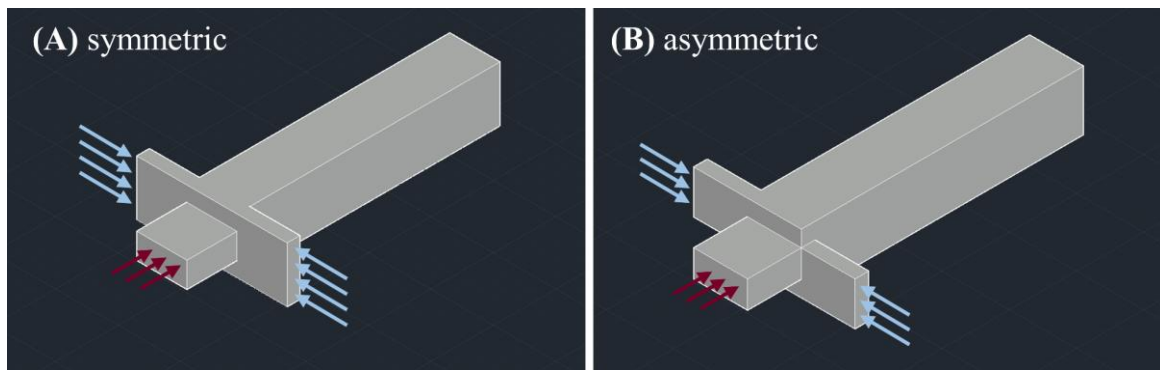

Figure 3: The CAD models show two different versions of the cross junction for a channel layout with 3D-focusing of the inner fluid: (A) symmetric and (B) asymmetric.

However, wall adhesion can occur even for the 3D channel geometries as there is a stagnation line at the edge where both fluids come in contact with each other for the first time. Due to the no-slip boundary condition at the fixed channel walls, a parabolic flow profile is assumed at low Reynolds numbers, which is called Poiseuille flow.[5,10] This means that the flow velocity is zero at the stagnation line and precipitations cannot be flushed away, instead they stick to the wall and grow in size.[10] Fig. 4 shows the position of the stagnation line; however, the stagnation line is a stagnation point in this 2D projection.
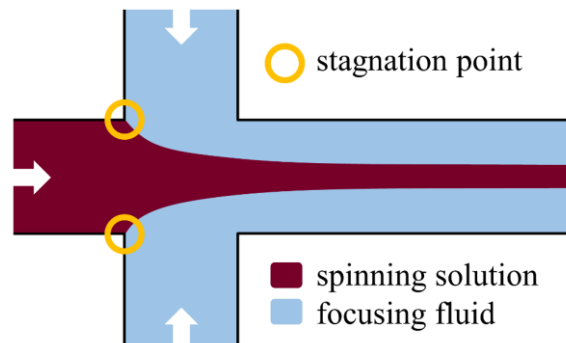

Figure 4: The flow velocity is zero at the solid boundary, because the no-slip condition is assumed for parabolic Poiseuille flow. As a consequence, there is a stagnation point at the edge, where both fluids converge. Precipitations remain there, since they are not carried away by the flow.

The presence of a stagnation line can be prevented by focusing the spinning solution with a separating fluid first and focusing the stream with the actual focusing fluid in a subsequent step. The inert separating fluid creates a sheath flow around the spinning solution in the center of the channel. Only then, the reactive components from the spinning solution and the focusing fluid come into contact by diffusion. At this moment, the fluid interface is in the center of the channel and so is the forming fiber. The thickness of the sheath flow can be adjusted by the volumetric flow rates of the respective fluids.

This double focusing can be achieved by two separate cross junctions, which are arranged one after the other, or by an intersection of five inlet channels, which results in a more compact variant. Both alternatives are illustrated in Fig. 5. As with the single focusing design, a three-dimensional architecture with different channel heights is used for the double focusing design to prevent contact to the top and bottom.
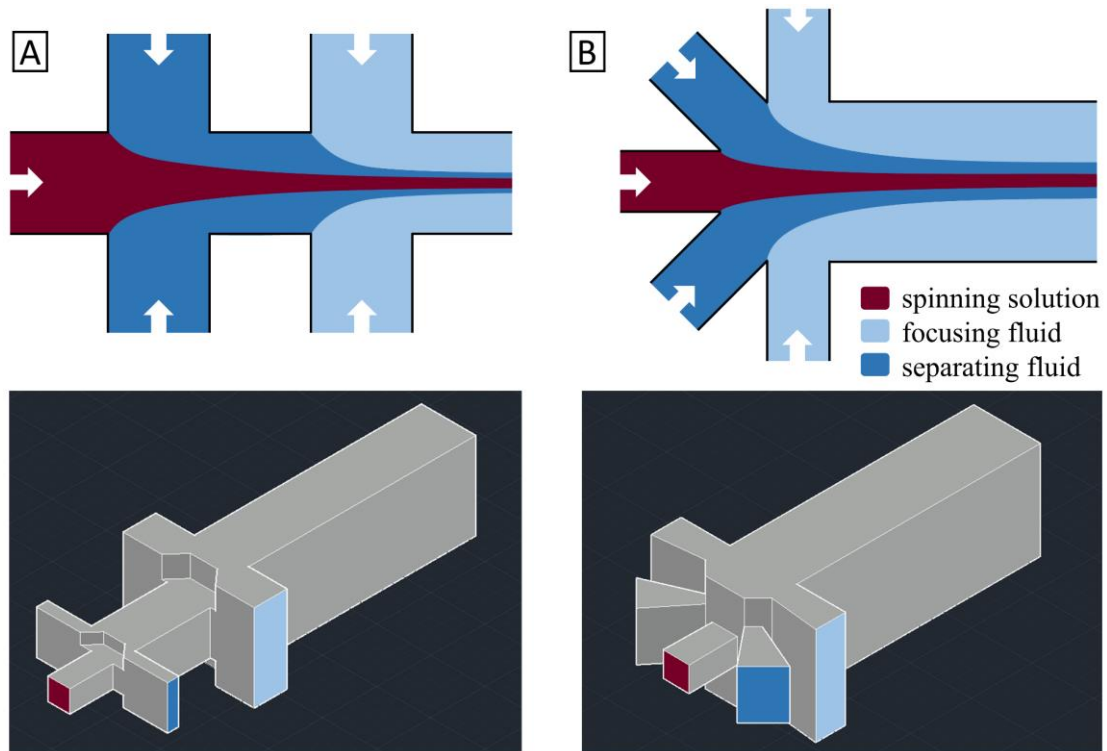

Figure 5: Two variants of a double focusing channel design are shown as 3D-CAD model (bottom), and as 2D projection (top), illustrating the flow of the different fluids. The channel layout can feature two consecutive cross junctions (A), or a more compact design with five joined inlets (B).

2.2.2   Significance of chain entanglements

Dry spinning shows quite a few similarities to electrospinning, as for both spinning methods a small liquid jet is generated, which solidifies by evaporation in the middle of air. The entanglement number of the polymer chains is an important parameter that significantly influence fiber formation. A jet of a polymer solution below the entanglement concentration or of low molecular weight breaks up into droplets and generates a spray, so that no continuous fiber can be produced.

The critical entanglement concentration is the minimum concentration that is required to get continuous fibers.[11] The polymer concentration must be at least 2-2.5 times the entanglement concentration to spin uniform and bead-free fibers, otherwise only beaded fibers are obtained.[11,12] Therefore, the entanglement concentration separates the unentangled regime from the entangled regime, where polymer chains significantly overlap one another such that individual chain motion is constrained.[12]

For a given molecular weight M, the entanglement density increases with the polymer concentration c, or rather with the volume fraction of polymer ϕ_p, and vice versa.[13] As a result, the solution viscosity η increases accordingly. These statements are valid for good solvents, or when specific polymer-polymer interactions, such as hydrogen bonds, can be neglected, otherwise additional effects have to be taken into account.[13] These relationships are explained in more detail below.

In polymer melts, the number of entanglements increases with the length of the polymer chains, respectively the molecular weight M. At low molecular weights, when there are no chain entanglements, the zero-shear melt viscosity η_0 is direct proportional to M. Above a critical molecular weight M_c, corresponding to one entanglement per chain, the dependence of η_0 changes from M^1 to $M^{3.4}$.[14] The critical molecular weight M_c marks the onset of entanglement behavior, while the entanglement molecular weight M_e corresponds to the average molecular weight between entanglement junctions. The ratio of M_c/M_e is about ~ 2 for most polymers to form at least one entanglement per chain.

In polymer solutions, the number of chain entanglements is additionally affected by the concentration, respectively the volume fraction of the polymer ϕ_p. Below the critical concentration c^*, the solution is diluted to such an extent that the polymer chains are separated and do not entangle. Above the critical concentration c^*, chain overlap is initiated, and the number of chain entanglements is proportional to the concentration c.

The polymer volume fraction ϕ_p relates the entanglement molecular weight in solution $(M_e)_s$ to the respective one in melt M_e:[13]

$$(M_e)_s = \frac{M_e}{\phi_p} \tag{25}$$

Just as in polymer melts, the solution viscosity increases faster above a critical molecular weight $(M_c)_s$, where $(M_c)_s/(M_e)_s \sim 2$.[13]

The entanglement number in solutions $(n_e)_s$ is defined as the ratio of the molecular weight M to its solution entanglement molecular weight $(M_e)_s$:

$$(n_e)_s = \frac{M}{(M_e)_s} \tag{26}$$

For polydisperse systems, the weight-average of the molecular weight M_w is typically used as the molecular weight. As a result, the entanglement number for concentrated solutions $(c \gtrsim c^*)$ can be determined by eq. (27):[13]

$$(n_e)_s = \frac{M_w}{(M_e)_s} = \frac{\phi_p \cdot M_w}{M_e} \tag{27}$$

However, the number of entanglements per chain is given by $(n_e)_s - 1$, since an entanglement necessarily involves two chains.[13]

2.3 Fabrication of microfluidic devices

Many microfluidic applications are based on the manipulation of continuous liquid flows through microfabricated channels. There are a lot of different requirements for microfluidic devices featuring these channels for fluid handling. First of all, there has to exist an applicable method to pattern the material for the microfluidic chip. This includes designing the desired channel structures and transferring them accurately to the chip material. As the devices are usually consisting of two or more individual parts, which have to be connected in a precise manner, the material has to offer the possibility to align the parts accurately and to bond them leak-tight. One of the most important aspects is the optical transparency of the device, so it is possible to monitor the experiment and adjust the parameters as necessary. Not only the transparency to visible light is important, but also the transparency to UV light or X-rays, when in-situ measurements should be performed like e.g. kinetic studies on particle growth and self-assembly.[15,16] The material should offer mechanical stability, to avoid deformation or expansion of the channels under high pressure. Another requirement is the compatibility of the material to the used solvents and the chemical stability.[17,18] Thermal stability is important for reactions under raised temperature.

First fluidic microsystems were made from glass or silicon since the applied techniques originate from the production of microelectronics and microelectromechanical systems (MEMS).[19] However, for many applications the use of devices fabricated in glass and silicon was unnecessary or inappropriate as it was too expensive and complex.[19] The exploratory research required that new concepts could be tested in a timely manner and iteration cycles were reasonably short. Therefore, one polymer established itself as key material for exploratory research in microfluidics – poly(dimethylsiloxane) (PDMS).[19]

The elastomer PDMS is transparent in the UV-visible regions and offers several characteristics which are beneficial for fabricating microfluidic devices.[20] PDMS enables rapid prototyping by using lithographic techniques, which are described in detail in chapter 2.3.1.[21–24] Two parts of PDMS can be bonded and sealed permanently by plasma activation of the surface.[25] Functional elements like pumps, mixers and valves can be implemented directly in the design and supplemented by additional probes and electrodes.[19,20,26] The modification of the PDMS surface is possible, which allows to change the hydrophobicity of channel walls. Connecting the tubing for feeding the fluids is a simple task, since the tubing can be plugged in pre-punched holes and the elastic material seals itself around the tubing. PDMS-based microfluidic devices are compatible to most polar solvents like water, most alcohols, disubstituted amides (NMP, DMF) and sulfoxides (DMSO).[27] However, PDMS swells in nonpolar solvents like pentane and xylenes.[27] This leads to a reduction of the cross-sectional area and up to a complete obstruction of the channels. The loss of solute is a concern, if the solubility of the solute in PDMS is

significant.[27] Additionally, there are still oligomers in the cross-linked PDMS, which could dissolve in the used solvents and contaminate the products.[27]

Besides the fabrication from metal, glass or silicon by etching, microfluidic devices can be produced from engineering thermoplastics like polycarbonate (PC), polystyrene (PS), poly(methyl methacrylate) (PMMA) or cyclic olefin copolymer (COC) by hot embossing, micro-machining or injection molding. Even additive manufacturing, also known as 3D-printing, can be used for producing microfluidic chips as shown in chapter 2.3.2.

2.3.1   Fabrication using lithography techniques

Poly(dimethylsiloxane) (PDMS) is a widely used material for microfluidic applications. This fact is not only based on its advantageous chemical and physical properties, but also on the short period of time between the conceptual design for a device and its realization. This rapid prototyping process consists of three phases: photolithography, soft lithography and chip assembly. The complete process is shown in detail in Fig. 6.

At first, the desired channel structures are designed with the help of computer-aided design (CAD) software and transferred to a casting master by photolithography. These steps are conducted in a dust-free environment in a cleanroom. A polished silicon wafer is spin-coated with a uniform layer of photoresist. A commonly used photo resist is SU-8, which is an epoxy-based and acid-catalyzed negative photoresist.[28] A negative photoresist crosslinks upon exposure, while unexposed areas remain soluble and can be washed away during development. The main component of the photoresist is EPON SU-8, a registered trademark of Shell Chemical Company, which is a multifunctional molecule with eight reactive epoxy groups (Fig. 7A). The solvent could be propylene glycol methyl ether acetate (PGMEA), cyclopentanone, or γ-butyrolactone (GBL).[28] Depending on the desired layer thickness, different formulations of SU-8 exist, which differ in the solid content of EPON SU-8 and consequently in the viscosity. The viscosity defines the possible range of layer thickness in the spin-coating process.
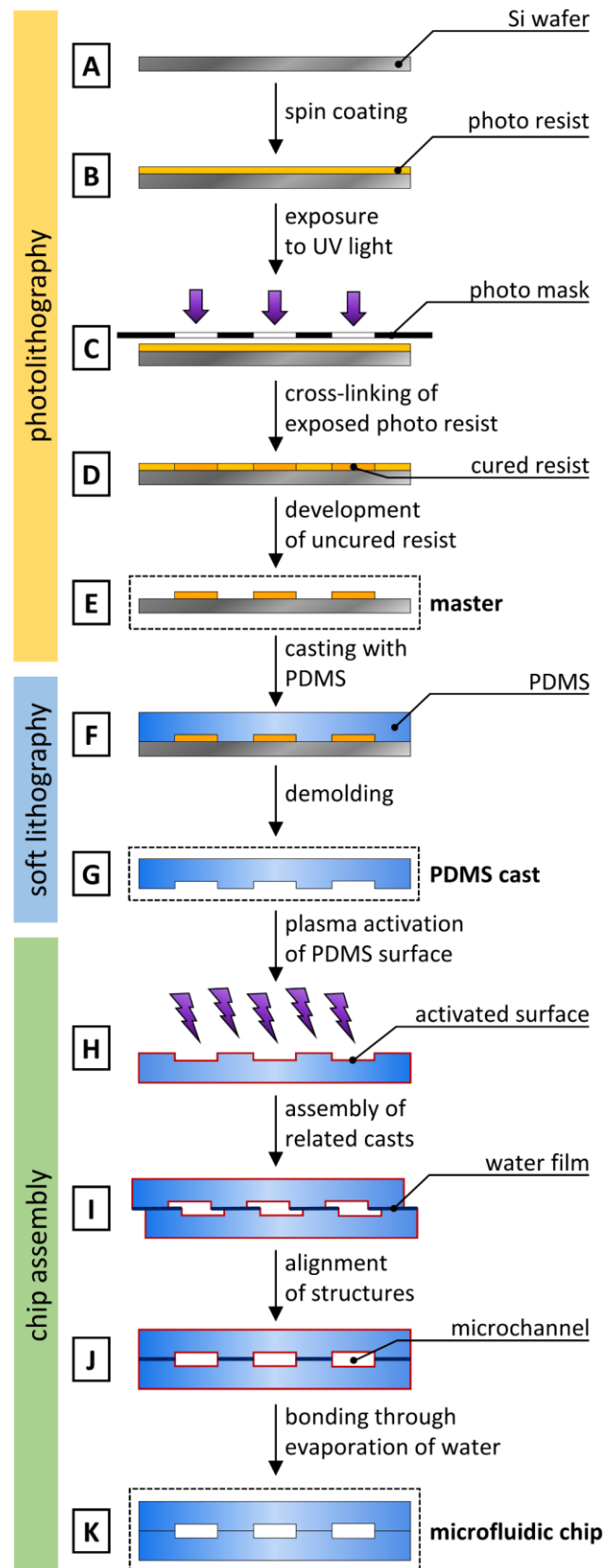
Figure 6: The fabrication process of microfluidic PDMS devices consists of three phases: photolithography, soft lithography and the final chip assembly. The channel structures, which were created by means of CAD software, are transferred from a photo mask to a thin spin-coated film of photo resist on a silicon wafer by exposure with UV light. The cross-linked photo resist serves as casting master for PDMS prepolymer, which contains the microstructures after curing. After cutting and punching holes for connection of tubing, the PDMS cast is surface-activated by plasma treatment and two matching parts are bonded to a ready-made chip.
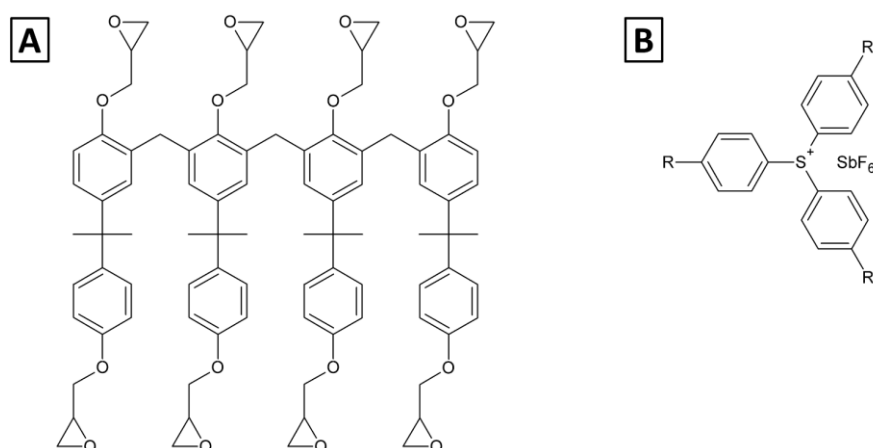
Figure 7: A) Structural formula of the multifunctional EPON SU-8 resin. Each molecule contains eight epoxy groups, which are cross-linked by cationic ring-opening polymerization. B) Structural formula of triarylsulfonium hexafluoroantimonate salt, which is added as photoinitiator to the SU-8 resist.

The second component is a triarylsulfonium hexafluoroantimonate salt, which acts as a photoacid generator (Fig. 7B). When exposed to UV-light, the photoinitiator decomposes to hexafluoroantimonic acid, which initiates the cationic ring-opening polymerization (CROP) of EPON SU-8 by protonating the epoxy groups.[28–30] These protonated oxonium ions are able to react with other neutral epoxides and thus, propagate the cross-linking reaction of the highly branched molecules after application of heat (see Fig. 8).[28]
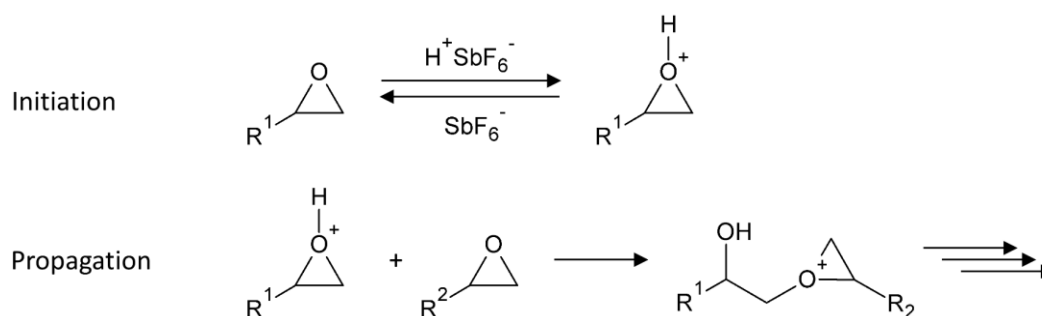

Figure 8: The photoresist SU-8 is cross-linked by cationic ring-opening polymerization (CROP). The epoxy groups are protonated by hexafluoroantimonic acid which acts as catalyst. The protonated oxonium ions react with further neutral epoxy groups in a series of cross-linking reactions after application of heat.

The channel layout is printed in very high resolution either as emulsion film on a flexible transparency or as chrome oxide film on quartz or soda lime glass (Fig. 11A). Lateral feature sizes as small as 1 µm can be reached.[31] Using a mask aligner, the photoresist is irradiated through this photo mask with light of the near-UV range (i-line, 365 nm) of a broadband mercury lamp. The cross-linking of the resist takes place in the post-exposure bake at elevated temperatures. The steps A-D in Fig. 6 can be repeated in order to get multiple layers of photoresist. This enables more complex channel designs with a pyramidal architecture. Afterwards, the uncured photoresist can be washed away by using the developer 1-methoxy-2-propanol acetate and a silicon master is obtained, which features the channels as inverted structures (Fig. 11B).
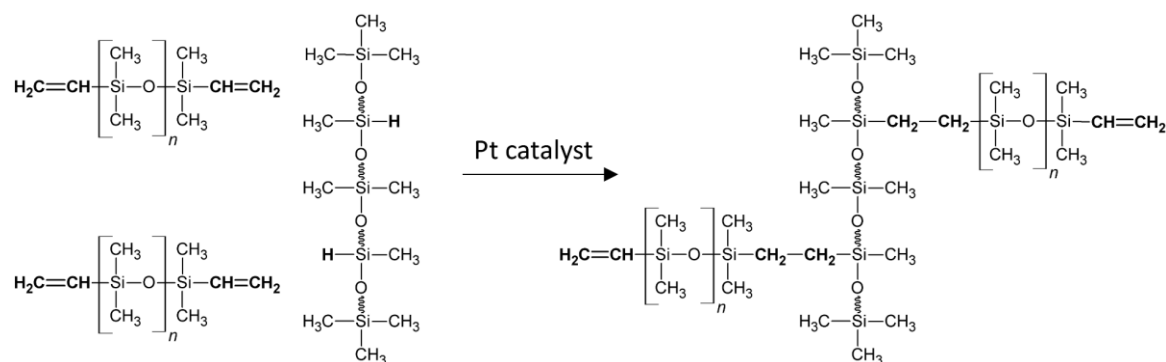
Figure 9: Reaction scheme for cross-linking of PDMS by hydrosilation. A vinyl-terminated base polymer and a curing agent, which consists of a copolymer having hydrosilane groups and a platinum complex as catalyst, are mixed in a ratio of 10:1. The liquid silicone mixture react at elevated temperature to a solid cross-linked elastomer.

In the next step, the structures are transferred from the master to the chip material PDMS by soft lithography. A base polymer and a curing agent are mixed in the ration of 10:1 and poured on the master, where the liquid mixture is cured at elevated temperatures and forms a solid cross-linked elastomer. The base polymer is a vinyl-terminated poly(dimethylsiloxane). The curing agent contains a mixture of a platinum complex as catalyst and a copolymer of methylhydrosiloxane and dimethylsiloxane. The vinyl groups ($SiCH=CH_2$) and the hydrosilane groups (SiH) crosslink in a catalytic hydrosilation reaction (Fig. 9).[32] PDMS allows to cast the structures of the master with sub-0.1-µm fidelity, since it has a low interfacial free energy of 21.6 mN/m.[21,33]

The PDMS replica can be released easily without damaging complex and fragile structures due to its elastic characteristic.[21] As the structures are inverted by replica molding, the PDMS cast contains the channels as lowered structures.

In the last phase, the microfluidic device needs to be assembled from two matching PDMS parts. Excess material is cut off from the casted PDMS and holes are punched to connect the tubing later. Three-dimensional channel geometries can be achieved, if both connected PDMS parts are structured. However, a precise alignment is necessary, because even a small offset can disturb the fluid flow in the microchannels.
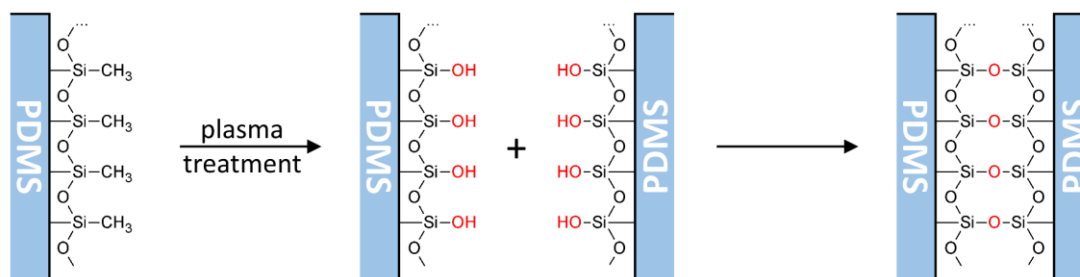
Figure 10: When assembling the microfluidic devices, two PDMS parts need to be bonded permanently and leak-tight. This can be achieved by a treatment with air plasma, which actives the PDMS surface by oxidation through oxygen radicals. The created silanol groups react with each other when brought in close contact and form permanent covalent bonds.

The surface of the PDMS replicas can be activated by a treatment with air plasma. Oxygen radicals are able to oxidize the methyl groups ($SiCH_3$) to silanol groups (SiOH), which can react with each other. When the PDMS surfaces are brought in conformal contact, covalent Si-O-Si bonds are formed (Fig. 10). These bonds are so strong, that cohesion failure of the PDMS occurs, when trying to separate the parts again. Since the activated PDMS adheres instantly when brought in contact, a thin film of water as lubricant is necessary. Both parts can be aligned precisely and remain adjustable until the water is removed by evaporation at elevated temperatures. Whereas the surface of the oxidized PDMS would reconstruct in air in a few minutes, it retains its hydrophilic properties while in contact with water or polar organic solvents.[33–35]

Finally, the microfluidic device is completely manufactured (Fig. 11C) and can be connected via tubing to syringe pumps or pressurized gas.
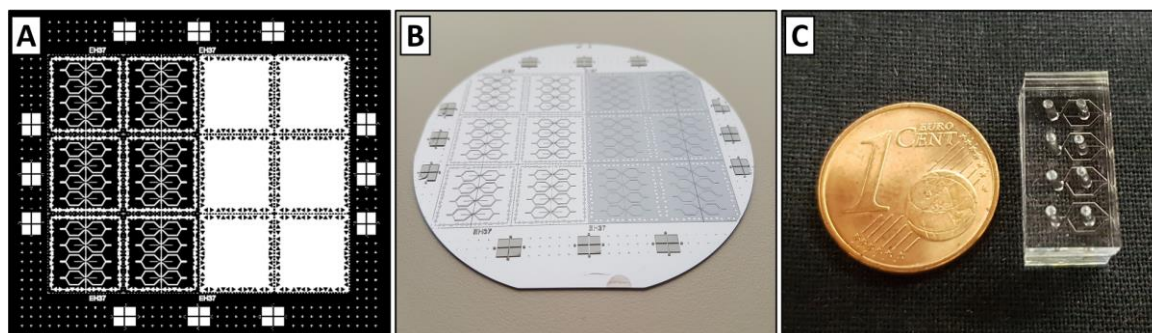

Figure 11: Layout of microstructures printed on high-resolution photo mask (A), master for casting of PDMS (B), ready-made microfluidic device (C).

2.3.2 Recent trend: Fabrication using 3D printing

Additive manufacturing, which is also known as 3D printing, creates an object by adding successive layers of material.[36] 3D printing has been on the rise due to technological advancements in terms of resolution and speed during the last decade.[37] It is hardly surprising, that researchers are interested in this promising technology. The possibilities for

microfluidic applications and also the limitations are explored right now, which manifests in an increasing number of publications in the last five years.[37–43]

The process of additive manufacturing consists of the two main steps of designing the microfluidic device and its fabrication via 3D printer.[37] First of all, the microfluidic device is constructed in a computer-aided design (CAD) software. Afterwards, the designed object is converted into a standard triangulation language (STL) file. This STL file is digitally sliced into individual layers and translated into computer numerical control (CNC) code, which can be processed by the 3D printer.[42] The 3D printer sequentially builds the object layer by layer. This basic procedure is the same for all kinds of 3D printers, which utilize different functional principles and handle various materials.

3D printed molds can be used for rapid fabrication of complex and arbitrary microchannel geometries in PDMS, which are unattainable by the photolithography based method presented in chapter 2.3.1.[40] However, the focus is on the fabrication of microfluidic devices in an one-step process, in which the final devices are made directly from the digital data.[37] Further physical or chemical treatment may be necessary for surface modification or cleaning up of the device.[37]

The main advantage of the one-step process is, that it is fast adaptable and easily applicable. There is no need for an intermediate process step like photolithography, which is time consuming and involves manual operations that are critical for the accuracy of the microfluidic device.[44] Especially in biological and medical research, it is beneficial if researchers can focus on the experiments instead of learning a complicated fabrication process. Since microfluidic devices can be printed directly from CAD data, channel designs can easily be shared and exchanged between labs, which have access to a 3D printer. Researchers can adopt a "try and error" strategy, as simple microfluidic devices can be printed in several minutes to an hour and because only appropriate CAD software and 3D printer are necessary.[42]

Despite these benefits, 3D printing has still serious limitations in terms of minimum feature size, surface roughness, optical transparency or choice of material.[42] The removal of excess or support material in small microchannels is challenging, as the removal process is diffusion-limited.[39]

The most widely used 3D printing techniques, which are suitable for microfluidic applications, are stereolithography (SLA), inkjet 3D printing (i3DP), two-photon polymerization (2PP) and fused deposition modeling (FDM).[42]

Stereolithography is based on the spatially controlled photopolymerization of a UV-curable liquid resin, performed by a scanning laser or a digital light projector (DLP) in a layer-by-layer manner.[42]

Inkjet 3D printing advances the existing technology of inkjet printers by using solutions of UV-curable polymers as ink. Small droplets get ejected on demand by the print head. These droplets get cross-linked on the substrate by UV light and builds up three-dimensional objects.[42]

Two-photon polymerization has the highest resolution of the presented 3D printing techniques. Arbitrary three-dimensional structures can be built from voxels with sub-micrometer dimensions.[45] A photocurable epoxy resin is cross-linked, when two photons of a near-infrared femtosecond laser are absorbed simultaneously by a single molecule.[42] However, this high spacial resolution and small feature sizes are accompanied by a slow build time for macroscopic objects.[37]

In 1992, the US patent described as "apparatus and method for creating three-dimensional objects" was awarded to Scott S. Crump.[46] Since the expiration of the patent, this 3D printing technique, called fused deposition modeling (FDM), got accessible to the general public. Heated thermoplastic material is extruded from a positionable nozzle and laid down layer by layer.[37] A wide variety of inexpensive and biocompatible thermoplastics can be used like for example acrylonitrile butadiene styrene (ABS), poly(lactic acid) (PLA), poly(ethylene terephthalate) (PET), polypropylene (PP), polycarbonate (PC), polyamide (PA), polyether ether ketone (PEEK), and poly(phenylene sulfide) (PPS).[36,37,39,41,42]

An example for a microfluidic device, which was made using an FDM 3D printer, is shown in Fig. 12. This disk-shaped microfluidic device contains a simple mixing cross as channel layout and was printed on an *Ultimaker 2* 3D printer (Ultimaker B.V.) in a transparent compound material named *BendLAY*. It is possible to fabricate very thin, transparent and leak-tight devices having channels of 500 µm or less in diameter. However, the walls of the channels are not smooth and clearly show the horizontally layered build-up of the device.
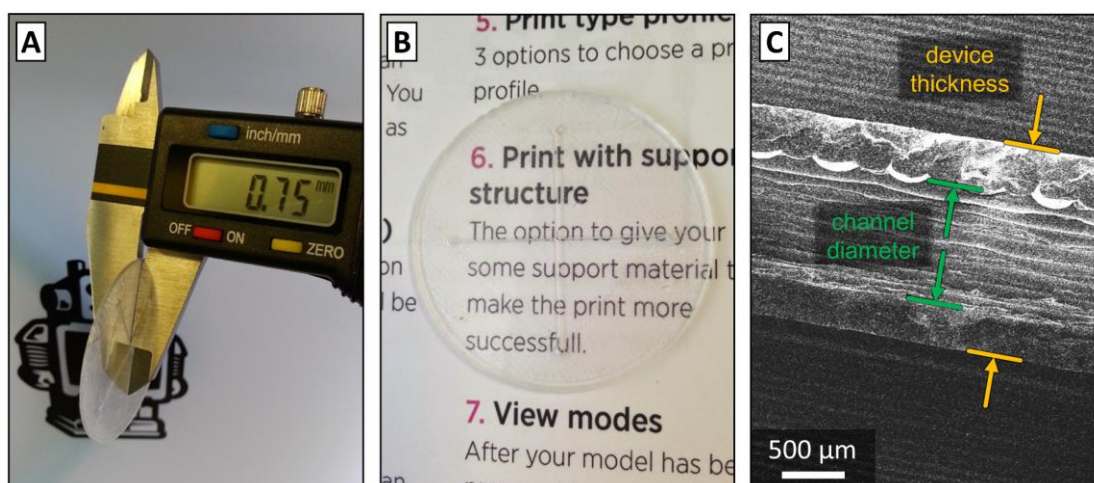

Figure 12: Fused deposition modeling (FDM) was used to print a fully functional and leak-tight microfluidic device of 0.75 mm in thickness (A). A high transparency of the device is necessary for the observation of experiments (B). An SEM image of the cross-section of an 3D printed microfluidic chip shows that the channel walls are structured as the printing process is performed layer by layer (C).

In Fig. 13 is illustrated how microfluidic devices could be used to spin alginate fibers in a wet-spinning process. A 3D-printed frame with integrated tube fittings locks the microfluidic chip into position (Fig. 13A/B). Inside the channel, an alginate solution is focused by calcium lactate, which forces the formation of an alginate fiber (Fig. 13D). The fiber exits the device by an open channel and can be collected on a spool (Fig. 13C).

In conclusion, 3D printing could help to spread microfluidic applications, because it is cost efficient and enables rapid prototyping. The fabrication of microfluidic devices via 3D printers requires less skill of the operator than conventional techniques. Devices could pursue a modular design and could be shared between users by the internet.[41]
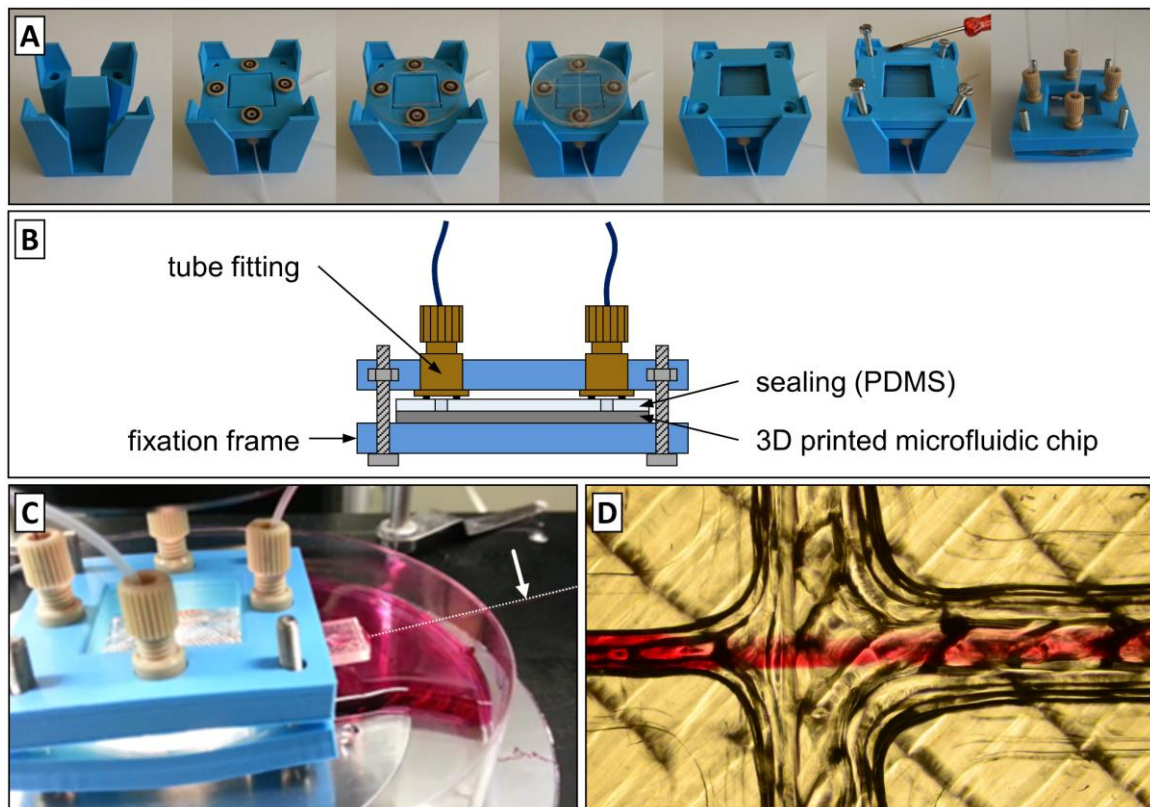

Figure 13: A series of pictures shows the assembly of a fixation frame for a 3D printed microfluidic device (A). The frame contains a sealing made of PDMS and integrated tube fittings, which establish a tight connection between the device and the tubings feeding the fluids (B). This setup was used for wet-spinning of a continuous alginate fibers (indicated by an arrow and a dotted line) (C). This microscopic image shows the flow focusing of the red-dyed alginate solution at the cross junction of the channels (D).

2.4 Small-angle x-ray scattering (SAXS)

2.4.1 Introduction to SAXS

Small-angle X-ray scattering (SAXS) is a powerful technique to characterize colloidal systems regarding averaged particle size, shape and orientation.[47] The samples may be solid or liquid matrices, which contain solid, liquid or gaseous domains of the same or another material in any combination.[47] The contrast in SAXS arises from the differences of electron density of the particles compared to the surrounding matrix.

The particle or structure size, that can be resolved, ranges from 1 to 100 nm in a typical SAXS setup and can be extended on both sides by measuring at even smaller angles (ultra-small-angle X-ray scattering, USAXS) or larger angles (wide-angle X-ray scattering, WAXS, also known as X-ray diffraction, XRD) than the typical 0.1° to 10°.[47]

In transmission mode, the X-rays are sent through the sample and every particle inside the beam can possibly interact with the X-rays, so the measured signal is an average value of all illuminated particles and gives information about the bulk material. In contrast, surface-near particles or thin layers can be selectively measured by GISAXS (grazing-incidence small-angle X-ray scattering), where the X-ray beam hits the surface almost parallel at a very small angle and is reflected.

2.4.2 Interaction of X-rays with matter

When X-rays hit a sample, there are several options: A fraction of the radiation passes through the sample without interacting, a fraction is absorbed and transformed into other forms of energy like fluorescence radiation and heat, and a fraction is scattered in different directions.[47]

The scattering of X-rays can be distinguished in elastic (Thomson scattering) and inelastic scattering (Compton scattering). Compton scattering occurs when a photon hits an electron, which is bounced away. A part of the energy of the photon is transferred to the electron.[48] Thomson scattering happens when photons collide with strongly bound electrons without transferring energy.[47] The electrons start to oscillate at the same frequency as the incoming wave and emit spherical waves themselves.[47]

While Compton scattering is incoherent and has no particular phase relationship with the incident radiation, Thomson scattering is coherent and carries structural information of the sample.[47] Coherent waves can interfere with each other, because all waves have the same wavelength and amplitude, and only differ in their phase relationship. Whether these waves show constructive (in phase) or destructive interference (out of phase) can be judged by Bragg's law (eq. (28)), which describes the angle of incidence θ at which a constructive interference exists between two planes of the distance d, on which the scattering centers are arranged:[49]

$$n \cdot \lambda = 2d \cdot \sin \theta \tag{28}$$

where λ is the wavelength of the incident wave and n is a positive integer.

Bragg's law can easily be deduced from geometrical considerations, when looking at Fig. 14A. The path for the wave, scattered at the lower plane, is longer than the path for the upper plane. The path difference 2δ, which is highlighted in red, can be calculated trigonometrically:

$$\delta = d \cdot \sin \theta \tag{29}$$

Since constructive interference occurs when the path difference is a multiple n of the wavelength λ, eq. (28) can be derived.
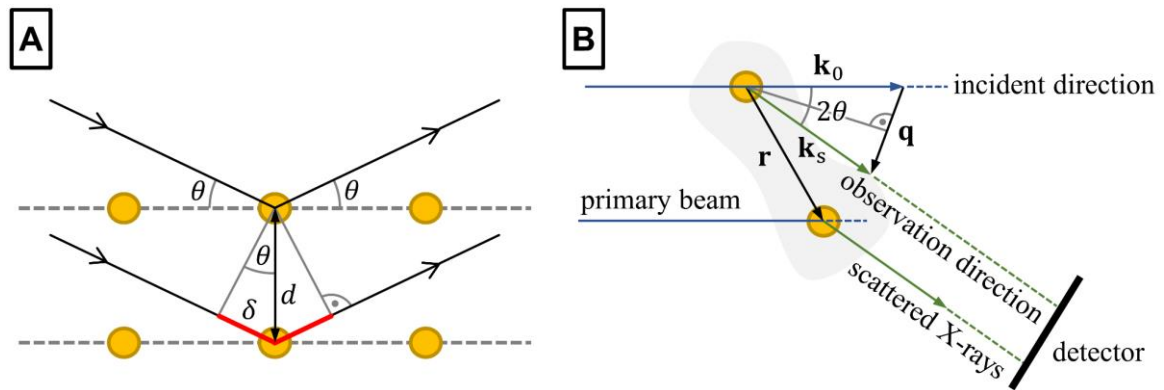

Figure 14: (A) When two waves of identical wavelength and phase are scattered of two atoms within a crystalline structure, one wave travels an extra distance 2δ. If the path difference is a multiple of the wavelength, constructive interference occurs. (B) Spherical waves are emitted from two atoms in a colloidal particle and produce a 2D interference pattern on the detector plane.

Fig 14B shows two atoms, which emit spherical waves, when X-rays are scattered at these atoms. As the outgoing waves from the Thomson scattering are coherent, they produce 2D interference patterns at the position of the detector. Whether this interference is constructive, destructive or somewhere in between depends on the angle 2θ of observation and the distance $\mathbf{r}$ between the light-emitting atoms.[47]

The detector only measures the intensity $I(\mathbf{q})$ of the wave, which is proportional to the squared amplitude $E(\mathbf{q})$ of the wave.

$$I(\mathbf{q}) \propto |E(\mathbf{q})|^2 \tag{30}$$

Thus, valuable information about the sign or the phase of the electric field is lost, and a structural analysis is only possible with additional knowledge about the sample.

A wave vector $\mathbf{k}_0$ in incident direction and a wave vector $\mathbf{k}_s$ of the scattered X-rays in direction of observation are defined, which have the same absolute value due to elastic scattering.

$$k = |\mathbf{k}_0| = |\mathbf{k}_\mathrm{s}| = \frac{2\pi}{\lambda} \tag{31}$$

Since the angle of the scattered X-rays changes with the wavelength λ, the scattering vector $\mathbf{q}$ is introduced, which is independent of the wavelength λ. The scattering vector $\mathbf{q}$ is defined as the difference between the scattered wave vector $\mathbf{k}_\mathrm{s}$ and the incident wave vector $\mathbf{k}_0$:

$$\mathbf{q} = \mathbf{k}_\mathrm{s} - \mathbf{k}_0 \tag{32}$$

Simple geometric considerations show that

$$\sin \theta = \frac{\left(\frac{q}{2}\right)}{k} \tag{33}$$

Thus, the magnitude of the scattering vector is:[50]

$$q = |\mathbf{q}| = \frac{4\pi}{\lambda} \cdot \sin \theta \tag{34}$$

2.4.3 Form factor and structure factor

As one particle consists of many scattering centers, the scattering of the particle can be explained as the interference pattern of all scattered X-rays, send in the direction of the detector.[47] Summing up all wave amplitudes at each observation angle and squaring this sum gives the scattered intensity as a function of the angle, respectively the scattering vector. This scattering pattern shows an oscillation, which is characteristic for the shape of the particle and is described by the so-called form factor $P(\mathbf{q})$. The form factor is proportional to the square of the Fourier transform of the electron density $\rho(\mathbf{r})$ in the particle.

$$P(\mathbf{q}) = \frac{1}{V_p^{\,2}} \left| \int \rho(\mathbf{r}) \, e^{-\mathrm{i}\mathbf{q}\mathbf{r}} \, \mathrm{d}\mathbf{r} \right|^2 \tag{35}$$

The observed scattering pattern only corresponds to the form factor in a dilute system, where the distances between the particles are large compared to the wavelength, and if all particles are identical in size and shape.[48] In this case, the scattered intensity of a single particle can be calculated from the intensity of the incident beam I_0 multiplied by the form factor $P(\mathbf{q})$, the squared particle volume V_p, and the squared the electron density difference $\Delta\rho$:

$$I_p(\mathbf{q}) = I_0 \cdot (\Delta\rho)^2 \cdot V_p^{\,2} \cdot P(\mathbf{q}) \tag{36}$$

The electron density difference $\Delta\rho$ represents the contrast of X-ray scattering and describes the difference of the electron densities between the particles and the matrix material. Particles are only visible in X-ray scattering, if their electron density differs from that of the matrix material, otherwise the particles cannot be distinguished from their surroundings.[47]

If the interparticle distance is in the same order of magnitude as the distances inside the particle, the interference pattern not only represents the particle shape, but also contains contributions from neighboring particles.[47] This additional interference pattern multiplies with the form factor of the single particle and is called structure factor $S(\mathbf{q})$, as it contains all the information about the spatial arrangement of the particles.

Consequently, the scattering intensity of the whole sample $I(\mathbf{q})$ is acquired by multiplying the scattering intensity of a single particle by the number of particles N in the sample and by the structure factor $S(\mathbf{q})$.

$$I(\mathbf{q}) = N \cdot I_p(\mathbf{q}) \cdot S(\mathbf{q}) \tag{37}$$

$$I(\mathbf{q}) = I_0 \cdot N \cdot (\Delta\rho)^2 \cdot V_p{}^2 \cdot P(\mathbf{q}) \cdot S(\mathbf{q}) \tag{38}$$

When the particles show a highly ordered and periodic arrangement, the distance d between the particles can be calculated from the q-value of the corresponding peak in the scattering pattern.[47]

$$d = \frac{2\pi}{q} \tag{39}$$

Particles with an anisotropic shape can be orientated and show an alignment in a preferred direction. This can be recognized in the 2D scattering patterns, when the intensity measured along concentric circles around the primary beam is not constant, but instead shows a modulation.[47] For example, fibers exhibit partially orientated structural features, as they are produced under substantial elongational and shear stresses.[51]

2.5 References

1 H. Bruus, *Theoretical microfluidics*, Oxford Univ. Press, Oxford, 2011, vol. 18.

2 P. A. Tipler, G. Mosca and J. Wagner, *Physik. Für Wissenschaftler und Ingenieure*, Springer Berlin Heidelberg, Berlin, Heidelberg, 7th edn., 2015.

3 R. Weber, *Physik. Teil I: Klassische Physik - Experimentelle und theoretische Grundlagen*, B. G. Teubner Verlag / GWV Fachverlage GmbH Wiesbaden, Wiesbaden, 2007.

4 T. M. Squires and S. R. Quake, *Rev. Mod. Phys.*, 2005, **77**, 977–1026.

5 G. M. Whitesides and A. D. Stroock, *Physics Today*, 2001, 42–48.

6 D. Meschede, ed., *Gerthsen Physik*, Springer Berlin Heidelberg, Berlin, Heidelberg, 2015.

7 E. M. Purcell, *American Journal of Physics*, 1977, **45**, 3–11.

8 R. J. Poole, *Rheology Bulletin*, 2012, 32–39.

9 J. S. Vrentas, C. M. Jarzebski and J. L. Duda, *AIChE Journal*, 1975, **21**, 894–901.

10 A. Salari and E. Kumacheva, *Macromol. Chem. Phys.*, 2017, **218**, 1600328.

11 M. G. McKee, G. L. Wilkes, R. H. Colby and T. E. Long, *Macromolecules*, 2004, **37**, 1760–1767.

12 L. Kong and G. R. Ziegler, *Biomacromolecules*, 2012, **13**, 2247–2253.

13 S. L. Shenoy, W. D. Bates, H. L. Frisch and G. E. Wnek, *Polymer*, 2005, **46**, 3372–3384.

14 M. Doi, *Journal of Polymer Science: Polymer Letters Edition*, 1981, **19**, 265–273.

15 S. Seibt, S. With, A. Bernet, H.-W. Schmidt and S. Förster, *Langmuir: the ACS journal of surfaces and colloids*, 2018, **34**, 5535–5544.

16 M. Herbst, E. Hofmann and S. Förster, *Langmuir*, 2019, **35**, 11702–11709.

17 J. N. Lee, C. Park and G. M. Whitesides, *Analytical chemistry*, 2003, **75**, 6544–6554.

18 B.-Y. Kim, L.-Y. Hong, Y.-M. Chung, D.-P. Kim and C.-S. Lee, *Adv. Funct. Mater.*, 2009, **19**, 3796–3803.

19 G. M. Whitesides, *Nature*, 2006, **442**, 368–373.

20 S. K. Sia and G. M. Whitesides, *Electrophoresis*, 2003, **24**, 3563–3576.

21 Y. Xia and G. M. Whitesides, *Angewandte Chemie International Edition*, 1998, **37**, 550–575.

22 J. C. McDonald, D. C. Duffy, J. R. Anderson, D. T. Chiu, H. Wu, O. J. A. Schueller and G. M. Whitesides, *Electrophoresis*, 2000, 27–40.

23 J. C. McDonald and G. M. Whitesides, *Acc. Chem. Res.*, 2002, **35**, 491–499.

24 J. R. Anderson, D. T. Chiu, R. J. Jackman, O. Cherniavskaya, J. C. McDonald, H. Wu, S. H. Whitesides and G. M. Whitesides, *Anal. Chem.*, 2000, **72**, 3158–3164.

25 D. C. Duffy, J. C. McDonald, O. J. Schueller and G. M. Whitesides, *Analytical chemistry*, 1998, **70**, 4974–4984.

26 D. B. Weibel, M. Kruithof, S. Potenta, S. K. Sia, A. Lee and G. M. Whitesides, *Analytical chemistry*, 2005, **77**, 4726–4733.

27 J. N. Lee, C. Park and G. M. Whitesides, *Analytical chemistry*, 2003, **75**, 6544–6554.

28 R. Martinez-Duarte and M. J. Madou, in *Microfluidics and Nanofluidics Handbook. Fabrication, Implementation, and Applications*, ed. Sushanta K. Mitra, Suman Chakraborty, CRC Press, 1st edn., 2017, pp. 231–268.

29 J. L. Dektar and N. P. Hacker, *Journal of the American Chemical Society*, 1990, **112**, 6004–6015.

30 R. Daunton, A. J. Gallant and D. Wood, *J. Micromech. Microeng.*, 2012, **22**, 75016.

31 JD PHOTO DATA, *4" Chrome Photomask,* available at: https://www.jd-photodata.co.uk/photomask/chrome-photomasks/4-x-4-x-0060-low-reflection-chrome-on-soda-lime-glass.html, accessed 25 November 2018.

32 Y. Xia and G. M. Whitesides, *Annu. Rev. Mater. Sci.*, 1998, **28**, 153–184.

33 J. C. McDonald and G. M. Whitesides, *Acc. Chem. Res.*, 2002, **35**, 491–499.

34 M. Morra, E. Occhiello, R. Marola, F. Garbassi, P. Humphrey and D. Johnson, *Journal of Colloid and Interface Science*, 1990, **137**, 11–24.

35 J. Kim, M. K. Chaudhury and M. J. Owen, *Journal of Colloid and Interface Science*, 2000, **226**, 231–236.

36 F. Horsch, *3D-Druck für alle. Der Do-it-yourself-Guide*, Hanser, München, 2014.

37 C. M. B. Ho, S. H. Ng, K. H. H. Li and Y.-J. Yoon, *Lab on a chip*, 2015, **15**, 3627–3637.

38 N. Bhattacharjee, A. Urrios, S. Kang and A. Folch, *Lab on a chip*, 2016, **16**, 1720–1742.

39 A. K. Au, W. Huynh, L. F. Horowitz and A. Folch, *Angewandte Chemie (International ed. in English)*, 2016, **55**, 3862–3881.

40 Y. Hwang, O. H. Paydar and R. N. Candler, *Sensors and Actuators A: Physical*, 2015, **226**, 137–142.

41 A. J. L. Morgan, L. Hidalgo San Jose, W. D. Jamieson, J. M. Wymant, B. Song, P. Stephens, D. A. Barrow and O. K. Castell, *PloS one*, 2016, **11**, e0152023.

42 S. Waheed, J. M. Cabot, N. P. Macdonald, T. Lewis, R. M. Guijt, B. Paull and M. C. Breadmore, *Lab on a chip*, 2016, **16**, 1993–2013.

43 R. Amin, S. Knowlton, A. Hart, B. Yenilmez, F. Ghaderinezhad, S. Katebifar, M. Messina, A. Khademhosseini and S. Tasoglu, *Biofabrication*, 2016, **8**, 22001.

44 C. I. Rogers, K. Qaderi, A. T. Woolley and G. P. Nordin, *Biomicrofluidics*, 2015, **9**, 16501.

45 G. Nelson, R. A. Kirian, U. Weierstall, N. A. Zatsepin, T. Faragó, T. Baumbach, F. Wilde, F. B. P. Niesler, B. Zimmer, I. Ishigami, M. Hikita, S. Bajt, S.-R. Yeh, D. L. Rousseau, H. N. Chapman, J. C. H. Spence and M. Heymann, *Optics express*, 2016, **24**, 11515–11530.

46   S. S. Crump, *US Patent*, 5121329A, 09.06.1992.

47   H. Schnablegger and Y. Singh, *The SAXS Guide. Getting acquainted with the principles*, Anton Paar GmbH, 3ʳᵈ edn., 2013.

48   N. Stribeck, *X-Ray Scattering of Soft Matter*, Springer Berlin Heidelberg, Berlin, Heidelberg, 2007.

49   W. H. Bragg and W. L. Bragg, *Proceedings of the Royal Society A: Mathematical, Physical and Engineering Sciences*, 1913, **88**, 428–438.

50   O. Glatter and O. Kratky, eds., *Small angle X-ray scattering*, Acad. Pr, London, 1982.

51   M. Hummel, A. Michud, S. Asaadi, Y. Ma, L. K. J. Hauru, E. Hartikainen and H. Sixta, *Annual transactions of the Nordic Rheology Society*, 2015, **23**, 13–20.

3 Thesis Overview

3.1 Outline

After an introduction to microfluidics and this thesis (chapter 1), an overview of the fundamentals (chapter 2), on which this thesis is built, the later chapters 4-6 will present the experimental findings and their interpretation in form of three peer-reviewed publications, which are reprinted as a whole. These publications contribute to the methodical advancement of microfluidic devices for the purpose of spinning microfibers and the fundamental understanding of structure formation in the process of fiber spinning. The present chapter 3 gives short summaries of the aforementioned publications and elucidates their role in the superordinate theme of this thesis.

3.2 Synopsis

The primary aim of this thesis was to identify and exploit the potential of using microfluidic devices for spinning of microfibers.

Microfluidics already showed its potential in different research areas like modern medicine, biology, and chemistry. Moreover, microfluidics found its way into various applications due to its key benefits, which come along with the laminar flow. Beside the small sample volume needed, defined and controlled conditions in space and time are obtained. This allows not only to fabricate fibers of uniform diameter and endless length in a steady and controlled process, but also to gain insights on the formation of fibrous microstructure by applying suitable methods.

Two different methods of conventional fiber spinning were identified, which could be adapted for a microfluidic approach and make use of the key advantages microfluidics has to offer. Both spinning methods are sub-variants of solution spinning, namely wet and dry spinning. These processes have in common that the natural or synthetic polymer, which should be spun, is dissolved in a solvent. The spinning solution is jetted through a spinneret in a surrounding medium, thereupon, the macromolecules orientate, the solvent is removed, and a solid fiber is formed.

In wet spinning, the spinning solution is extruded into a bath of a non-solvent, which forces the polymer to precipitate by solvent exchange. Alternatively, gelation or cross-linking could be triggered by a stimulus like a change of the pH value or ionic concentration. When transferring this process to microfluidics, the formation of the fiber happens inside the microfluidic device by hydrodynamic flow focusing. The spinning solution is focused into a flow of defined size by using a second liquid, which induces precipitation. Having control

over channel design and flow rates means having also control over fiber size, shear forces, concentration, and pH value within the channel, which are important parameters for the formation of fibers with excellent mechanical properties.

The second approach for microfluidic fiber spinning is a special variant of dry spinning, which is called solution blow spinning. Here, the surrounding medium is pressurized air. The spinning solution is ejected from a nozzle, the solvent evaporates, and the polymer fiber remains. In our variant, the nozzle was substituted by a microfluidic nozzle device accompanied by the aforementioned benefits of a highly controllable process. The fast-flowing stream of air confines the spinning solution and acts as a virtual nozzle, which can be adjusted by the air pressure. In contrast to wet spinning, the fiber formation happens outside of the microfluidic device.

The first publication, presented in chapter 4, demonstrated what microfluidic wet spinning is capable of. It was shown for the first time, that it is possible to produce endless microfibers made from pure collagen type I with diameters down to $3\,\mu m$ by using our microfluidic approach. Irreversible clogging of the assembling collagen could be prevented by reducing wall adhesion with our elaborate channel geometry, resulting in a continuous and adjustable process. Thus, the fabricated fibers had the smallest diameter, which had been reported for wet-spun collagen fibers and showed extraordinary mechanical properties, exceeding the stability of previous wet-spun collagen fibers as well as even natural tendon. Additionally, due to the nontoxic, all-aqueous conditions, the collagen fibers could be potentially useful for directed axonal growth of neuronal cells.

In the second publication, presented in chapter 5, micro solution blow spinning (μSBS) was established as a technique for spinning of ultrafine fibers with precise diameter control. This spinning technique is a further development of dry spinning, which uses a stream of pressurized air not only to solidify the jetted polymer solution, but also to control the diameter and velocity of the liquid jet. Accordingly, equations could be deduced from hydrodynamics and mass balance, which relate the fiber diameter to the controllable system parameters, in particular to volume flow rate and pressure difference. Thus, it is possible to quantitatively predict the final diameter of the fiber as demonstrated by using the fluoroplastic terpolymer THV as a model system to produce uniform fibers with virtually endless length.

The third publication, presented in chapter 6, made use of the previously established technique of micro solution blow spinning (μSBS) in order to control polymer microfiber structure. By combining fiber spinning experiments with small- and wide-angle X-ray scattering (SAXS, WAXS) the macroscopic spinning conditions could be related directly to the molecular structure of the resulting fibers. For this purpose, the orientational order

parameter was determined by simulating the 2D-SAXS patterns and comparing them to the measured ones. The elongational rate of the jetted fiber was found to be a crucial parameter, which impacts the internal macromolecular alignment. Additional tensile testing experiments revealed that the well-defined shish–kebab crystal structure of the microfibers evolves into an extended chain crystal structure upon plastic deformation.

3.3 Content of individual publications

3.3.1 Summary of chapter 4

Microfluidics-produced collagen fibers show extraordinary mechanical properties

In chapter 4, a microfluidic device is used for wet spinning of collagen fibers. Collagen microfibers are in the focus of biomedical research, since this biodegradable, biocompatible, and hypoallergenic biomaterial can be used in drug-delivery and tissue engineering applications. Thus, researchers have great interest in producing collagen microfibers of small diameter and with good mechanical properties in a stable and continuous process. This can be achieved by this microfluidic approach.

The microfluidic device was fabricated using established lithography techniques. First, a master structure is produced via photolithography in a clean room, then this master acts as a mold for uncured poly(dimethylsiloxane), which is cross-linked afterwards. The finalized microfluidic device contains a cross junction of two microchannels. This cross junction has three inlets and one outlet and can be used for hydrodynamic flow focusing.

The central channel delivers the spinning solution, consisting of collagen type I dissolved in diluted acetic acid at pH 3. The spinning solution is focused from the side channels by an aqueous buffer solution (pH 8), which consists of 112 mM phosphate, 30 mM TES, 135 mM NaCl, and 10% (w/v) polyethylene glycol (PEG). When both solutions come in contact at the cross junction, the acidic collagen solution is neutralized, water is removed by the hygroscopic PEG and consequently, the formation of fibrils is triggered, which align in the elongational flow and form microfibers. A special three-dimensional channel design is used at the cross junction to avoid sticking of the assembling collagen to the channel walls, which is usually followed by irreversible clogging. The buffer solution forms a sheath flow around the inner collagen solution and prevents the collagen from wall contact. The produced microfiber is rinsed by pulling through a water bath and collected on a rotating spool (see Fig. 1A).
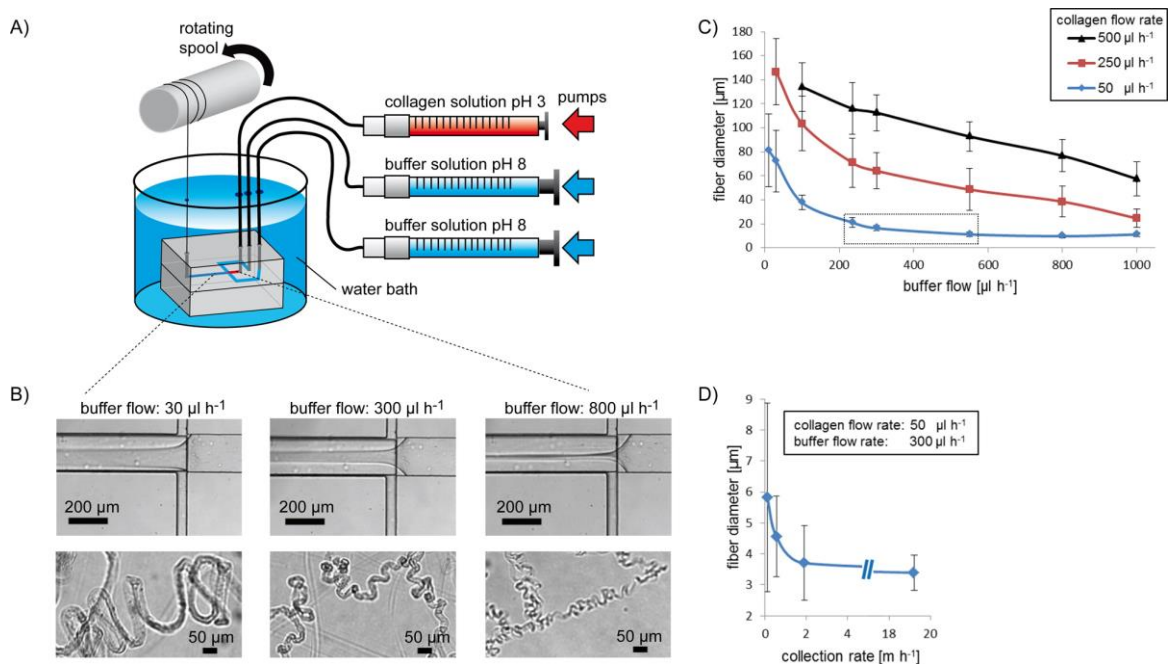
Figure 1: (A) A microfluidic device is connected to three syringe pumps, which deliver the collagen and the buffer solutions for spinning. The collagen microfiber is produced by hydrodynamic flow focusing at the cross junction of the microchannels and extruded in a water bath afterwards, from where it is collected and poststretched by a rotating spool. (B) The diameter of the fiber can be adjusted by varying the buffer flow rate at a fixed flow rate of 50 µL/h for the collagen solution. (C) Diameters of the fibers depend on the volumetric flow rates of both the collagen and the buffer solution. The box indicates the set of parameters, where collecting the fiber by the automated spool is feasible. (D) The final diameter of the dried fiber can be further reduced by changing the collection rate of the spool.

As the flow rates of the individual channels can be adjusted by using syringe pumps, it is possible to control the diameter of the resulting fiber. In Fig. 1B, the influence of the buffer flow rate can be seen in the microscopic images of flow profile at the cross junction and the corresponding images of the final fibers before spooling. The graph of Fig. 1C shows the range of diameters, that can be achieved by varying the buffer flow rate between 30 µL/h and 1000 µL/h at three fixed collagen flow rates of 50 µL/h, 250 µL/h and 500 µL/h.

Collecting the fiber on a rotating spool causes poststretching, which leads to even smaller diameters. For example, the diameter of the microfiber decreases from 16 µm without poststretching to a minimum diameter of 3-4 µm above a collection rate of 1.92 m/h at flow rates of 50 µL/h for the collagen solution and 300 µL/h for the buffer solution (see graph in Fig. 1D).

Optical microscopy and scanning electron microscopy allow to measure the diameters of the fibers exactly, moreover, SEM reveals small aligned grooves along the fiber axis indicating an orientation of collagen fibrils within the microfiber. In order to gain further information about the molecular alignment, the microfibers were examined by polarized Fourier-transform infrared spectroscopy (FTIR). The ratios of the amide I/amide II peak areas in perpendicular and parallel polarization also indicate a good collagen fibril

orientation. So, the mechanical properties of the microfibers were investigated by tensile testing at 30% humidity in more detail and it became apparent that the produced collagen microfibers are superior to classical wet-spun collagen fibers and even to natural fibers of tendon. The tensile strength of 383 ± 85 MPa and the Young's modulus of 4138 ± 512 MPa of the microfluidics-produced collagen fibers exceed the respective ones of previous wet-spun collagen fibers. However, it has been shown that collagen fibers with better mechanical properties can be produced, but it requires chemical cross-linking, which may come along with disadvantages like cytotoxicity. In contrast, this microfluidic setup allows the continuous spinning of mechanically stable microfibers of pure collagen type I and a diameter of only 3.7 ± 1.2 µm under nontoxic, all-aqueous conditions.

As further characterization, the thermal stability of the air-dried microfibers was tested using differential scanning calorimetry (DSC) and thermogravimetric analysis (TGA), confirming the suitability for biomedical applications at human body temperature.

Additionally, some initial cell culture experiments were performed by incubating cells of the neuronal cell line NG108-15 in contact to the microfibers for 72 h. As the cells migrated directionally along the longitudinal axis and showed axonal growth in direction of the fiber, these collagen microfibers could be potentially useful in peripheral nerve repair.

3.3.2   Summary of chapter 5

Microfluidic nozzle device for ultrafine fiber solution blow spinning with precise diameter control

In chapter 5, a new technique for controlled continuous spinning of uniform microfibers is presented, which is called micro solution blow spinning (μSBS). Ultrafine fibers of virtually endless length and with diameters smaller than 2 µm can be produced in a continuous and steady process. In comparison to electrospinning, this method imposes less requirements concerning the spinning setup and the properties of the spinning solution. The key element in μSBS is the microfluidic nozzle, which adds high control over processing parameters and nozzle geometry to the process of solution blow spinning. Therefore, the diameter of the fibers can be controlled precisely and even predicted quantitatively.

The microfluidic nozzle devices can be fabricated from PDMS by using established photolithography and soft lithography techniques. This allows to freely construct a flow-optimized nozzle design and set width and height of all microchannels. A PDMS device is shown in Fig. 2A, which contains an array of four identical nozzles next to each other.

The gas dynamic virtual nozzle (GDVN)-principle is applied to create a liquid jet by focusing the spinning solution using pressurized air. The air pressure influences the size of the liquid jet and the jet velocity. The scheme in Fig. 2B illustrates how the polymer solution is focused perpendicular from the sides by the pressurized air. The layered three-dimensional architecture of the nozzle ensures that the air encloses the jetted polymer

solution from all sides and hereby, it prevents sticking of the polymer to the channel walls. The virtual nozzle, which is created by the fast-flowing air, is much smaller than the physical channel dimensions, allowing to fabricate ultrafine fibers of even smaller diameter.

As spinning solutions, a fluorinated terpolymer, called THV, dissolved in acetone and poly(caprolactone) dissolved in hexafluoroisopropyl alcohol (HFIP) were used. An important aspect for the polymer solution is, that the solvent should exhibit a fast evaporation time. When the solvent evaporates from the jetted polymer solution, a solid fiber is formed in mid-air, which is collected on a rotating cork spool afterwards (Fig. 2C). By changing the rotational speed, the fiber can be stretched additionally during the spinning process. The microfibers can not only be collected as a filament yarn (Fig. 2D) but also deposited as a non-woven mesh directly on a substrate (Fig. 2E).

The fiber samples were examined by scanning electron microscopy (SEM) in order to analyze and evaluate the diameters of the fibers statistically. A narrow size distribution was observed for THV fibers proving a steady spinning process (see Fig. 2F).

The SEM images also reveal that the morphology and the surface structure of the fibers depend on the evaporating time of the solvent and can be influenced by adjusting the process parameters.
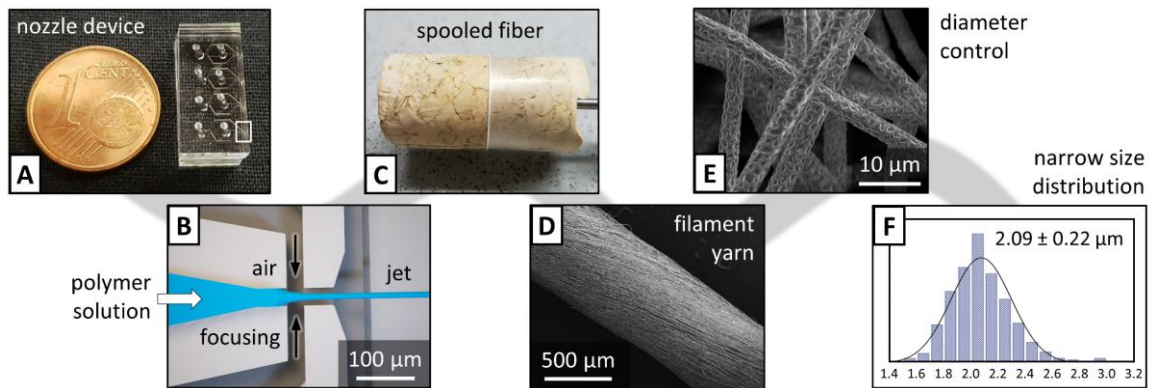

Figure 2: Inside of a microfluidic device made of PDMS (A) the polymer solution is focused by pressurized air into a liquid jet (B). When the solvent evaporates from the spinning solution, a microfiber is formed in mid-air, which can be collected on a rotating cork spool (C). This ultrafine fiber is either bundled into a filament yarn (D) or can be applied directly on a substrate as non-woven mesh (E). The histogram shows the narrow diameter distibution of THV fibers at process parameters of Q = 1.0 mL/h, Δp = 2.0 bar, v_s = 7.7 m/s, d_s = 8 cm, 20% (v/v) THV in acetone (F).

A major advancement of μSBS is that the fiber diameter d_f can be calculated by eq. (1):

$$d_f = \sqrt{\frac{4 \cdot \phi_T \cdot Q}{\pi \cdot v_f}} \tag{1}$$

The fiber diameter depends only on the flow rate Q, the volume fraction of THV ϕ_T in the polymer solution, and the fiber velocity v_f, which is either equal to the jet velocity v_j or the drawing speed of the spool v_s, depending on which is the faster one.

$$v_f = \begin{cases} v_j & \text{, if } v_j \geq v_s \\ v_s & \text{, if } v_j < v_s \end{cases} \tag{2}$$

The velocity of the jet v_j is determined by the pressure drop Δp of the compressed air, which are both connected by Bernoulli's equation for incompressible flows. Hence, an equation for the fiber diameter without poststretching of the fiber can be derived:

$$d_f = \left(\frac{8 \cdot \rho_0 \cdot \phi_T{}^2 \cdot Q^2}{\pi^2 \cdot \Delta p} \right)^{1/4} \tag{3}$$

A correction factor accounts for a systematic deviation since the pressure difference was not measured directly at the nozzle in this spinning setup.

The evaluation of the SEM images verified that the fiber diameter is proportional to $Q^{1/2}$ and $v_f{}^{-1/2}$, respectively to $\Delta p^{-1/4}$, as shown in the graphs in Fig. 3. The dashed lines indicate the calculated fiber diameter according to eq. (1), which match quite well the measured values.
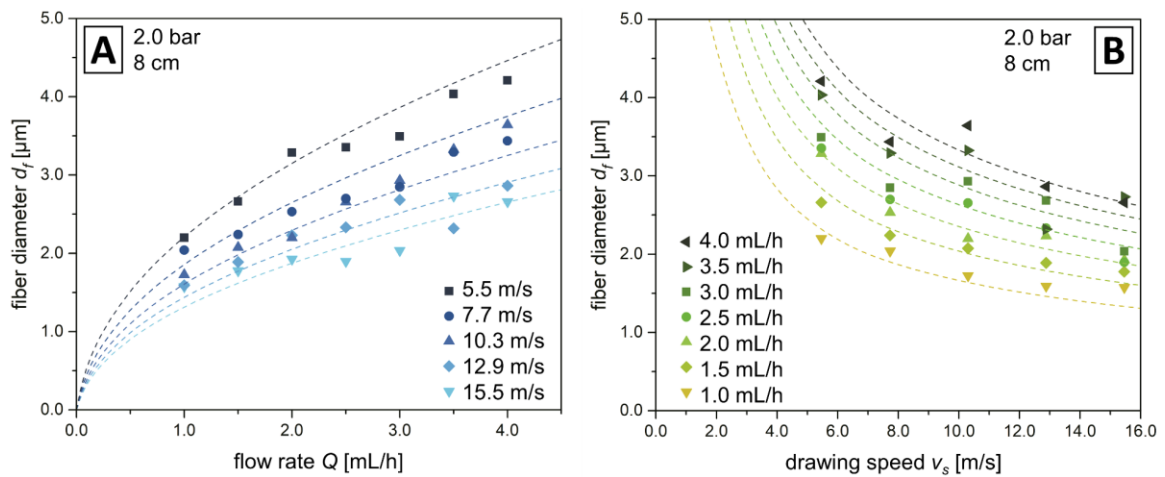

Figure 3: The graphs show the measured mean diameter of THV fiber samples as a function of (A) the flow rate and (B) the drawing speed of the spool. The dashed lines display the theoretical proportionality of the fiber diameter, calculated by eq. (1).

The diameter of the jet and the fiber exhibit the same proportionality of $Q^{1/2}$ and $v_f{}^{-1/2}$, since both differ just in the factor $\phi_T{}^{1/2}$ due to evaporation of the solvent. This was proved by measuring the diameter of the liquid jet when it exits the nozzle.

An important parameter is the distance between the nozzle and the spool, as the spool needs to be positioned beyond a certain distance from the nozzle to allow for sufficient solvent evaporation. Otherwise, the wet fibers fuse and no individual fibers are obtained.

The velocity of the liquid jet, which is equal to the velocity of the fiber, could only be measured by using a high-speed camera. That way, it was verified that the velocity is, for example, 6.13 m/s at a volume flow rate of 1 mL/h. At this production rate, over 22 km of microfiber can be produced in 1 h.

3.3.3   Summary of chapter 6

Controlling polymer microfiber structure by micro solution blow spinning

In chapter 6, the previously established technique of micro solution blow spinning is combined with small- and wide-angle X-ray scattering (SAXS, WAXS) to relate the spinning conditions to the bulk and molecular structure of the resulting fibers. The excellent adjustability of all relevant process parameters in μSBS allows to control not only the fiber diameter, but also the internal crystalline alignment, which determines the mechanical properties. It became apparent that the elongational rate is the decisive parameter that transduces the nozzle flow conditions to the local macromolecular structure and orientation. For this study, the prior introduced microfluidic nozzle devices were used, which were fabricated from PDMS by lithographic techniques and rely on the gas dynamic virtual nozzle principle to produce micron-sized fibers in a continuous and stable process. As spinning solution, the fluorinated terpolymer THV was dissolved in acetone with 20% (w/w). The polymer solution is focused by pressurized air inside of the nozzle and forms a liquid jet, which upon evaporation of the solvent solidifies and turns into a microfiber. The ejected fiber is collected by a rotating spool, which can stretch the fiber, as the rotational frequency is adjustable.

The process of fiber formation can be divided into four characteristic sections. The most important parameters are the velocities and diameters of (i) the solution inside the nozzle, (ii) the liquid jet, (iii) the emerging fiber before, and (iv) after drawing. The equations for these sections are listed in Table 1.

Table 1: Equations for the diameter and the velocity at the four relevant sections of fiber formation. Q: volumetric flow rate, Δp: pressure difference, ρ_0: density of spinning solution, ϕ_T: volume fraction of THV, f_j: proportionality factor, d_{spool}: diameter of spool, v_{spool}: rotational frequency.

section	diameter	velocity	remarks
nozzle exit	w_n, h_n	$v_n = \dfrac{Q}{w_n \cdot h_n}$	diameter set by nozzle design
free jet	$d_j = \sqrt{\dfrac{4 \cdot Q}{\pi \cdot v_j}}$	$v_j = f_j \cdot \sqrt{\dfrac{2 \cdot \Delta p}{\rho_0}}$	velocity set by pressure
free fiber	$d_f = \sqrt{\phi_T} \cdot d_j$	$v_f = v_j$	assuming complete evaporation
spooled fiber	$d_s = \sqrt{\dfrac{4 \cdot \phi_T \cdot Q}{\pi \cdot v_s}}$	$v_s = d_{spool}\pi \cdot v_{spool}$	velocity set by spool

The evaporation time of the solvent defines the length of the section, in which the free fiber is still susceptible for stretching. Considering this, the elongational rate should depend on the volumetric flow rate and the velocities of the jet and the spool.

$$\dot{\varepsilon} = \frac{\Delta v}{\Delta x} \propto \frac{v_s - v_j}{v_s + v_j} \cdot \frac{v_j}{Q} \tag{4}$$
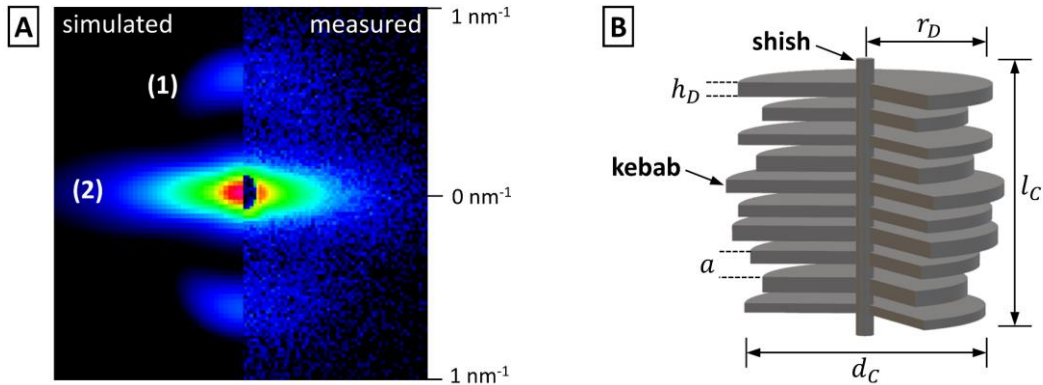
Figure 4: (A) Simulated and measured 2D-SAXS pattern of THV fibers: (1) meridional Bragg peaks, (2) equatorial scattering; (B) Definition of the parameters of the shish–kebab model, which is proposed for the semi-crystalline THV polymer fibers.

The influence of the spinning parameters on the microstructure of the THV fiber was studied by small-angle X-ray scattering. Therefore, 2D-SAXS patterns were simulated using the software *Scatter*, that matches the measured scattering patterns of various fiber samples (Fig. 4A). The proposed model for the semi-crystallin polymer is a shish–kebab structure, consisting of thin cylinders, representing the shishs, which are oriented in fiber direction, and stacks of disks representing the kebabs (Fig. 4B). The equatorial scattering arises from cylindrical or primary fibril structures, which are aligned along the fiber axis and the meridional Bragg reflexes originate from the stacks of lamellar disks, which represent folded chain crystals. From the orientational distribution function of the shish–kebabs the orientational order parameter can be derived:

$$S = \frac{1}{2} < 3\cos^2\theta - 1 > \tag{5}$$

In the experiments, an increasing alignment of the crystalline domains was observed for high draw ratios v_s/v_j, which should have a maximum at $v_s/v_j \sim 2.4$. At draw ratios $v_s/v_j > 2$ values of the orientational order parameter of up to $S = 0.95$ were achieved.

In Fig. 5A, the quantitative relation between the macroscopic flow parameters and the degree of molecular orientation of the microfibers is shown, as the orientational order parameter S is plotted against the extensional rate $\dot{\varepsilon}$, given by eq. (4).

For $v_s > v_j$, the orientational order increases until it reaches a nearly constant plateau value. For $v_s < v_j$, there is no additional acceleration and thereby extension of the jetted fiber, causing the orientational order parameter to stay on a constant base level. This shows that the extensional rate is the central parameter, which determines the molecular alignment.
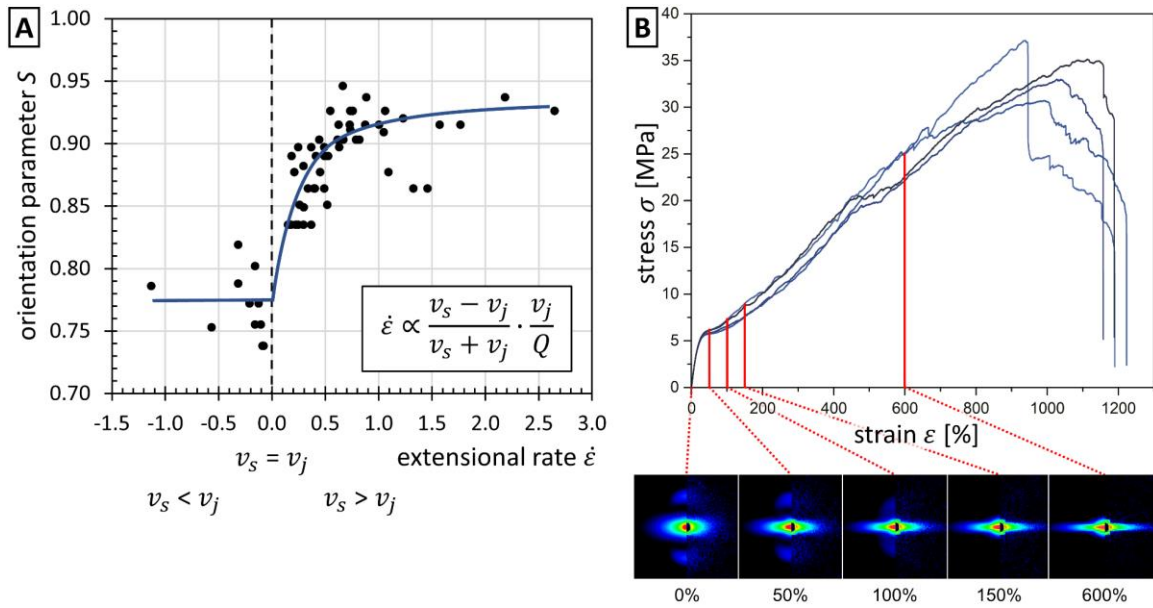
Figure 5: (A) Plot of the orientational order parameter versus the extensional rate; (B) Engineering stress-strain curves for THV filament yarns together with the corresponding SAXS patterns at the selected strains.

A requirement for fibers with high orientational order is an adequate distance between nozzle and spool. The solvent needs enough time to evaporate completely, while the extensional forces last, which sets the orientation of the aligned microfibrils in the fiber. Stress-strain curves were measured to acquire the mechanical data of THV fiber bundles. The values are in a typical range for rubbery materials. Of particular interest were the microstructural changes during deformation, that could be derived from the measured 2D-SAXS patterns at different strain values (Fig. 5B). Upon deformation, the intensity of the meridional Bragg peaks decreases, while the peak position shifts to lower q. This increase in disk-spacing together with a disappearance of disks results from a transformation of the lamellae of folded chains within the disks into fibrils of extended chains. Simultaneously, the amorphous layers between the crystalline lamellae get extended. At even higher strains, the shish–kebab structure transforms into an extended chain crystal structure, which can be plastically deformed up to high elongations of 1000-1200%. The increasing crystalline orientation along the fiber axis is also confirmed by WAXS measurements.

3.4 Individual contributions to joint publications

The results presented in the scientific papers of this thesis are based on the collaborative work with other scientists and have been published in peer-reviewed journals. The contribution of each co-author is specified in further detail below. The corresponding author is indicated by an asterisk (*).

Chapter 4

"Microfluidics-produced collagen fibers show extraordinary mechanical properties"
by Christian Haynl, Eddie Hofmann, Kiran Pawar, Stephan Förster, Thomas Scheibel*

This paper is published in *Nano Lett.*, **2016**, *16* (9), 5917–5922.

I carried out various pretests with spider silk and alginate to optimize microfluidic channel designs and select a suitable one. I designed and fabricated the microfluidic devices for the most part and supervised the fabrication of the other part. I introduced Christian Haynl to microfluidic wet spinning, supported him by scientific discussions and proof-read the manuscript. Christian Haynl performed all final experiments, analyzed the data and wrote the manuscript for the paper. Kiran Pawar conducted the cell culture experiments, which included cultivating, staining and microscoping the nerve cells. Stephan Förster was involved in scientific discussions and proof-reading of the manuscript. Thomas Scheibel supervised the project and corrected the manuscript.

Chapter 5

"Microfluidic nozzle device for ultrafine fiber solution blow spinning with precise diameter control"
by Eddie Hofmann, Kilian Krüger, Christian Haynl, Thomas Scheibel, Martin Trebbin, Stephan Förster*

This paper is published in *Lab Chip*, **2018**, 18, 2225–2234.

I performed all experiments, analyzed the data, prepared the figures, and wrote the manuscript for the paper. Stephan Förster supervised the project, supported by scientific discussions and proof-read the manuscript. Kilian Krüger performed first pretests and supported by scientific discussions. Martin Trebbin gave the initial idea for this project and proof-read the manuscript. Christian Haynl gave the idea for spinning PCL fibers, performed first pretests and provided the spinning solution. Thomas Scheibel was involved in scientific discussions and proof-read the manuscript.

Chapter 6

"Controlling polymer microfiber structure by micro solution blow spinning"

by Eddie Hofmann, Kilian Krüger, Martin Dulle, Xiaojian Liao, Andreas Greiner, Stephan Förster*

I performed all experiments of fiber spinning and SAXS measurements, analyzed the data, prepared the figures, and wrote the manuscript for the paper. Stephan Förster supervised the project, helped with scientific discussions and supplemented the manuscript. Kilian Krüger supported by scientific discussions and performed complementary rheological testing of the spinning solution. Martin Dulle conducted the WAXS measurements and helped to discuss the results. Xiaojian Liao performed the tensile testing of the fibers. Andreas Greiner proof-read the manuscript.

4 Microfluidics-produced collagen fibers show extraordinary mechanical properties[1]

Christian Haynl,[†] Eddie Hofmann,[‡] Kiran Pawar,[†] Stephan Förster,[‡,∥,¶]
Thomas Scheibel[†,∥,¶,§,#,⊥]

[†] Lehrstuhl Biomaterialien, Fakultät für Ingenieurwissenschaften, Universität Bayreuth, Universitätsstraße 30, 95440 Bayreuth, Germany.

[‡] Lehrstuhl Physikalische Chemie I, Universität Bayreuth, Universitätsstraße 30, 95440 Bayreuth, Germany.

[∥] Bayreuther Zentrum für Kolloide und Grenzflächen (BZKG), Universität Bayreuth, Universitätsstraße 30, 95440 Bayreuth, Germany.

[¶] Bayerisches Polymerinstitut (BPI), Universitätsstraße 30, 95440 Bayreuth, Germany.

[§] Bayreuther Zentrum für Molekulare Biowissenschaften (BZMB), Universität Bayreuth, Universitätsstraße 30, 95440 Bayreuth, Germany.

[#] Institut für Bio-Makromoleküle (bio-mac), Universität Bayreuth, Universitätsstraße 30, 95440 Bayreuth, Germany.

[⊥] Bayreuther Materialzentrum (BayMAT), Universität Bayreuth, Universitätsstraße 30, 95440 Bayreuth, Germany.
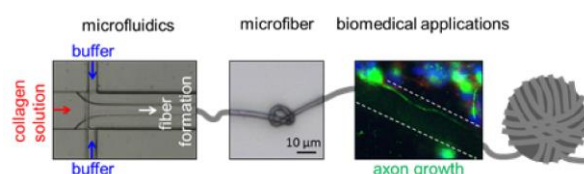
4.1   Abstract

Collagens are widely used as biomaterials in drug-delivery and tissue engineering applications due to their biodegradability, biocompatibility and hypoallergenicity. Besides gelatin-based materials, collagen microfibers are in the focus of biomedical research. Commonly, man-made fibers are produced by wet-spinning yielding fiber diameters higher than 8 μm. Here, assembly and continuous production of single collagen type I microfibers were established using a microfluidic chip. Microfluidics-produced microfibers exhibited tensile strength and Young's modulus exceeding that of fibers produced in classical wet-spinning devices and even that of natural tendon and they showed lower diameters. Their structural orientation was examined by polarized Fourier transform infrared spectroscopy (FTIR) showing fibril alignment within the microfiber. Cell culture tests using the neuronal cell line NG108-15 showed cell alignment and axon growth along the microfiber axes inaugurating potential applications in, for example, peripheral nerve repair.

4.2   Body

Protein fibers in nature are used for a great diversity of tasks including motility, scaffolding, stabilization, and protection.[1] One of the most abundant structural proteins is collagen mainly contributing to the extracellular matrix of vertebrates.[2,3] So far, more than 20 distinct types of collagen have been described. Thereof, collagen type I is the major collagen of tendon, ligament, skin, and bone and therefore the most studied one.[4] On the molecular level, collagen type I forms a characteristic triple helix consisting of three polypeptides termed α-chains (two α1[I] and one α2[I]). Previous examinations showed that a high amino acid homology exists between both types of α-chains, however the α1(I) chain comprises a lower hydrophobicity compared to the α2(I) chain.[5] Each α-chain exhibits a helical core domain mainly consisting of the repeating amino acid motif Gly-Xaa-Yaa (Xaa and Yaa could be any amino acid, but mostly proline and hydroxyproline residues are found) and flanking nonrepetitive sequences.[4,6-8] These triple-helical molecules self-assemble into fibrils and fibers in an entropy-driven process including the reduction of the contact area to the surrounding water.[6,9] Because of collagen's good mechanical stability, biocompatibility, biodegradability, low immunogenicity, and ability to promote cellular attachment and growth, collagenous materials, especially fibers, are used in medical and biomedical applications such as drug-delivery, wound healing, and tissue engineering.[10-14]

Up to now, numerous publications reported the processing of soluble collagen into fibers using wet-spinning devices.[13,15-19] Here, collagen microfibers were fabricated using a microfluidic system. In general, microfluidics deals with the processing of small amounts of fluids in channels with dimensions of tens to hundreds of micrometer,[20] which are mostly

embedded in small chips regularly consisting of polydimethylsiloxane (PDMS). Besides analytical applications, microfluidic systems were shown to be suitable to fabricate fibers of synthetic polymers, polysaccharides such as chitosan or alginate and silk.[21,22] With regard to collagen type I, previous studies dealt with microfluidic channels acting either as a mold for the discontinuous collagen fibril formation[23] or as an environment for in situ analysis of collagen gelation.[24] Nevertheless, up to now microfluidic spinning did not allow to continuously fabricate collagen fibers due to its significant longer gelation/assembly time (minutes to hours),[25] which is in contrast to the very fast ionic cross-linking of polysaccharides such as chitosan and alginate. However, microfluidic fiber spinning methods were already used to incorporate collagen within polysaccharide fibers. Usually, chitosan or alginate have been used as a scaffold in which collagen was embedded, for example, as blended fibers[26] or as tubular fibers with a collagen hydrogel core[25] or simply coated onto the fiber surface.[27] Nevertheless, the production of endless, plain collagen fibers would be highly desirable due to a better performance in comparison to blended fibers including an expected higher mechanical stability, better biocompatibility, and less complexity in processing compared to polysaccharide-collagen blend fibers.
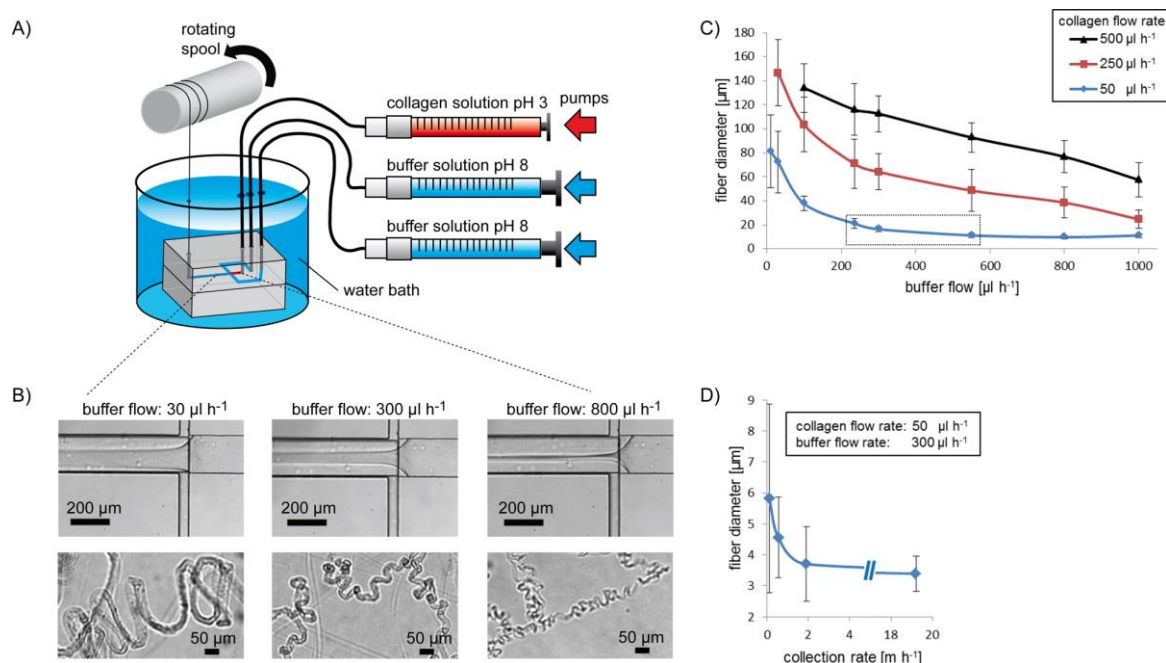

Figure 1: (A) A microfluidic chip is connected to three independent syringe pumps that allow simultaneous pumping of a collagen solution at pH 3 (red) and two PEG-containing buffer solutions at pH 8 (blue). Microfiber formation takes place at the cross junction within the microfluidic chip upon an increase of the pH and in the presence of PEG, and microfibers are extruded into a water bath and drawn by an automated spool. (B) Using a constant collagen flow (here, 50 μL h–1) and varying buffer flow rates enables the extrusion of microfibers into water with adjustable diameters. (C) Diameters of extruded fibers depend on buffer and collagen flow rates. Collection of collagen fibers using a rotating spool is possible for a collagen flow of 50 μL h–1 and buffer flow rates in between 235 and 550 μL h–1 (shown by the box). (D) Dry microfiber diameters could be adjusted by changing the collection rate using a constant collagen flow of 50 μL h–1 and a buffer flow rate of 300 μL h–1 yielding final diameters from 6 to 3 μm.

In this study, we introduce a microfluidic approach for the continuous production of adjustable collagen microfibers yielding minimum dry diameters of only 3 μm. Polarized Fourier transform infrared spectroscopy (FTIR) revealed fibril orientation along the microfiber axis supposed to be in part responsible for the excellent mechanical stability exceeding that of natural tendon fibers and previous wet-spun collagen fibers. Cell studies using the neuronal cell line NG108-15 showed directional cell growth and even axon elongation along the fiber axes. Therefore, we conclude that these fibers are of high interest for biomedical applications, especially for the use in peripheral nerve repair.

In order to produce endless collagen microfibers, we used a microfluidic device featuring one inlet channel for the collagen solution and two inlet channels for the sheath flows joining at a cross junction (90° angle) into one larger channel. A great challenge in producing continuous fibers with microfluidic devices is to reduce wall adhesion of the assembling polymer (here collagen) followed by irreversible clogging. Therefore, we designed a microfluidic chip, similar to Kinahan et al.,[22] which contained a tiered channel geometry, thus enabling the circulation of the sheath flow around the protein stream. The microfluidic chip, consisting of polydimethylsiloxane (PDMS), was fabricated by using the soft-lithography technology.
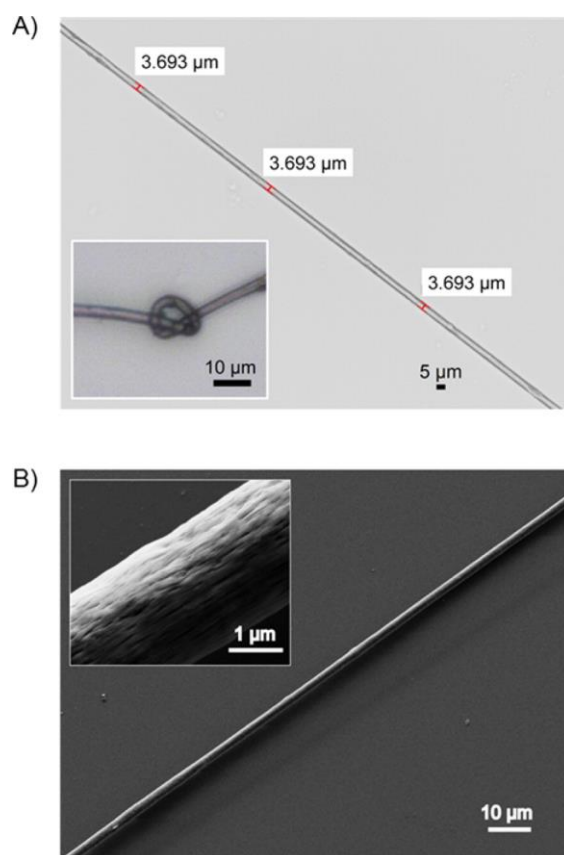

Figure 2: (A) Light-microscopy image of a microfluidics-produced collagen microfiber confirming a homogeneous fiber diameter. (Insert) Man-made knot within the microfiber. (B) SEM picture of a microfluidics-produced collagen microfiber and higher magnification (insert) showing longitudinal grooves.

For microfiber assembly, collagen type I (with triple-helical conformation) was dissolved in diluted acetic acid at pH 3, and as sheath flows a buffer solution (112 mM phosphate, 30 mM TES, and 135 mM NaCl, pH 8) with 10% (w/v) polyethylene glycol (PEG) was used. The interaction between both types of solution at the cross intersection induced a neutralization of the collagen solution due to the high buffering capacity of the PEG solution. Shifting an acidic collagen type I solution to slightly basic conditions triggers the formation of fibrils.[28,29] As a result of the hydrodynamic focusing and the elongational flow in the microfluidic chip, fibrils were aligned and assembled into microfibers. Surprisingly, it was observed that the addition of polyethylene glycol to the surrounding buffer was essential for continuous microfiber formation, likely depending on the high hygroscopicity of PEG,[30] which contributes to protein precipitation by rapidly detracting water molecules therefrom.[31,32] Microfibers at the chip's exit were pulled through a water bath by a rotating spool to remove buffer components and PEG (Figure 1A). Washing-off of PEG from the microfibers was confirmed by Fourier transform infrared (FTIR) spectroscopy yielding spectra lacking the characteristic PEG signal at 1100 cm^{-1} (Figure 3B). Furthermore, water extrusion avoided the formation of spindle-knotted fiber morphologies, usually occurring when outer fiber layers are still liquid and breakup due to Rayleigh instabilities,[33-35] and microfibers exhibiting a homogeneous diameter along their longitudinal axes were generated (Figure 2). Because fiber morphology usually depends on the hydrodynamic focusing of the core solution within microchannels, we were able to extrude microfibers with varying diameters by changing the collagen and/or the buffer flow rates. As shown in Figure 1B,C, the diameter of extruded microfibers decreased upon increasing the buffer flow rates while applying a constant collagen flow. On the contrary, an increase of the collagen flow rate led to higher fiber diameters (Figure 1C). Using 250 or 500 µL h^{-1} collagen flows in combination with buffer flow rates lower than 30 respectively 100 µL h^{-1} prevented the extrusion of fibers exhibiting a well-defined fiber shape with a homogeneous diameter. Furthermore, it was noticed that the microfiber diameter after extrusion differed from the diameter of the hydrodynamically focused collagen stream at the cross-intersection. This could be attributed to the low fibrillogenesis rate of collagen,[25] supposedly inhibiting immediate hardening of the forming microfiber at the cross-intersection. For instance, by applying a constant collagen flow of 50 µL h^{-1} and 30, 300, and 800 µL h^{-1} buffer flows, the relative decline in microfiber diameter between the focusing zone and the outlet was 36, 74 and 74%, respectively. Collection of microfibers using a rotating spool was feasible for a collagen flow of 50 µL h^{-1} and buffer flow rates in between 235 and 550 µL h^{-1}. Applying lower buffer flow rates than 235 µL h^{-1} (and/or collagen flow rates higher than 50 µL h^{-1}) resulted in a loss of the hydrodynamic focusing of the collagen solution that hindered complete collagen assembly and reduced the shear forces necessary for fabrication of mechanically stable fibers. On the other side, rising the buffer flow rates to values higher than 550 µL h^{-1} (at a collagen flow rate of 50 µL h^{-1}) led

to lower reaction times of collagen with the surrounding buffer solution, thereby inhibiting fiber collection, too. We observed that the collagen fiber collection by the rotating spool caused poststretching leading to even lower diameters. To investigate the effect of the collection rate on microfiber diameter, we used a 50 μL h^{-1} collagen flow and 300 μL h^{-1} buffer flows (which turned out to be the most robust processing condition for continuous fiber production) and varied the speed of the collecting spool (Figure 1D). We noticed that microfibers were stretched even with the lowest collection rate of 0.11 m h^{-1}, and their diameters decreased from original (i.e., no poststretching) 16 μm (see Figure 1C) to 6 μm during collection. The high standard deviation at slow collection rates could be explained by undirected agglomeration of extruded fibers hindering collection of untangled fibers (Figure S1 in Supporting Information). Microfibers drawn at a collection rate above 1.92 m h^{-1} resulted in fiber diameters of 3–4 μm, which obviously indicated that the maximum stretching capacity was reached. Continuous microfiber production was possible up to 19 m h^{-1}.
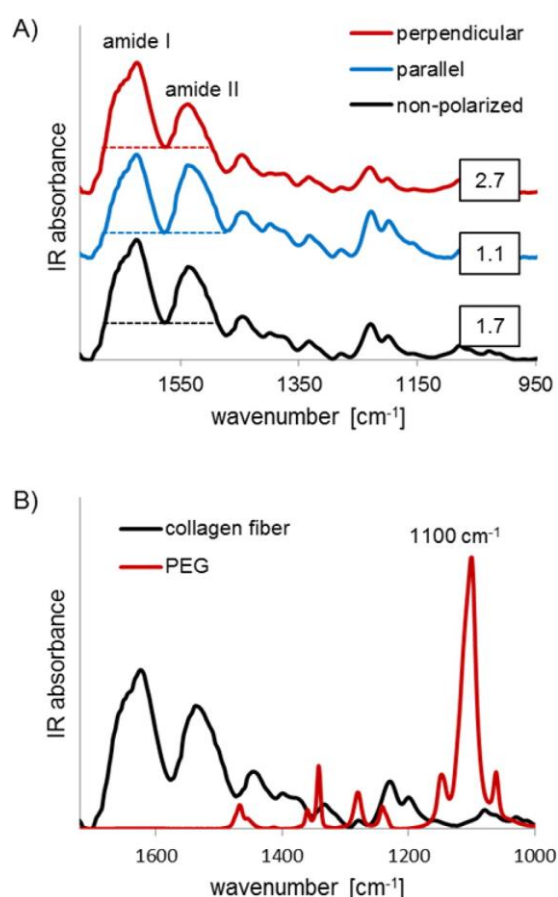

Figure 3: (A) Polarized FTIR spectroscopy of a microfluidics-produced collagen microfiber. The ratios of the amide I/amide II peak area change upon exposure to IR radiation polarized perpendicular or in parallel to the microfiber axis and under nonpolarizing conditions (shown in boxes). (B) IR spectrum of a microfluidics-produced collagen microfiber in comparison to that of polyethylene glycol (PEG) indicating that no PEG can be found within the microfiber.

For microfiber characterization, we investigated microfibers produced at 50 μL h^{-1} collagen flow, 300 μL h^{-1} buffer flows and at a collection rate of 1.92 m h^{-1} (if not otherwise indicated). Light microscopy of collagen microfibers revealed that the fiber diameter was constant at 3.7 μm (Figure 2A). Scanning electron microscopy (SEM) allowed identifying small aligned grooves along the microfiber axis indicating an orientation of collagen fibrils within the microfiber (Figure 2B).

In order to test the molecule alignment as well as the structural integrity of the microfibers, polarized FTIR spectroscopy was used. Polarized FTIR is a technique to get information concerning orientation and/or ordering of molecules.[36] Former studies indicated that the ratio of the amide I and amide II peak area of collagenous tissues changes when examined using polarized infrared light from different angles due to the molecular dichroism.[36,37] Here, it was observed that microfibers exposed to polarized radiation exhibited a ratio of the amide I to amide II peak area of 2.7 when polarized perpendicular to the fiber axis, whereas the amide I/amide II area ratio was 1.1 upon polarization in parallel to the fiber axis, and it was 1.7 at nonpolarizing conditions, thereby indicating good collagen fibril orientation along the microfibers (Figure 3A). In comparison, natural fibers of tendon possess values for perpendicular, parallel and nonpolarized conditions of 4, 1 and 1.8, respectively.[37]

Because the obtained microfibers could be easily hand knotted (Figure 2A, insertion), the mechanical stability of the fibers collected at a rate of 1.92 m h^{-1} was obviously quite good. Therefore, the mechanical properties of collagen microfibers were investigated by tensile testing at 30% humidity in more detail. Figure 4A shows a representative stress–strain curve of the obtained microfibers at the detected optimal processing conditions. Tensile strength of microfluidics-produced collagen microfibers was 383 ± 85 MPa and superior to that of tendon as well as of classically wet-spun collagen type I fibers. Moreover, the Young's modulus was also significantly higher (4138 ± 512 MPa) in comparison to that of tendon and artificial collagen fibers, while the extensibility of $25.0 \pm 3.7\%$ was similar between all fibers (Table 1). Fiber toughness was calculated to be 52.9 ± 14.7 MJ m^{-3}. Importantly, the average microfiber diameter was 3.7 ± 1.2 μm denoting the lowest fiber diameter ever published for wet-spun collagen fibers (≥ 8 μm).[13,15,17-19] Collagen microfibers collected at nonoptimal conditions, for example, at a rate of only 0.11 m h^{-1} led to lower tensile strength (361 ± 126 MPa) and Young's modulus (3201 ± 1026 MPa) (Figure S2 in Supporting Information). Although Yaari *et al.* recently produced wet-spun collagen fibers achieving a tensile strength of 378 MPa and a Young's modulus of 3.5 GPa, additional glutaraldehyde cross-linking of these fibers was required.[19] However, glutaraldehyde cross-linking is markedly cytotoxic,[15,38] and therefore, only EDC/NHS cross-linked fibers exhibiting 314 MPa tensile strength were used in Yaari *et al.* for cell culture applications.[19] In contrast, we did not need any chemical cross-linking to yield

mechanically stable fibers. In addition, our microfluidic setup allowed the spinning of low concentrated collagen solutions with as little as 5 mg mL^{-1}. Such concentrations lead to a decrease in viscosity enabling enhanced fibril movement and more distinct alignment.[15]

It can be assumed that the smaller diameters of our microfibers led to increased mechanical stability due to better longitudinal orientation of collagen fibrils[18] and less defect structures like voids, entanglements, free chain ends, and foreign particles in contrast to the situation in bigger diameter fibers.[39] To confirm this, we had a closer look at the mechanical properties of collagen microfibers with varying diameters ranging from 5 to 10 µm with an average diameter of 6.8 µm (collected by 0.11 m h^{-1}). Actually, 6.8 µm diameter fibers showed a tensile strength of 284 ± 102 MPa and a Young's modulus of 2900 ± 1100 MPa, both being significantly lower than the mechanical properties of 3.7 µm fibers (for comparison of the mechanical properties see Figure S3 in Supporting Information). The high mechanical stability of our microfibers makes them accessible to the fabrication of textile scaffolds for tissue engineering and suture- or wound-dressing materials, whereas the adaption of the final mechanical properties to its environment could be controlled by the specific textile structure and the type of processing, for example, knitting, weaving, or braiding.

Table 1: Mechanical properties and diameter of microfluidics-produced collagen microfibers ($n = 36$) in comparison to that of collagen fibers after wet-spinning and that of tendon.

material	modulus E [MPa]	strength σ [MPa]	extensibility ε [%]	diameter d [µm]
microfluidics-produced microfiber	4138 ± 512	383 ± 85	25.0 ± 3.7	3.7 ± 1.2
wet-spun fibers:				
Dunn *et al.*, 1993[18]	-	200	-	20
Cavallaro *et al.*, 1994[17]	-	224	-	≥ 25
Zeugolis *et al.*, 2008[13]	1580	208	27.0	119
Siriwardane *et al.*, 2014[15]	1265	262	18.4	46.5
fibers of tendon:				
Hepworth *et al.*, 2002[43]	2410	180	25.6	254
Gosline *et al.*, 2002[44]	1200	120	13	-

Next, the thermal stability of air-dried microfluidics-produced microfibers was characterized using differential scanning calorimetry (DSC) and thermogravimetric analysis (TGA). DSC measurements of the microfibers showed an endothermic peak at

59 °C referring to helix-to-coil transition (Figure 4B).[40-42] TGA revealed a residual internal water content of 3%, which was indicated by weight loss upon 98 °C, and the microfibers were thermally stable up to 178 °C before further weight loss occurred in a multistage decomposition manner (Figure 4C). As a result, the microfluidics-produced collagen microfibers were suitable concerning biomedical or tissue engineering applications usually only requiring human body temperature stability.

Because the microfluidics-produced collagen microfibers exhibited explicit mechanical stability and thermal characteristics and because collagen is known to be biocompatible[10,12] with biochemical cues allowing cell attachment,[45] we tested our microfibers in initial cell culture experiments. Exemplary, the neuronal cell line NG108-15 was analyzed in contact
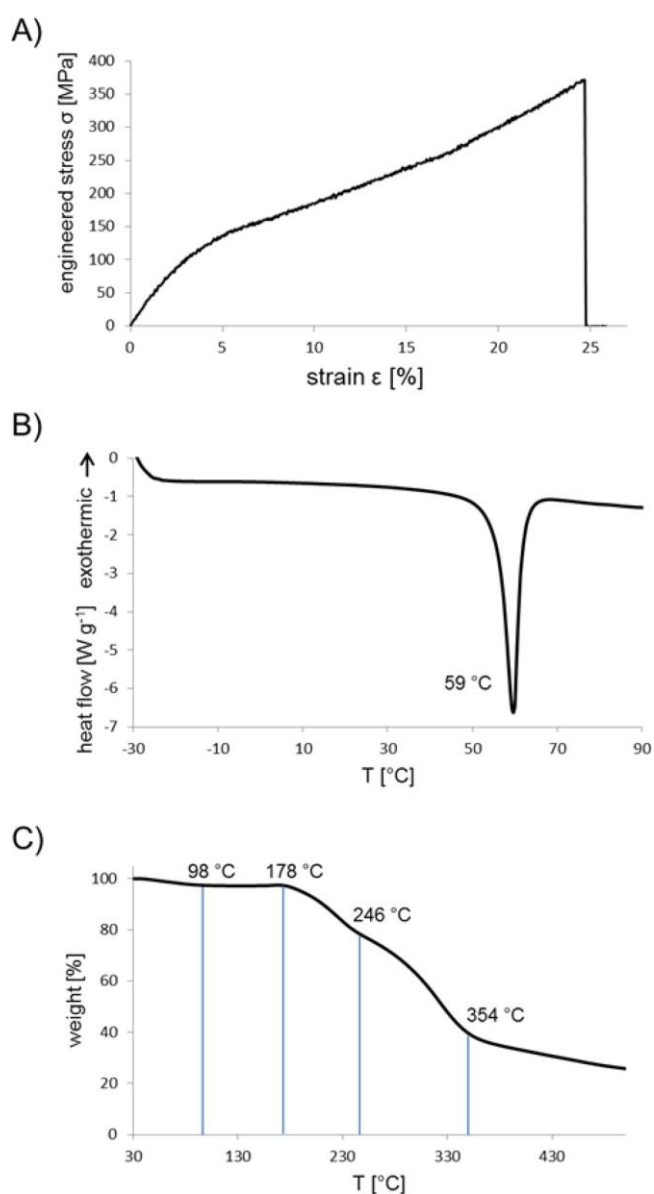
Figure 4: Representative stress–strain plot, (B) DSC analysis, and (C) TGA of dry microfluidics-produced collagen microfibers.

to our microfibers after 72 h of incubation. Low-magnification fluorescence images of cell nuclei marked with DAPI showed cell alignment along the collagen microfiber's longitudinal axes (Figure 5A). To get more detailed information about the cell morphology, higher-magnification phase contrast (Figure 5B), and fluorescence images (Figure 5B–F) were taken. DAPI-stained cell nuclei (Figure 5C) and phalloidin-labeled actin filaments (Figure 5D) revealed the general cell morphology in contact to microfibers. Cells were additionally labeled with an antibody against ßIII-tubulin, which is almost found exclusively in neuronal cell structures. Interestingly, we observed that cells exhibited axon growth. Axons were up to 100 μm in length and were aligned in microfiber direction (Figure 5E, white arrows). Figure 5F depicts merged fluorescence of all three channels.
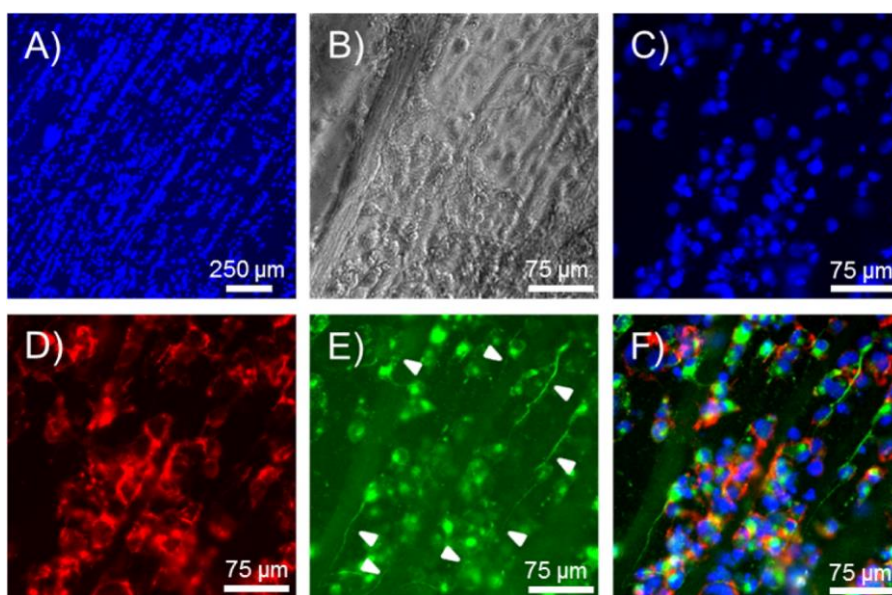

Figure 5: Cell culture analysis of neuronal NG108-15 cells on microfluidics-produced collagen microfibers after 72 h of incubation. (A) Fluorescence image of DAPI-stained cells. Cells align along the microfibers axes. (B) Phase-contrast image of cells on microfibers. Fluorescence images of (C) DAPI- and (D) phalloidin-stained cells in the presence of microfibers. (E) Immuno-staining of neuronal-specific ßIII-tubulin indicates axon growth in direction of the microfiber axes (white arrows). (F) Merged fluorescence image of (C), (D), and (E).

Although recently progress was made concerning the production of polysaccharide fibers using microfluidics,[21,25-27] the microfluidic fabrication of collagen fibers has so far been less manageable because of the slow gelling rate of collagen. Here, the continuous assembly of acid-soluble collagen type I into microfibers was performed by microfluidics with asymmetric hydrodynamic focusing. The determination of appropriate assembly conditions and flow rates allowed the production of microfibers under nontoxic, all-aqueous conditions, and a maximum production rate of 19 m h^{-1}. These microfibers exhibited good mechanical properties exceeding the stability of previous wet-spun collagen fibers as well as even natural tendon without the need of chemical cross-linking, which could be harmful to cells. The high mechanical stability of our microfibers facilitates fiber processing, which allow textile fabrication and adjustment of the resulting mechanical textile properties to its

respective application, for example, tendon repair. Neuronal NG108-15 cells migrated directionally along the longitudinal microfiber axes and showed axonal growth in direction of the microfiber axis. Therefore, these microfibers could be potentially useful in peripheral nerve repair to bridge long distance gaps allowing directional growth of neuronal cells for developing functional tissue. On the other side, according to little material consumption by our microfluidic approach (1 mg collagen $\triangleq$ 76 m microfiber using a collection rate of 19 m h^{-1}), our setup is also of high importance for screening different fiber additives, for example, matrix proteins or polymers with regard to their functionality in collagen microfibers including their influence on mechanical properties or biocompatibility.

Associated Content

The Supporting Information is available free of charge on the ACS Publications website at DOI: 10.1021/acs.nanolett.6b02828.
Materials and Methods. Light microscopic image showing fiber agglomeration by using slow collection rates (Figure S1). Comparison of the mechanical properties of collagen microfibers collected at 0.11 and 1.92 m h^{-1} (Figure S2) and of collagen microfibers with average diameters of 3.7 and 6.8 μm (Figure S3)

Author Information

Corresponding Author

*E-mail: thomas.scheibel@bm.uni-bayreuth.de

Notes
The authors declare no competing financial interest.

Acknowledgements

4.3 References

1   Scheibel, T. *Curr Opin Biotechnol*, 2005, **16**, 427–433.

2   Kadler, K. E.; Baldock, C.; Bella, J.; Boot-Handford, R. P. *J Cell Sci*, 2007, **120**, 1955–1958.

3   Zhu, B.; Li, W.; Lewis, R. V.; Segre, C. U.; Wang, R. *Biomacromolecules*, 2014, **16**, 202–213.

4   Gelse, K.; Poschl, E.; Aigner, T. *Adv Drug Deliv Rev*, 2003, **55**, 1531–1546.

5   Kuhn, K. *Connect Tissue Res*, 1982, **10**, 5–10.

6   Kadler, K. E.; Holmes, D. F.; Trotter, J. A.; Chapman, J. A. *Biochem J*, 1996, **316**, 1–11.

7   Shoulders, M. D.; Raines, R. T. *Annu Rev Biochem*, 2009, **78**, 929–958.

8   Lintz, E. S.; Scheibel, T. R. *Adv Funct Mater*, 2013, **23**, 4467–4482.

9   Parkinson, J.; Kadler, K. E.; Brass, A. *J Mol Biol*, 1995, **247**, 823–831.

10   Lee, C. H.; Singla, A.; Lee, Y. *Int J Pharm*, 2001, **221**, 1–22.

11   Maeda, M.; Tani, S.; Sano, A.; Fujioka, K. *J Control Release*, 1999, **62**, 313–324.

12   Parenteau-Bareil, R.; Gauvin, R.; Berthod, F. *Materials*, 2010, **3**, 1863–1887.

13   Zeugolis, D. I.; Paul, R. G.; Attenburrow, G. *J Appl Polym Sci*, 2008, **108**, 2886–2894.

14   Hagenau, A.; Suhre, M. H.; Scheibel, T. R. *Prog Polym Sci*, 2014, **39**, 1564–1583.

15   Siriwardane, M. L.; DeRosa, K.; Collins, G.; Pfister, B. J. *Biofabrication*, 2014, **6**, 015012.

16   Caves, J. M.; Kumar, V. A.; Wen, J.; Cui, W.; Martinez, A.; Apkarian, R.; Coats, J. E.; Berland, K.; Chaikof, E. L. *J Biomed Mater Res B Appl Biomater*, 2010, **93**, 24–38.

17   Cavallaro, J. F.; Kemp, P. D.; Kraus, K. H. *Biotechnol Bioeng*, 1994, **43**, 781–791.

18   Dunn, M. G.; Avasarala, P. N.; Zawadsky, J. P. *J Biomed Mater Res*, 1993, **27**, 1545–1552.

19   Yaari, A.; Schilt, Y.; Tamburu, C.; Raviv, U.; Shoseyov, O. *Acs Biomater-Sci Eng*, 2016, **2**, 349–360.

20   Whitesides, G. M. *Nature*, 2006, **442**, 368–373.

21   Jun, Y.; Kang, E.; Chae, S.; Lee, S. H. *Lab Chip*, 2014, **14**, 2145–2160.

22   Kinahan, M. E.; Filippidi, E.; Koster, S.; Hu, X.; Evans, H. M.; Pfohl, T.; Kaplan, D. L.; Wong, J. *Biomacromolecules*, 2011, **12**, 1504–1511.

23   Lee, P.; Lin, R.; Moon, J.; Lee, L. P. *Biomed Microdevices*, 2006, **8**, 35–41.

24   Koster, S.; Evans, H. M.; Wong, J. Y.; Pfohl, T. *Biomacromolecules*, 2008, **9**, 199–207.

25   Onoe, H.; Okitsu, T.; Itou, A.; Kato-Negishi, M.; Gojo, R.; Kiriya, D.; Sato, K.; Miura, S.; Iwanaga, S.; Kuribayashi-Shigetomi, K.; Matsunaga, Y. T.; Shimoyama, Y.; Takeuchi, S. *Nat Mater*, 2013, **12**, 584–590.

26   Jun, Y.; Kim, M. J.; Hwang, Y. H.; Jeon, E. A.; Kang, A. R.; Lee, S. H.; Lee, D. Y. *Biomaterials*, 2013, **34**, 8122–8130.

27   Yeh, C. H.; Lin, P. W.; Lin, Y. C. *Microfluid Nanofluid*, 2010, **8**, 115–121.

28   Williams, B. R.; Gelman, R. A.; Poppke, D. C.; Piez, K. A. *J Biol Chem*, 1978, **253**, 6578–6585.

29   Silver, F. H. *Journal of Biological Chemistry*, 1981, **256**, 4973–4977.

30   Doblhofer, E.; Heidebrecht, A.; Scheibel, T. *Appl Microbiol Biotechnol*, 2015, **99**, 9361–9380.

31   Ingham, K. C. *Arch Biochem Biophys*, 1978, **186**, 106–113.

32   Honig, W.; Kula, M. R. *Anal Biochem*, 1976, **72**, 502–512.

33   Chen, Y.; Wang, L.; Xue, Y.; Jiang, L.; Zheng, Y. *Sci Rep*, 2013, **3**, 2927.

34   Tian, X.; Chen, Y.; Zheng, Y.; Bai, H.; Jiang, L. *Adv Mater*, 2011, **23**, 5486–5491.

35   Bai, H.; Sun, R.; Ju, J.; Yao, X.; Zheng, Y.; Jiang, L. *Small*, 2011, **7**, 3429–3433.

36   Nguyen, T. T.; Eklouh-Molinier, C.; Sebiskveradze, D.; Feru, J.; Terryn, C.; Manfait, M.; Brassart-Pasco, S.; Piot, O. *Analyst*, 2014, **139**, 2482–2488.

37   Bi, X.; Li, G.; Doty, S. B.; Camacho, N. P. *Osteoarthritis Cartilage*, 2005, **13**, 1050–1058.

38   Huanglee, L. L. H.; Cheung, D. T.; Nimni, M. E. *J Biomed Mater Res*, 1990, **24**, 1185–1201.

39   Chae, H. G.; Kumar, S. *Science*, 2008, **319**, 908–909.

40   Miles, C. A.; Ghelashvili, M. *Biophys J*, 1999, **76**, 3243–3252.

41   Walton, R. S.; Brand, D. D.; Czernuszka, J. T. *J Mater Sci-Mater M*, 2010, **21**, 451–461.

42   Arafat, M. T.; Tronci, G.; Yin, J.; Wood, D. J.; Russell, S. J. *Polymer*, 2015, **77**, 102–112.

43   Hepworth, D. G.; Smith, J. P. *Compos Part a-Appl S*, 2002, **33**, 797–803.

44   Gosline, J.; Lillie, M.; Carrington, E.; Guerette, P.; Ortlepp, C.; Savage, K. *Philos Trans R Soc Lond B Biol Sci*, 2002, **357**, 121–132.

45   Kwak, E. A.; Ahn, S.; Jaworski, J. *Biomacromolecules*, 2015, **16**, 1761–1770.

4.4 Supporting Information

4.4.1 Materials and Methods

Microfluidic collagen microfiber production

Acid-soluble collagen type I extracted from calf skin was purchased from Sigma Aldrich Life Sciences. Collagen was dissolved in diluted acetic acid at pH 3 for 20 hours. The solution was centrifuged for 10 min at 17000 x g, and the supernatant was removed for further experimentation (4.8 mg ml^{-1}). For microfiber formation, a buffer solution was prepared with 10% (w/v) PEG 20000, 4.14 mg ml^{-1} $NaH_2PO_4 \cdot 2\,H_2O$, 12.1 mg ml^{-1} Na_2HPO_4, 6.86 mg ml^{-1} TES (2-[(2-Hydroxy-1,1-bis(hydroxymethyl)ethyl)amino]-ethane-sulfonic acid) and 7.89 mg ml^{-1} NaCl and adjusted to pH 8 using NaOH.[1] The microfluidic chip device enabling asymmetric hydrodynamic focusing of the collagen solution was designed and produced similarly to Kinahan *et al.*, 2011.[2] In brief, the chips consisted of a top and a bottom layer each contributing to the microchannel structure. PDMS (Sylgard® 184, Dow Corning) was mixed in a curing-agent-to-base ratio of 1:10, poured onto a silicon wafer acting as a microchannel stamp and degassed for 2 h. After incubation in an oven for 2 h at 75 °C, holes were punched into the upper chip half for creating inlets for the tubes. Subsequently, both halves were cleaned with isopropanol and dried in an air flow before applying them to a plasma oven (MiniFlecto® PC-MFC, Plasma Technology GmbH) for 30 s, 0.5 mbar, 64 W and an air supply of 10 sccm. Small water droplets were pipetted onto the two chip halves, and both were fitted to each other using a light microscope. Finally, the bonded chips were dried in an oven over night at 35 °C. The inlet channel for the collagen solution was 200 µm wide and 60 µm high. The inlet channel for the buffer was 50 µm wide and 150 µm high. The channel after the cross intersection possessed a size of 200 µm in width and 210 µm in height.

FTIR spectroscopy

Polarized FTIR spectra of collagen microfibers were taken on a Bruker Tensor 27 IR spectroscope connected to a hyperion unit. Microfibers were produced and air-dried at room temperature for 3 days. Subsequently, microfibers were fixed to plastic frames and were exposed either to non-polarized or polarized (parallel or perpendicular to longitudinal microfiber axis) radiation. The resolution was 4 cm^{-1}. Peak areas of the amide I and amide II bands were integrated, and the ratio of the amide I to amide II peak area was calculated. The IR spectrum of polyethylene glycol (PEG) was measured on a Bruker Tensor 27 using an ATR module and a resolution of 4 cm^{-1}.

Tensile test

Mechanical measurements of air-dried (3 days) microfibers, fixed to plastic frames (gauge length of 2 mm) with a high-viscosity acrylate glue, were carried out at 30% humidity on a tensile testing machine (Bose Electroforce 3220 equipped with a 0.49 N load cell) using an extension rate of 0.3 mm min^{-1}. Engineered stress σ was calculated as the force divided by the cross-sectional area assumed to be circular. The cross-sectional area was calculated upon measuring the microfiber diameter at ten different positions. Strain ε was defined as the change in microfiber length divided by its original length. Young's modulus E was determined as the slope of the stress-strain curve in the linear elastic deformation range (2% strain). Microfiber toughness was assessed by integration of the stress-strain plot using Origin 8.1G.

Microscopy

Microfibers were air-dried for 3 days at room temperature and SEM pictures of platinum sputtered microfibers (2 nm platinum coating) were taken using a Zeiss 1540 EsB CrossBeam. Light microscopy was carried out using a Leica Microscope DMI 3000B.

Thermal characterization

Microfibers were air-dried for 3 days at room temperature. Differential scanning calorimetry (DSC) was conducted on a DSC1 (Mettler Toledo) by applying 1.3 mg of fibers under nitrogen-atmosphere conditions and a heating rate of 20 °C min^{-1}. Thermal weight loss was examined using thermogravimetric analysis (TGA) (TGA/SDTA 851e System). Curves were generated under oxygen-atmosphere conditions at a heating rate of 10 °C min^{-1} using 3.9 mg of sample.

Cell culture

Microfibers for cell culture testing were continuously collected on metal frames as aligned fibers and sterilized with UV light treatment for 30 min. The neuronal cell line NG108-15 was obtained from the European Collection of Cell Culture (ECACC) and grown in complete Dulbecco's Modified Eagle Medium (DMEM) (Biochrom) containing 10% (v/v) fetal bovine serum (Biochrom), 2 mM GlutaMAX (Gibco) and 1% gentamicin in a humidified atmosphere with 5% CO_2 at 37 °C. Cells were trypsinized for experiments after they became 80–90% confluent and cells were seeded directly on microfibers at a density of 104 cells cm^{-2} in a small amount of complete medium without serum in order to induce axon growth.[3,4] After 30 min of incubation, additional medium was added lacking serum. At day three (72 h) of incubation with 5% CO_2 at 37 °C, the culture medium was removed, and cells were fixed with 4% paraformaldehyde (PFA). Fixed cells were permeabilized using 0.1% Triton X-100 (Sigma Aldrich) in phosphate buffered saline (PBS) (Sigma

Aldrich) followed by blocking with 5% bovine serum albumin (BSA) (Sigma Aldrich) in PBS. The primary rabbit antibody anti-ßIII-tubulin (polyclonal) (abcam) for detection of neuronal-specific cell structures was diluted 1:1000 in 0.1% Triton X-100 in PBS, and cells were incubated for 2 h at room temperature. Subsequently, the secondary antibody Alexa fluor 488 goat anti-rabbit (1:1000 dilution in PBS with 0.1% Triton X-100) (Invitrogen) was applied for further 2 h to detect the primary antibody. In order to detect actin filaments and cell nuclei, phalloidin (TRITC) (Sigma Aldrich) and Hoechst 33258 pentahydrate (Invitrogen) were used. Samples were imaged by using a fluorescence microscope (Leica DMi8). Experiments were carried out in non-treated culture plates (Thermo Scientific).

4.4.2   References

1   Caves, J. M.; Kumar, V. A.; Wen, J.; Cui, W.; Martinez, A.; Apkarian, R.; Coats, J. E.; Berland, K.; Chaikof, E. L. *J Biomed Mater Res B Appl Biomater*, 2010, **93**, 24–38.

2   Kinahan, M. E.; Filippidi, E.; Koster, S.; Hu, X.; Evans, H. M.; Pfohl, T.; Kaplan, D. L.; Wong, *J. Biomacromolecules*, 2011, **12**, 1504–1511.

3   Pun, S.; Yang, J. F.; Ng, Y. P.; Tsim, K. W. K. *Febs Lett*, 1997, **418**, 275–281.

4   Dhir, V.; Natarajan, A.; Stancescu, M.; Chunder, A.; Bhargava, N.; Das, M.; Zhai, L.; Molnar, P. *Biotechnol Progr*, 2009, **25**, 594–603.
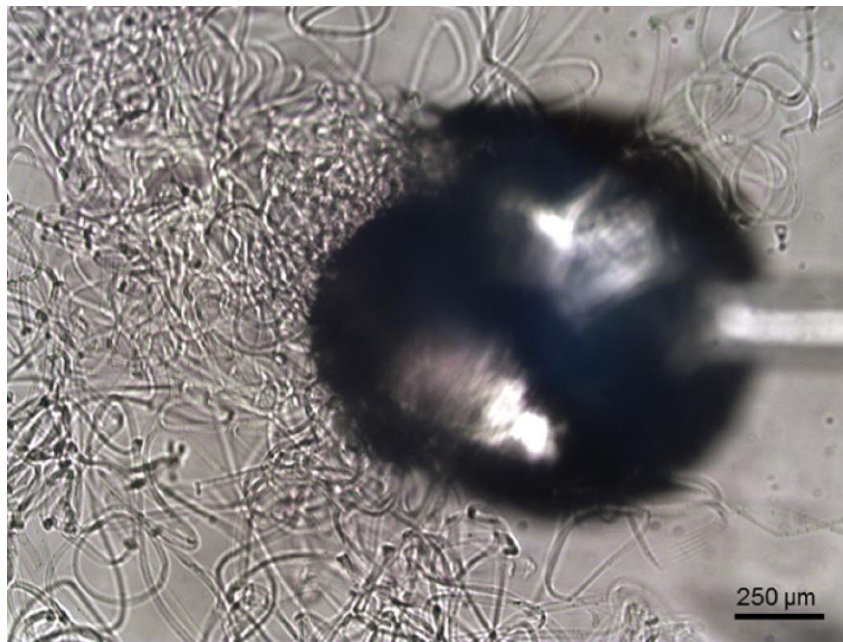
Figure S1: Light-microscopic image of the collagen fiber extrusion from the microfluidic chip outlet (black area) without collecting them on a rotating spool. Extruded fibers form agglomerations/entanglements due to absent (or slow) collection rates.
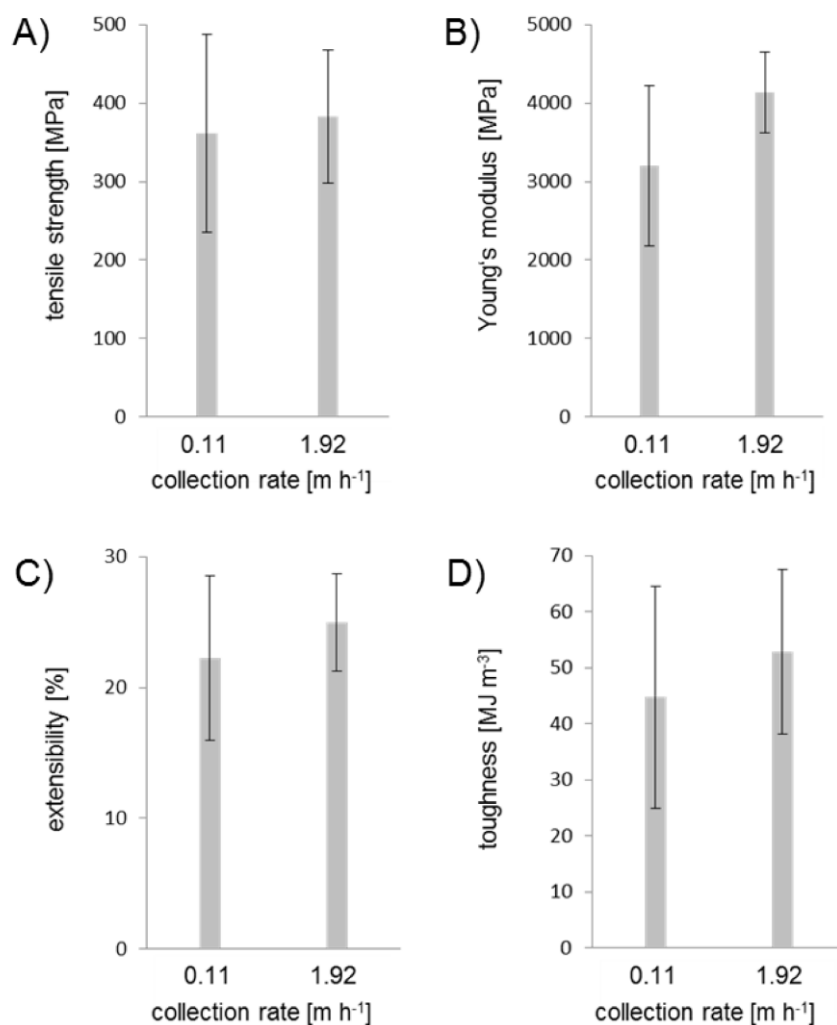
Figure S2: Comparison of the mechanical properties of collagen fibers drawn at a collection rate of 0.11 m h^{-1} versus 1.92 m h^{-1}. (A) Tensile strength, (B) Young's modulus, (C) extensibility and (D) toughness. Error bars indicate the standard deviation.
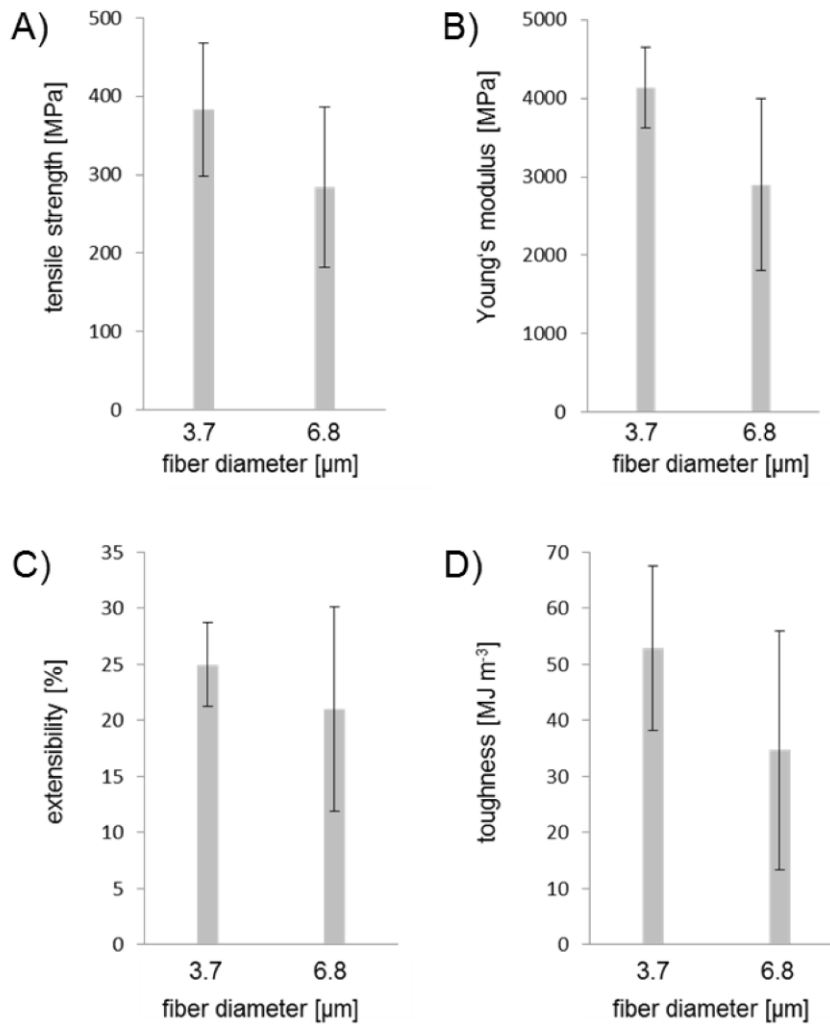
Figure S3: Comparison of the mechanical properties of collagen fibers having fiber diameters of 3.7 ± 1.2 µm and 6.8 ± 1.9 µm. (A) Tensile strength, (B) Young's modulus, (C) extensibility and (D) toughness. Error bars indicate the standard deviation.

5 Microfluidic nozzle device for ultrafine fiber solution blow spinning with precise diameter control[2]

Eddie Hofmann,[a,b] Kilian Krüger,[a,b] Christian Haynl,[c] Thomas Scheibel,[c] Martin Trebbin,[d] Stephan Förster[a,b]

[a] Department of Physical Chemistry I, University of Bayreuth, 95440 Bayreuth, Germany.
[b] Jülich Centre for Neutron Science (JCNS-1/ICS-1), Forschungszentrum Jülich GmbH, 52425 Jülich, Germany.
[c] Department for Biomaterials, University of Bayreuth, 95440 Bayreuth, Germany.
[d] Centre for Ultrafast Imaging (CUI), University of Hamburg, 22761 Hamburg, Germany.
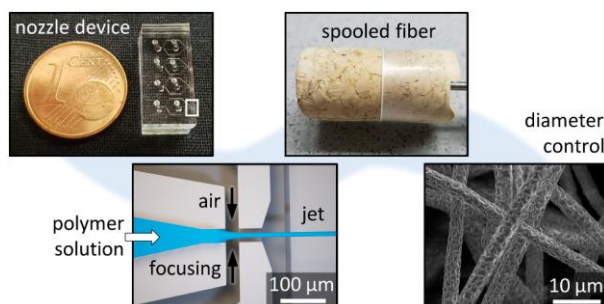
We present a microfluidic nozzle device for the controlled continuous solution blow spinning of ultrafine fibers.

5.1 Abstract

We present a microfluidic nozzle device for the controlled continuous solution blow spinning of ultrafine fibers. The device is fabricated by soft lithography techniques and is based on the principle of a gas dynamic virtual nozzle for precise three-dimensional gas focusing of the spinning solution. Uniform fibers with virtually endless length can be produced in a continuous process while having accurate control over the fiber diameter. The nozzle device is used to produce ultrafine fibers of perfluorinated copolymers and of polycaprolactone which are collected and drawn on a rotating cylinder. Hydrodynamics and mass balance quantitatively predict the fiber diameter which is only a function of flow rate and air pressure, with a small correction accounting for viscous dissipation during jet formation which slightly reduces the jet velocity. Because of the simplicity of the setup, the precise control of the fiber diameter, the positional stability of the exiting ultrafine fiber and the potential to implement arrays of parallel channels for high throughput, this methodology offers significant benefits compared to existing solution-based fiber production methods.

5.2 Introduction

Solution blow spinning is a technique that is used to produce micro- and nanofibers.[1,2] Especially ultrafine fibers and nanofibers have widely gained interest because of their unique mechanical properties and high surface to volume ratio, with applications in protective clothing,[3] air filtration,[4] the controlled release of drugs,[5] as wound dressings for skin regeneration,[6] and for tissue engineering.[7–9] Solution blow spinning combines concepts from melt blowing, solution spinning and electrospinning. It makes use of a concentric nozzle with two coaxial channels to inject a polymer solution through the inner channel into a high velocity gas flow from the surrounding outer channel.[1] Pressurized air confines the polymer solution to generate a fine liquid jet. During jetting, the solvent evaporates and a solid polymer fiber forms which can be collected on a target.[1]

As the main parameters, which influence the spinning process, are very similar for solution blow spinning and electrospinning, the micro- and nanofibers produced by these two techniques are equivalent in size and morphology.[1] Electrospinning uses electrostatic forces, while solution blow spinning uses pressurized gas to generate a liquid jet.[10] Surface tension is the main driving force for jet instability and breakup. It reduces the surface area per unit mass by transforming the jet into spherical droplets with a smaller overall surface area.[11] Conversely, viscosity resists rapid changes in shape, so that an increasing viscosity slows down the deformation and breakup of the polymer jet and thus favors formation of continuous fibers.[11] The viscosity of polymer solutions is strongly influenced by both concentration and molecular weight which affect the number of chain entanglements.[12] The

entanglement number eventually determines whether a spray, a spindle-knotted fiber or a uniform fiber is obtained.[12] Further, a solvent with high vapor pressure is necessary as during fast solvent evaporation there is less time for flow instabilities to develop that deform the jet while spinning. For electrospinning specific additional parameters are the electric voltage and the net charge density, whereas for solution blow spinning flow rate and air pressure define fiber diameter and morphology.[1,13,14]

Solution blow spinning is an inexpensive technique that can be realized in a simple and compact setup. Compared to electrospinning, a higher rate of fiber production is possible, and there are fewer restrictions on the electrical properties of the polymer solution such as conductivity and dielectric constant.[1,15,16] Scaling-up by the use of multiple nozzles is possible, and the method has already demonstrated unique possibilities as for the fabrication of non-woven meshes that can be directly formed on tissue cultures or living tissue,[15] or for the coating of the internal side of tubular vascular prosthesis.[17]

Electrospinning has gained wide attention due to its versatility in spinning a large variety of polymeric fibers,[18] such that the influence of solution properties, electric potential and spinning parameters have already been well investigated.[13,14,19–24] Since solution blow spinning is a much younger technique, there are much fewer studies dealing with the prediction and control of fiber diameter and morphology.[1,25–27] Oliveira *et. al.* showed a strong influence of flow rate, air pressure, concentration and viscosity,[1] whereas Wojasiński *et al.* did not observe any influence of processing parameters other than solution concentration in their study.[26] Sinha-Ray *et al.* developed a complex theoretical model of the solution blowing process showing that reasonable agreement with the experimental data could be observed for the predicted fiber-size distribution.[28] Thus, there still is a considerable lack of knowledge to predict and control the fiber diameter in solution blow spinning, and experimental results are partially contradicting.[1,15,26–30]

Microfluidic technology has not yet been used for solution blow spinning. The key element of the spinning process is the nozzle, for which microfluidic technology offers the possibility to use design principles based on the gas dynamic virtual nozzle-principle (GDVN) which would for the first time allow a precise control of the jet and thus the fiber diameter. The physics of the GDVN-principle to generate capillary jets was developed by Gañán-Calvo *et al.* This study used a simple plate-orifice geometry to create liquid jets and formulated a predictive model for the jet diameter.[31,32] In the model, the pressure difference imposed in axial direction, transmitted to the liquid stream by normal surface stress, is converted into kinetic energy to accelerate the fluid. With the assumption that viscous and capillary forces are sufficiently small compared to the liquid inertia, the jet diameter can be calculated in very good approximation.[33] The nozzle shape determines the boundaries of

the stability and can be used to decrease jet diameters.[10] While Gañán-Calvo *et al.* started their investigations with the plate-orifice geometry,[31,33,34] later on, the converging-diverging nozzle made of glass capillaries was examined,[10,35] and Trebbin *et al.* developed a microfluidic nozzle device for generating liquid jets.[36]

Here we demonstrate that microfluidic nozzle devices based on the GDVN principle can be used for continuous solution blow spinning with excellent prediction and control of the fiber diameter. The microfluidic device was made of poly(dimethylsiloxane) (PDMS), which enabled a fast and easy reproduction by replica molding. In an alteration of Trebbin *et al.*'s nozzle design,[36] the air flow focuses the polymer solution from an orthogonal direction. We demonstrate continuous stable spinning conditions at rates of 5–10 m/s for perfluorocopolymer and polycaprolactone solutions to produce ultrafine fibers with endless length and narrow size distribution. Thus, for the first time the fiber diameter can be precisely controlled by air pressure and solution flow rate in very good agreement with theoretical predictions, which now enables a rational, controlled and reproducible fabrication of endless fibers of the desired diameter by solution blow spinning.

5.3   Results and discussion

5.3.1   Fabrication and design of the nozzle device

The microfluidic nozzle devices for fiber spinning were fabricated by using established photolithography and soft lithography techniques.[37–40] In the first step of this sequence, a micro-structured master was created which acted as a molding template for poly(dimethylsiloxane) PDMS subsequently. Multiple microfluidic chips could be produced from one single PDMS cast, which was divided into individual parts. After cutting, punching inlet ports and thorough cleaning with propan-2-ol, two matching parts were treated with air plasma, aligned accurately and permanently bonded. A schematic overview of the fabrication process is shown in Fig. 1. The final microfluidic chip contained a nozzle array with four separate nozzles side by side. Each nozzle had two inlet ports. One was connected to pressurized air, whereas the other was connected to a syringe pump containing the polymer solution.
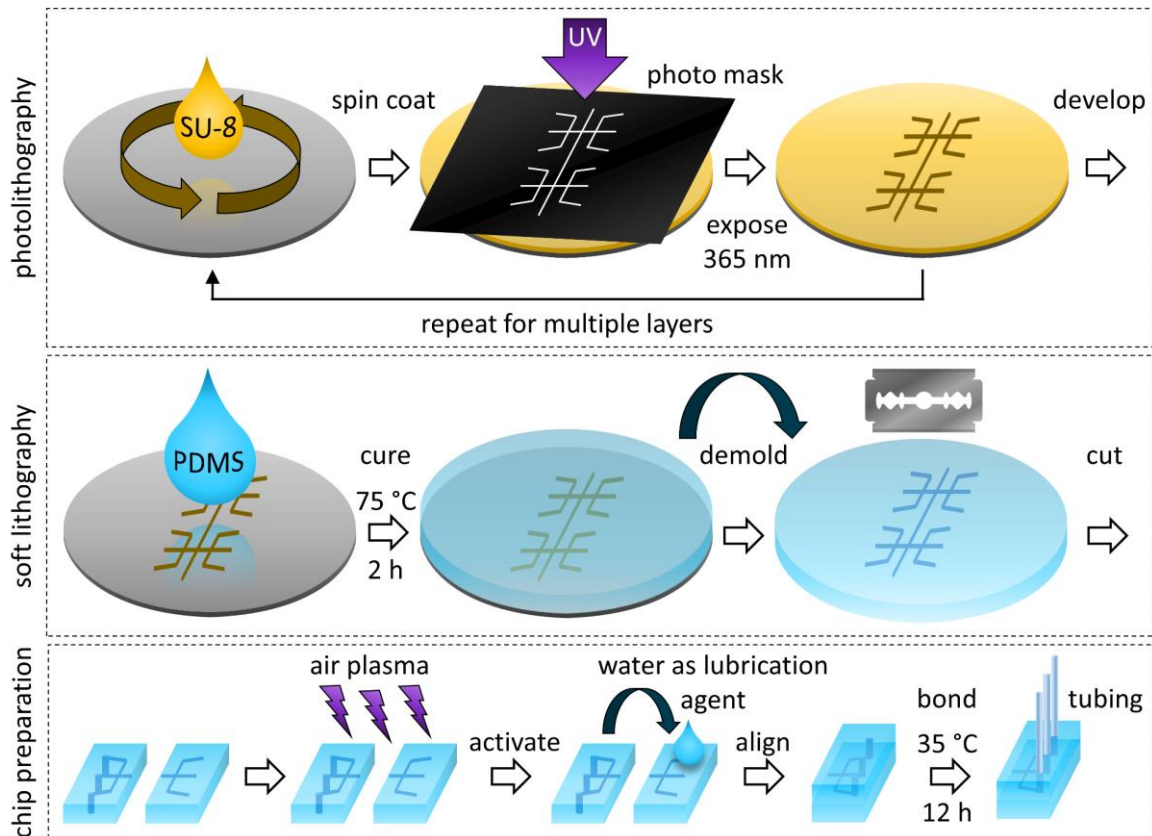
Figure 1: Microfluidic nozzle devices for solution blow spinning are fabricated by using standard photolithography and soft lithography techniques. At first, a structured master is produced, which acts as a casting template for polydimethylsiloxane (PDMS). After curing, a microfluidic device is prepared by bonding two precisely tailored PDMS halves. Water is used as a lubrication agent to facilitate the precise alignment.

As shown previously,[36] the GDVN-principle can be well used to focus a polymer solution into a liquid jet and encase it with a high-velocity air flow. In contrast to solution blow spinning with a concentric nozzle,[15] the inner nozzle, delivering the polymer solution, is not protruding with respect to the outlet of the compressed air. Within the microfluidic nozzle, the air stream is approaching perpendicularly from the sides. To ensure a complete three-dimensional focusing from every direction, also from above and below, the nozzle design is composed of multiple stacked layers to mimic a concentric nozzle. Therefore, two individually structured PDMS halves need to be combined into one microfluidic nozzle device. A precise alignment of these two parts is crucial for accurate nozzle geometry, but can easily be accomplished by integrated orientation structures, which hold both halves in place. The multi-layer architecture of the microfluidic nozzle device is shown in Fig. 2, where all relevant design parameters, listed in Table 1, are also depicted.

The nozzle design can easily be adapted, since master fabrication is a rapid prototyping process. In combination with PDMS, replica molding has a high reproducibility because the same master can be used repeatedly. As all nozzles are almost identical and also fast and simple to produce using soft lithography, the microfluidic chips are disposable consumables. The use of PDMS as chip material has benefits like transparency in UV-

visible regions, compatibility with aqueous and polar solvents and chemical inertness.[41] However, if polar solvents are used, the PDMS needs a surface modification or coating.[42]
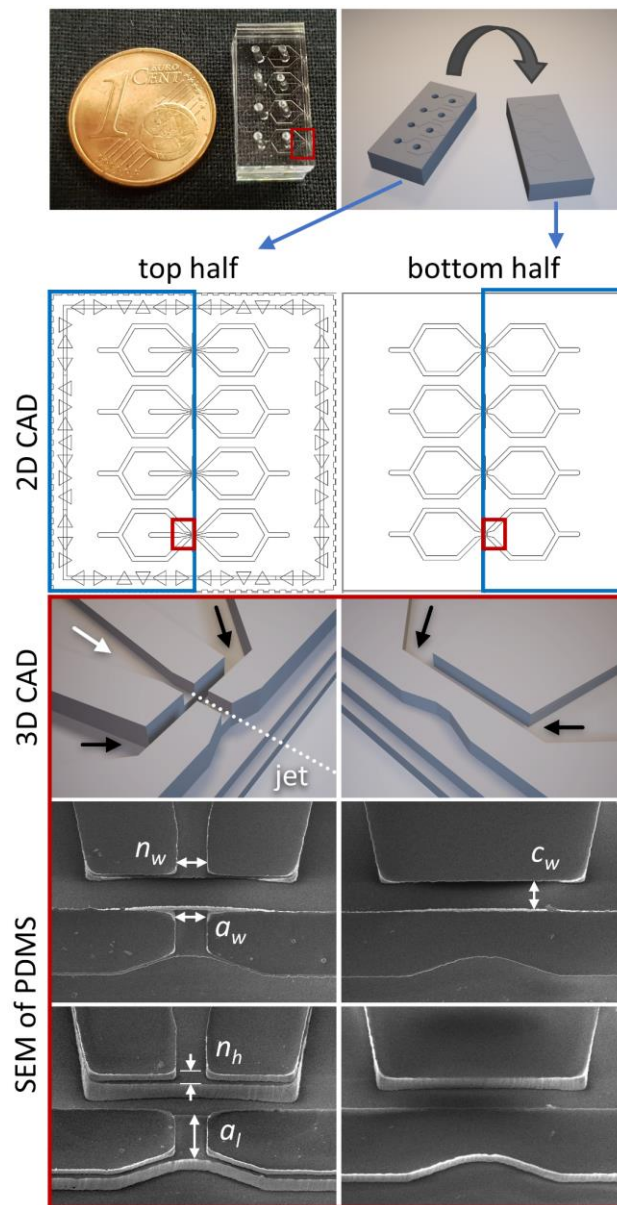

Figure 2: The microfluidic device contains an array of four identical nozzles. Each nozzle is constructed with multiple layers on two individually structured halves, which need to be aligned precisely. Only this multi-layer architecture enables a complete three-dimensional focusing of the spinning solution by a surrounding air flow. Black arrows indicate the inlets of the pressurized air and a white arrow denotes the inlet of the polymer solution. Relevant design parameters are indicated in the SEM images of the nozzle (also see Table 1).

Table 1: List of relevant design parameters for the nozzle layout along with the target size in CAD software and the actually measured size in SEM.

parameter	target size	measured size (SEM)
nozzle width n_w	30 µm	32 µm
nozzle height n_h	30 µm	28 µm
air channel width c_w	30 µm	34 µm
aperture width a_w	30 µm	31 µm
aperture length a_l	50 µm	45 µm

5.3.2   Spinning process and sample collection

In order to quantitatively investigate the conditions for continuous solution blow spinning, a reliable and steady jetting of the polymer solution was necessary. For this study, a special grade perfluorocopolymer (THV 221 from 3M Dyneon, abbreviated as THV) was used, which is soluble in acetone because of the relatively high amount of vinylidene fluoride.[43,44] Due to its fluorinated components, THV has great non-sticking properties to PDMS, which leads to a very stable spinning process. Acetone is well-suited as a solvent because of the high vapor pressure (240 hPa at 20 °C).[45] This results in a high evaporation rate of the solvent from the jetted polymer solution preventing jet instabilities to develop, which would lead to non-uniform fibers or alternatively to spraying or to discontinuous fibers. For comparison, a poly(caprolactone) (PCL) solution was spun using the microfluidic device in a similar manner but with hexafluoroisopropanol (HFIP) as a solvent.

High-precision syringe pumps were used to ensure a constant flow rate Q of the spinning solution. The pressure difference Δp between the compressed air and atmospheric pressure was adjusted by a pressure controller with a manometer. Employing suitable values for these parameters, uniform fibers could be produced by jetting the polymer solution out of the nozzle device in a steady process. While jetting through the air for a certain distance, the solvent evaporates, the fiber solidifies and could be collected on a cork spool. Both the working distance d_s between the nozzle and the spool and the rotational speed of the spool were adjustable. By changing the rotational speed, different drawing speeds v_s could be applied during the spinning process. Fig. 3 shows the spinning process (3A) and the setup for sample collection (3B). The jetted fiber exits in a very narrow cone of only a few degrees and can be collected on a spool, where it forms a strand of parallel fibers forming a torus (Fig. 3C). All fiber samples were investigated by scanning electron microscopy (SEM) to determine the quadratic mean (root mean square, RMS) and the standard deviation (SD) of the fiber diameter by evaluating multiple images statistically (see ESI[†]).
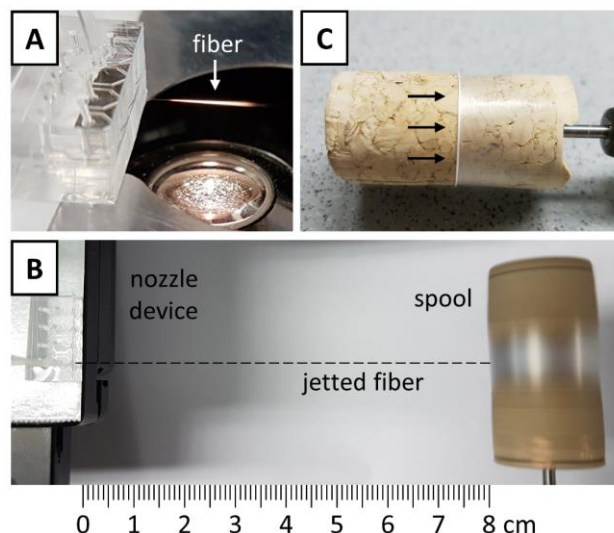
Figure 3: Photos illustrating the process of spinning and collection of the fiber samples. The polymer solution is jetted out of the microfluidic device (A). While the jet travels through the air, the solvent is evaporating and a solid fiber is forming, which is collected on a rotating cork spool (B). Afterwards, the fibers are bundled into a strand by carefully pushing them together (C).

Under stable spinning conditions, continuous fibers of ~2.3 km length (5 min) and of narrow size distribution could be produced. The histogram in Fig. 4D confirms the narrow size distribution. The evaluation of 368 single fibers resulted in a mean diameter of 2.1 ± 0.3 µm for the following processing parameters: $Q = 1.0$ mL/h, $\Delta p = 2.0$ bar, $v_s = 7.7$ m/s, $d_s = 8$ cm, 20% (w/w) THV in acetone.

This successful application of a microfluidic nozzle design for the continuous production of fibers could, in principle, be extended to bio-based nanofibrils which have recently been demonstrated to be a promising material in fiber spinning technology.[46] This would only require a flow-focusing section prior to the gas virtual nozzle section, which has been recently demonstrated.[36]

5.3.3   Surface structure of fibers

The SEM images also reveal the morphology and surface structure of the THV fibers for all different sets of parameters. In Fig. 4A, the fiber sample is collected as a non-woven mesh on a plate, and in Fig. 4C as a strand of fibers on a spool. As shown in Fig. 4B, the fiber surface texture exhibits small cavities with almost circular shape which emerge during solvent evaporation through the outer shell of the fiber, similarly as for electrospun fibers. Fibers with smooth surfaces are obtained when using solvents with lower vapor pressure.
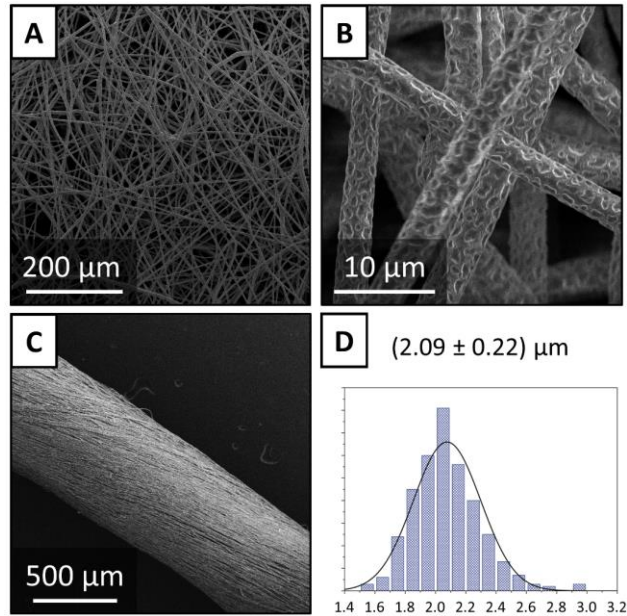
Figure 4: SEM images of a non-woven mesh collected on a plate (A) and close-up image of the surface structure of the fiber (B) for 2.0 mL/h, 2.0 bar, 8 cm, 20% (w/w) THV in acetone, 3.7 ± 0.7 µm; strand of fibers after collection on a spool (C) and histogram showing the distribution of fiber diameters (D) for 1.0 mL/h, 2.0 bar, 7.7 m/s, 8 cm, 20% (w/w) THV in acetone, 2.1 ± 0.2 µm.
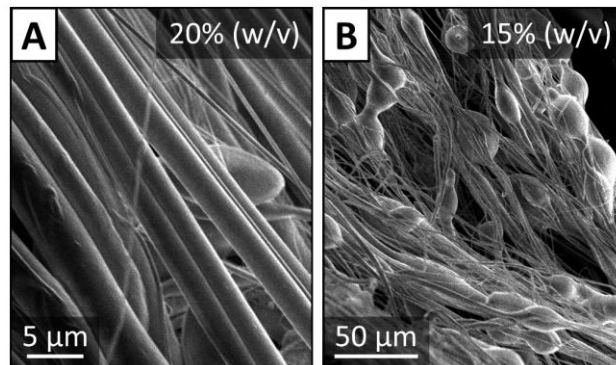

Figure 5: Different morphologies of polycaprolactone fibers that can be achieved: SEM image of (A) smooth fiber (0.5 mL/h, 2.5 bar, 5.5 m/s, 10 cm, 20% (w/v) PCL in HFIP, 2.3 ± 1.1 µm) and (B) spindle-knotted fiber (1.0 mL/h, 2.0 bar, 10.3 m/s, 10 cm, 15% (w/v) PCL in HFIP).

Fig. 5A shows an example of a fiber with smooth surface structure, which was spun from a 20% (w/v) solution of poly(caprolactone) (PCL) in hexafluoroisopropanol (HFIP). Using a 15% (w/v) solution of PCL in addition to the slower evaporation rate caused by the lower vapor pressure of HFIP of 160 hPa (20 °C)[47] leads to a varying fiber diameter showing spindle-knotted fiber morphology (Fig 5B) since there is more time for jet instabilities to develop. In general, as for electrospun fibers, spindle-knotted fibers could be useful for water collection in technical processes.[48–50] As a remedial measure, the overall evaporation time can be reduced by generating smaller jets which reduces the diffusion

distance or by increasing the temperature. When the drawing speed was increased, the cavities on the THV fibers became more elongated, confirming that the fiber is stretched during jetting while forming between nozzle and spool.

5.3.4   Control of fiber diameter

A major aim of our investigation was to quantify the influence of the main spinning parameters on the fiber diameter to develop a fundamental understanding of the spinning process, and to establish a precise prediction of the fiber diameter. Therefore, an equation for calculating the fiber diameter d_f was derived, based on the conservation of volume of the THV polymer in the spinning solution and the final fiber.

The fiber diameter is only depending on the flow rate Q, the fiber velocity v_f and the volume fraction of THV ϕ_T in the polymer solution. A detailed derivation of eq. (1) can be found in the ESI[†].

$$d_f = \sqrt{\frac{4 \cdot \phi_T \cdot Q}{\pi \cdot v_f}} \tag{1}$$

For a given polymer solution with a certain concentration, the fiber diameter is only proportional to $Q^{1/2}$ and $v_f^{-1/2}$. The velocity of the fiber v_f is supposed to be equal to the velocity of the jet v_j, which is determined by the pressure drop Δp of the compressed air. Alternatively, if the drawing speed v_s applied to the fiber by the rotating spool is even faster, the final diameter is determined by the drawing speed while collecting the fiber.

$$v_f = \begin{cases} v_j & , \text{if } v_j \geq v_s \\ v_s & , \text{if } v_j < v_s \end{cases} \tag{2}$$

A connection between the jet velocity v_j and the pressure difference Δp can be established by Bernoulli's equation for incompressible flows by comparing the two states inside the nozzle and inside the liquid jet.

$$v_j = \sqrt{\frac{2 \cdot \Delta p}{\rho_0}} \tag{3}$$

Eq. (3) shows, that the velocity increases in proportion to $\Delta p^{1/2}$. If we assume that the acceleration of the jet and the evaporation of the solvent happen successively, the mass density ρ_0 of the polymer solution stays constant while the jet is accelerated. We note that in this consideration, the loss of kinetic energy due to viscous dissipation and shear stress is neglected.[31] As a result, eq. (4) connects the fiber diameter to the pressure difference, showing a proportionality of $\Delta p^{-1/4}$.

$$d_f = \left(\frac{8 \cdot \rho_0 \cdot {\phi_T}^2 \cdot Q^2}{\pi^2 \cdot \Delta p} \right)^{1/4} \qquad (4)$$

Gañán-Calvo postulated an equation for the diameter of a jet d_j in the plate-orifice geometry using the GDVN-principle.[31] Trebbin *et al.* showed that this model can also be applied to microfluidic nozzle devices.[36]

$$d_j = \left(\frac{8 \cdot \rho_0}{\pi^2 \cdot \Delta p} \right)^{1/4} \cdot Q^{1/2} \qquad (5)$$

The comparison between eq. (4) and eq. (5) illustrates that the fiber diameter differs just by the term $\sqrt{\phi_T}$ from the Gañán-Calvo[31] equation for the jet diameter. The factor $\sqrt{\phi_T}$ takes account of the evaporation of the solvent causing the shrinkage in diameter:

$$d_f = \sqrt{\phi_T} \cdot d_j \qquad (6)$$

The main spinning parameters were varied systematically to verify the proportionalities of flow rate, pressure difference and drawing speed. Therefore, different combinations for a 20% (w/w) solution of THV 221 in acetone were tested with flow rates between 1.0 mL/h and 4.0 mL/h and the drawing speed ranging from 5.5 m/s to 15.5 m/s at a constant pressure difference of 2.0 bar and a working distance of 8 cm. Additionally, the flow rate and the air pressure were varied between 1.0 mL/h and 3.0 mL/h, respectively between 1 bar and 2.5 bar at a constant drawing speed of 7.7 m/s and a working distance of 8 cm. The fiber diameter was ranging from 1.6 µm to 4.2 µm, as shown in Fig. 6.
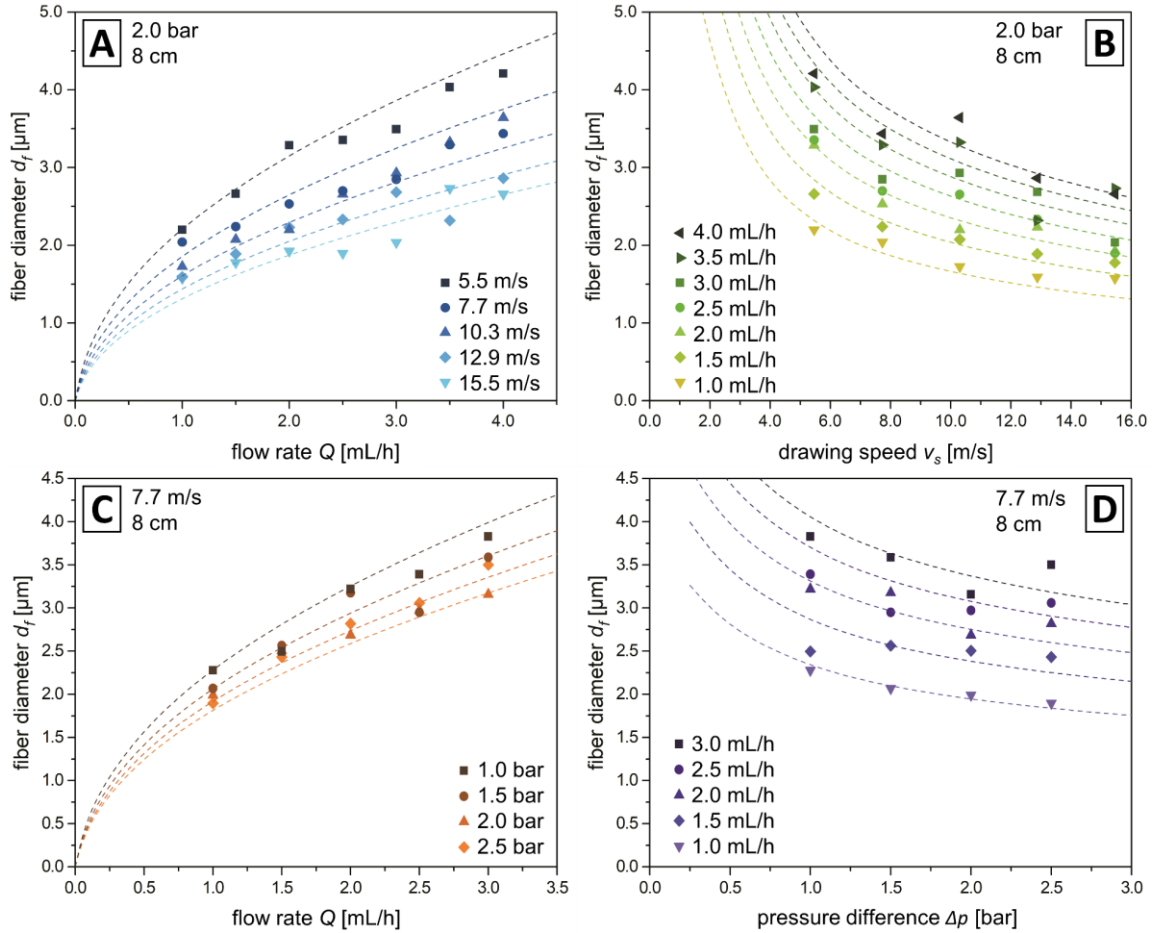
Figure 6: Graphs showing the mean diameter of the THV fiber samples as a function of the investigated process parameters (flow rate (A,C), drawing speed (B) and pressure difference (D)). Dashed lines indicate the predicted fiber diameters according to eq. (7) and eq. (8).

When performing a linear regression with the logarithmic values of the fiber diameter and the varied process parameter, the slope should be equivalent to the exponent of the corresponding parameter. The values for the linear regression are summarized in Table 2. The experimentally determined exponents coincided very well with the postulated power laws in eq. (1) and eq. (4). This confirms that the assumed correlations are correct.

We noted above that the loss of kinetic energy due to viscous dissipation and surface tension were neglected in the derivation of eqs. (1) and (4). In this light we introduced a factor f_{BC} for the fiber diameter derived in eq. (1), and a factor f_{AD} in eq. (4) to account for systematic deviations between calculated and measured fiber diameters.

$$d_f = f_{BC} \cdot \sqrt{\frac{4 \cdot \phi_T \cdot Q}{\pi \cdot v_f}} \qquad (7)$$

$$d_f = f_{AD} \cdot \left(\frac{8 \cdot \rho_0 \cdot \phi_T{}^2 \cdot Q^2}{\pi^2 \cdot \Delta p}\right)^{1/4} \qquad (8)$$

The values of the parameters were determined by linear regression with the slopes fixed to the theoretical values. As shown in Table 2 we thus obtained values of $f_{BC} = 0.91 \pm 0.04$ and $f_{AD} = 1.55 \pm 0.08$. The correction factor f_{BC} for $d_f(Q, v_f)$ is close to 1, confirming the excellent applicability of eq. (1), which is based on the conservation of volume.

Table 2: Results for the linear regressions of the fiber diameter support the power laws for the correlation with the tested processing parameters.

	first linear regression		second linear regression	
equation	expected slope	calculated slope	correction term	correction factor
$\log d_f = \log C + c \cdot \log Q$	$c = +0.5$	0.43 ± 0.07	$\log f_{BC} = -0.041 \pm 0.019$	$f_{BC} = 0.91 \pm 0.04$
$\log d_f = \log B - b \cdot \log v$	$b = -0.5$	-0.42 ± 0.05		
$\log d_f = \log D + d \cdot \log Q$	$d = +0.5$	0.48 ± 0.05	$\log f_{AD} = 0.192 \pm 0.022$	$f_{AD} = 1.55 \pm 0.08$
$\log d_f = \log A - a \cdot \log \Delta p$	$a = -0.25$	-0.13 ± 0.07		

The graphs in Fig. 6 show a very good agreement between the measured fiber diameters and the calculated values from eqs. (7) and (8). The determined exponent of Δp deviates moderately from the theoretical one of -0.25. We note that the drawing speed v_s can only be used for the fiber velocity v_f, if it is faster than the velocity of the jet exiting v_j the nozzle. In this experiment, this is valid for all tested drawing speeds except the slowest one with 5.5 m/s. The jet velocity at the pressure difference of 2.0 bar is 6.1 m/s as shown with a high-speed camera (see Fig. 8).

In contrast, when calculating the fiber diameter $d_f(Q, \Delta p)$ with eq. (4), based on pressure difference and flow rate, the fiber diameter is around 1.55-times larger than the expected one. A larger fiber diameter is an indication for a slower jet and fiber velocity. As a consequence, the specific internal energy is not completely converted into specific kinetic energy and the jet is less accelerated. The finite energy loss due to viscous dissipation of the polymer solution is determined in the subsequent section.

5.3.5   Measurement of jet diameter

If there is an incomplete conversion of specific internal energy to specific kinetic energy, the measured jet diameters should be systematically larger than the calculated ones. Therefore, the jet diameter was investigated by optical microscopy and the results are reported in Fig. 7. The same trend as for the fiber diameter could be observed, which is shown by the graph in Fig. 7.

$$d_j = f_J \cdot \left(\frac{8 \cdot \rho_0 \cdot Q^2}{\pi^2 \cdot \Delta p} \right)^{1/4} \tag{9}$$

As expected, a correction factor f_J in eq. (9) was necessary to scale the jet diameter in eq. (5) appropriately. The correction factor $f_J = 1.79 \pm 0.10$ is close to the corresponding one f_{AD} for the fiber diameter.
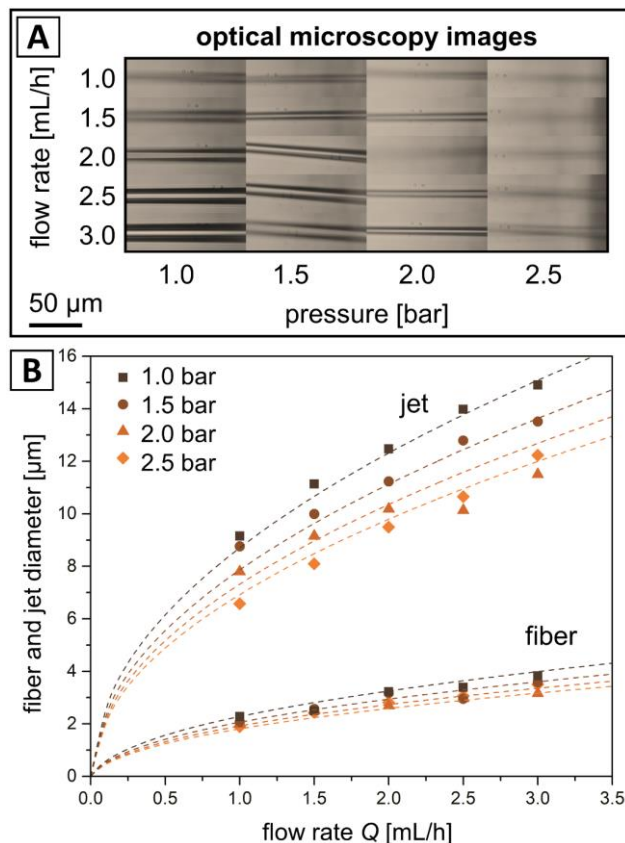

Figure 7: Jet diameter of a 20 % (w/w) THV solution measured directly after passing the nozzle at varied flow rates and pressure differences. The diameters of the jet and the fiber exhibit the same correlation, since both differ just in the factor $\sqrt{\phi_T}$ due to evaporation of the solvent. Images of the jet from optical microscopy (A); graph showing measured values (B) and predictions according to eq. (8) and eq. (9) as dashed lines.

5.3.6   Measurement of fiber velocity

Using a high-speed camera, the velocity of the polymer solution inside the nozzle v_n and the velocity of the polymer jet v_j could be measured directly. Therefore, an aqueous dispersion of polystyrene particles was pumped through the microfluidic device to determine v_n by measuring the travel distance of multiple particles between two images at a frame rate of 37004 fps. The determined velocity of 0.273 m/s is equal to the velocity of 0.268 m/s, which can be calculated by dividing the flow rate (1.0 mL/h) by the cross section of the nozzle (1037 µm²). The measurement of the jet velocity v_j was performed with the THV solution, complying exactly with the spinning conditions for sample collection. Infrequently occurring beads in the jet were used to calculate the jet velocity of 6.13 m/s

(see Fig. 8B). This measured velocity is also equal to the expected velocity for a jet with a diameter of 7.6 µm at 1 mL/h. In conclusion, it could be shown by using a high-speed camera that the jet velocity can be calculated by dividing the flow rate by the cross-sectional area. This confirms that the jet velocity is slower than expected in eq. (3).
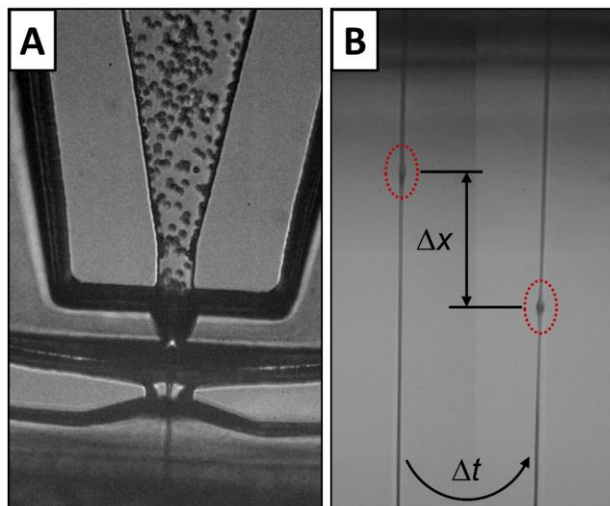

Figure 8: The velocity of the stream (1 mL/h, 2 bar) was measured inside the nozzle by tracking of polymer particles (A) or inside the jet by following occasional beads (B) with a high-speed camera (frame rate: 37004 fps (A); 31019 fps (B)).

5.3.7   Influence of other working parameters

As shown above the fiber diameter is completely determined by the flow rate Q and the pressure difference Δp, with a slight correction to account for viscous dissipation which reduces the velocity v_j of the jet exiting the nozzle. We additionally examined the influence of the distance d_s between the nozzle and the spool, which showed that the spool needs be positioned beyond a certain distance from the nozzle to allow for sufficient solvent evaporation to obtain fully developed fibers. Furthermore, we studied the influence of polymer concentration. In order to generate continuous fibers, the concentration needs to be in a range where it is sufficiently large to obtain continuous fibers, but still being low enough to have a viscosity where the solution can be pumped through the central channel. Finally, also conditions for narrow fiber diameter distributions were determined. Details of these additional studies are given in the ESI†.

5.4   Conclusion

In conclusion, we present a microfluidic nozzle device for solution blow spinning of ultrafine fibers offering significant benefits compared to existing approaches. Using the gas dynamic virtual nozzle-principle, uniform fibers with virtually endless length can be

produced in a steady process while having precise control over fiber diameter and morphology. The fiber diameter can be quantitatively predicted and depends only the flow rate and air pressure, with a small correction accounting for viscous dissipation which reduces the jet velocity. Thus, for the first time the fiber diameter can be precisely controlled by air pressure and solution flow rate in very good agreement with theoretical predictions, which now enables a rational, controlled and reproducible fabrication of endless fibers of the desired diameter by solution blow spinning. Because of the simplicity of the setup, the positional stability of the exiting ultrafine fiber and the potential to implement arrays of parallel channels for high throughput this methodology is a versatile alternative to established solution-based fiber production methods.

5.5 Materials and methods

5.5.1 Photolithographic master fabrication

By using photolithography, a microstructured master was produced and afterwards cast with polydimethylsiloxane (PDMS). The whole procedure of fabricating microfluidic devices with multi-layered channel structures is shown in Fig. 1. At first, the desired microfluidic nozzle structures were designed with AutoCAD (Autodesk Inc.) and printed on a high-resolution film photomask by JD Photo Data. The following steps were performed in a clean room. A 3" silicon wafer was spin-coated (Cee 200X, Brewer Science Inc.) with a negative photoresist (SU-8 25 and SU-8 50, MicroChem Corp.). The structures on the photomask were transferred to the photoresist by exposing this thin layer of SU-8 through the photomask and hereby cross-linking the photoresist at the exposed areas. For this purpose, a contact mask aligner MJB4 (SÜSS MicroTec SE) with UV light of 365 nm was used. The previous steps of spin-coating and exposure were repeated to build up two additional layers. Precise alignment of photomask and substrate was necessary. In the subsequent development step, the uncured photoresist was removed with 1-methoxy-2-propanyl acetate (mr-Dev 600, micro resist technology GmbH). The resulting lithography master featured the channel design as inverted microstructure. The values of all geometric design parameters, which are shown in Fig. 2, are listed in Table 1.

5.5.2 PDMS device fabrication

The following steps of soft lithography and finalization of the microfluidic device were performed in a dust-free environment. For replication of the micro-structured master, a 10 : 1 mixture (monomer : curing agent) of PDMS (Sylgard 184 kit, Dow Corning Corp.) was poured onto the microstructured master, degassed and cured for 2 h at 75 °C. After demolding, the PDMS replica was cut with a razor blade along predefined grooves into

individual parts. For later connection of the tubing, inlet ports were punched into the PDMS with an Integra® Miltex® biopsy punch with plunger (1 mm, Integra LifeSciences Corp.). Two individual structured halves had to be combined, to create a 3D nozzle device. Therefore, the surfaces of two matching halves of PDMS were activated using air plasma (MiniFlecto®, plasma technology GmbH). In addition, a small drop of ultrapure water (Milli-Q, Merck KGaA) was added to generate a thin film of water, which enabled the alignment of the two individual parts prior to the final bonding. Bringing both parts in close contact allowed the integrated orientation structures to snap in and align the microstructures automatically. If necessary, fine adjustments were performed under a microscope. Removing the water in an oven at 35 °C for 12 h resulted in a permanent bonding of the microfluidic device.

5.5.3   Spinning solution

Microfluidic solution blow spinning requires a polymer solution with a volatile solvent. For most experiments, a 20% (w/w) polymer solution of 3M™ Dyneon™ THV 221GZ (3M Deutschland GmbH) in acetone was used. THV is a flexible and transparent fluoroplastic composed of tetrafluoroethylene, hexafluoropropylene and vinylidene fluoride. Acetone has a high vapor pressure of 240 hPa (20 °C),[44,45] which results in a fast evaporation rate of the solvent from the jetted solution. In addition, a solution of polycaprolactone ($M_w = 45,000$ g mol^{-1}, Sigma Aldrich Chemie GmbH) in hexafluoro-2-propanol, which has a vapor pressure of 160 hPa (20 °C),[47] was tested.

5.5.4   Microfluidic solution blow spinning and sample collection

The microfluidic nozzle device was connected via LDPE tubing (0.38 mm I.D., 1.09 mm O.D., Science Commodities Inc.) to a syringe pump (neMESYS 290N, Cetoni GmbH) and pressurized air. The spinning solution was filled into glass syringes (1.0 mL, Gastight 1000 Series, Hamilton Company) for precise pumping at flow rates between 0.5 mL/h and 4.0 mL/h and at constant air pressures between 0.5 bar and 2.5 bar. For the start-up procedure, the pressurized air was connected first and set to the desired value. Subsequently, the flow of the spinning solution was started, and the tubing plugged into the nozzle device to start the spinning process. The fiber spinning was conducted at ambient conditions of 23 °C room temperature and a relative humidity in the range of 45-55%. The spinning process was examined with an inverted optical microscope (IX71 and IX73, Olympus Corp.) and in combination with a DSLR camera (D7000, Nikon) high resolution images of the jetted spinning solution were taken.

Fiber samples were collected by means of a cork cylinder on a rotary tool (Proxxon GmbH), which was mounted in an adjustable distance to the nozzle device. The rotational speed was monitored with an optical revolution counter (UT372, UNI-T) and could be changed

steplessly. Thus, it was possible to apply different drawing speeds to the fiber while collecting the sample. The drawing speed could be calculated from the rotational speed by using the perimeter of the cork cylinder (61.8 mm). The benefit of using a cork spool was that the fibers didn't adhere to it. After a predefined collection time, the spooled fiber was carefully pushed together to form a strand of fibers.

From each fiber sample, several representative images were taken with a scanning electron microscope (JSM-6510LV, JEOL GmbH) and statistically analyzed with ImageJ software (National Institutes of Health) to determine the quadratic mean of the fiber diameter (root mean square) and the standard deviation.

5.5.5   Velocity measurement with high-speed cinematography

The liquid jet of spinning dope exited the nozzle at a very high velocity in relation to its small scale. This fast process could only be observed by a high-speed camera (Phantom v1610, Vision Research Inc.). A highly intense, focused light source (halolux LED-30, STREPPEL Glasfaser-Optik GmbH & Co. KG) was used to get sufficient light for short exposure times down to 2 µs. In combination with a long-distance microscope (Model K1 CentriMax™, Infinity Photo-Optical Company) and a UPlanFL N 10x/0.30 objective (Olympus Corporation) the setup allows to measure the velocity of the solution inside the nozzle and the velocity of the jet directly after the nozzle outlet. The flow inside the nozzle was tracked using monodisperse polystyrene particles in aqueous dispersion (4.89 µm, SD = 0.08 µm, microParticles GmbH).

Conflicts of interest

There are no conflicts to declare.

Acknowledgements

5.6 References

1   J. E. Oliveira, E. A. Moraes, R. G. F. Costa, A. S. Afonso, L. H. C. Mattoso, W. J. Orts and E. S. Medeiros, *J. Appl. Polym. Sci.*, 2011, **122**, 3396–3405.

2   R. M. d. C. Farias, R. R. Menezes, J. E. Oliveira and E. S. de Medeiros, *Materials Letters*, 2015, **149**, 47–49.

3   Z.-M. Huang, Y.-Z. Zhang, M. Kotaki and S. Ramakrishna, *Composites Science and Technology*, 2003, **63**, 2223–2253.

4   E. Scholten, L. Bromberg, G. C. Rutledge and T. A. Hatton, *ACS applied materials & interfaces*, 2011, **3**, 3902–3909.

5   F. Sharifi, A. C. Sooriyarachchi, H. Altural, R. Montazami, M. N. Rylander and N. Hashemi, *ACS Biomater. Sci. Eng.*, 2016, **2**, 1411–1431.

6   M. Mirjalili and S. Zohoori, *J Nanostruct Chem*, 2016, **6**, 207–213.

7   C. A. Martínez-Pérez, I. Olivas-Armendariz, J. S. Castro-Carmona and P. E. García-Casillas, in *Advances in regenerative medicine*, ed. S. Wislet-Gendebien, Intech, Rijeka, 2011.

8   R. Vasita and D. S. Katti, *International journal of nanomedicine*, 2006, **1**, 15–30.

9   Q. P. Pham, U. Sharma and A. G. Mikos, *Biomacromolecules*, 2006, **7**, 2796–2805.

10 A. J. Acero, C. Ferrera, J. M. Montanero and A. M. Gañán-Calvo, *J. Micromech. Microeng.*, 2012, **22**, 65011.

11 H. Fong, I. Chun and D.H. Reneker, *Polymer*, 1999, **40**, 4585–4592.

12 S. L. Shenoy, W. D. Bates, H. L. Frisch and G. E. Wnek, *Polymer*, 2005, **46**, 3372–3384.

13 A. Haider, S. Haider and I.-K. Kang, *Arabian Journal of Chemistry*, 2015, doi: http://dx.doi.org/10.1016/j.arabjc.2015.11.015.

14 J.M. Deitzel, J. Kleinmeyer, D. Harris and N.C. Beck Tan, *Polymer*, 2001, **42**, 261–272.

15 E. S. Medeiros, G. M. Glenn, A. P. Klamczynski, W. J. Orts and L. H. C. Mattoso, *J. Appl. Polym. Sci.*, 2009, **113**, 2322–2330.

16 W. K. Son, J. H. Youk, T. S. Lee and W. H. Park, *Polymer*, 2004, **45**, 2959–2966.

17 S. François, C. Sarra-Bournet, A. Jaffre, N. Chakfé, B. Durand and G. Laroche, *Journal of biomedical materials research. Part B, Applied biomaterials*, 2010, **93**, 531–543.

18 T. Subbiah, G. S. Bhat, R. W. Tock, S. Parameswaran and S. S. Ramkumar, *J. Appl. Polym. Sci.*, 2005, **96**, 557–569.

19 C. J. Luo, M. Nangrejo and M. Edirisinghe, *Polymer*, 2010, **51**, 1654–1662.

20 A. Baji, Y.-W. Mai, S.-C. Wong, M. Abtahi and P. Chen, *Composites Science and Technology*, 2010, **70**, 703–718.

21   C. Wang, H.-S. Chien, K.-W. Yan, C.-L. Hung, K.-L. Hung, S.-J. Tsai and H.-J. Jhang, *Polymer*, 2009, **50**, 6100–6110.

22   V. Beachley and X. Wen, *Mater Sci Eng C Mater Biol Appl.*, 2009, **29**, 663–668.

23   S. Agarwal, A. Greiner and J. H. Wendorff, *Progress in Polymer Science*, 2013, **38**, 963–991.

24   G. Lang, S. Jokisch and T. Scheibel, *Journal of visualized experiments: JoVE*, 2013, e50492.

25   L. Zhang, P. Kopperstad, M. West, N. Hedin and H. Fong, *J. Appl. Polym. Sci.*, 2009, **114**, 3479–3486.

26   M. Wojasiński, M. Pilarek and T. Ciach, *Polish Journal of Chemical Technology*, 2014, **16**, 2, 43–50.

27   D. D. da Silva Parize, J. E. de Oliveira, M. M. Foschini, J. M. Marconcini and L. H. C. Mattoso, *J. Appl. Polym. Sci.*, 2016, **133**, 43379.

28   S. Sinha-Ray, S. Sinha-Ray, A. L. Yarin and B. Pourdeyhimi, *Polymer*, 2015, **56**, 452–463.

29   D. D. da Silva Parize, M. M. Foschini, J. E. de Oliveira, A. P. Klamczynski, G. M. Glenn, J. M. Marconcini and L. H. C. Mattoso, *J Mater Sci*, 2016, **51**, 4627–4638.

30   J. Oliveira, G. S. Brichi, J. M. Marconcini, L. H. Capparelli Mattoso, G. M. Glenn and E. Souto Medeiros, *Journal of Engineered Fabrics & Fibers (JEFF)*, 2014, **9**, 117–125.

31   A. M. Gañán-Calvo, *Phys. Rev. Lett.*, 1998, **80**, 285–288.

32   A. M. Gañán-Calvo, C. Ferrera and J. M. Montanero, *J. Fluid Mech.*, 2011, **670**, 427–438.

33   M. A. Herrada, A. M. Gañán-Calvo, A. Ojeda-Monge, B. Bluth and P. Riesco-Chueca, *Physical review. E, Statistical, nonlinear, and soft matter physics*, 2008, **78**, 36323.

34   T. Si, F. Li, X.-Y. Yin and X.-Z. Yin, *J. Fluid Mech.*, 2009, **629**, 1.

35   D. P. DePonte, U. Weierstall, K. Schmidt, J. Warner, D. Starodub, J. C. H. Spence and R. B. Doak, *J. Phys. D: Appl. Phys.*, 2008, **41**, 195505.

36   M. Trebbin, K. Krüger, D. DePonte, S. V. Roth, H. N. Chapman and S. Förster, *Lab Chip*, 2014, **14**, 1733.

37   Y. Xia and G. M. Whitesides, *Angewandte Chemie International Edition*, 1998, **37**, 550–575.

38   J. C. McDonald and G. M. Whitesides, *Acc. Chem. Res.*, 2002, **35**, 491–499.

39   J. C. McDonald, D. C. Duffy, J. R. Anderson, D. T. Chiu, H. Wu, O. J. A. Schueller and G. M. Whitesides, *Electrophoresis*, 2000, 27–40.

40   J. R. Anderson, D. T. Chiu, R. J. Jackman, O. Cherniavskaya, J. C. McDonald, H. Wu, S. H. Whitesides and G. M. Whitesides, *Anal. Chem.*, 2000, **72**, 3158–3164.

41   J. N. Lee, C. Park and G. M. Whitesides, *Analytical chemistry*, 2003, **75**, 6544–6554.

42   B.-Y. Kim, L.-Y. Hong, Y.-M. Chung, D.-P. Kim and C.-S. Lee, *Adv. Funct. Mater.*, 2009, **19**, 3796–3803.

43   3M Advanced Materials Division, *Product Data Sheet.* 3M™ Dyneon™ Fluoroplasic Granules THV 221GZ, available at: https://multimedia.3m.com/mws/media/571351O/fluoroplastic-granules-thv-221gz-data-sheet.pdf, accessed 27 October 2017.

44   J. G. Drobny, *Technology of Fluoropolymers, Second Edition*, CRC Press, 2008.

45   Carl Roth GmbH + Co. KG, *Safety data sheet of acetone,* available at: https://www.carlroth.com/downloads/sdb/de/9/SDB_9372_DE_DE.pdf, accessed 17 November 2017.

46   A. Kamada, N. Mittal, L. D. Söderberg, T. Ingverud, W. Ohm, S. V. Roth, F. Lundell and C. Lendel, *PNAS*, 2017, **114**, 1232–1237.

47   Carl Roth GmbH + Co. KG, *Safety data sheet of 1,1,1,3,3,3-hexafluoro-2-propanol,* available at: https://www.carlroth.com/downloads/sdb/de/2/SDB_2473_DE_DE.pdf, accessed 17 November 2017.

48   H. Bai, R. Sun, J. Ju, X. Yao, Y. Zheng and L. Jiang, *Small*, 2011, **7**, 3429–3433.

49   Y. Chen, L. Wang, Y. Xue, L. Jiang and Y. Zheng, *Scientific reports*, 2013, **3**, 2927.

50   X. Tian, Y. Chen, Y. Zheng, H. Bai and L. Jiang, *Advanced materials*, 2011, **23**, 5486–5491.

5.7 Supplementary Information

5.7.1 Analyzing the fiber diameter

When analyzing the fiber samples via scanning electron microscopy, the quadratic mean (RMS) and the standard deviation (SD) were determined. For each parameter set, an adequate number n of single fibers was measured. Since later calculations assume volume constancy, the arithmetic mean of the fiber volume (eq. (S2)) is needed, and the RMS of the fiber radius (eq. (S5)) was used instead of the arithmetic mean. The fiber volume is approximated by the volume of a cylinder:

$$V = r^2 \pi \cdot l \tag{S1}$$

$$\bar{V} = \frac{1}{n} \cdot \sum_{i=1}^{n} V_i \tag{S2}$$

$$\bar{r}^2 \pi \cdot l = \frac{1}{n} \cdot \sum_{i=1}^{n} r_i^2 \pi \cdot l \tag{S3}$$

$$\bar{r}^2 = \frac{1}{n} \cdot \sum_{i=1}^{n} r_i^2 \tag{S4}$$

$$\bar{r} = \sqrt{\frac{1}{n} \cdot \sum_{i=1}^{n} r_i^2} \tag{S5}$$

5.7.2 Deviation of an equation to predict the fiber diameter

The flow rate Q states which volume of polymer solution V_0 is jetted by the nozzle in a predefined time t.

$$Q = \frac{V_0}{t} \tag{S6}$$

The created fiber volume V_f equals the volume V_T of THV in the jet, given by the volume fraction ϕ_T.

$$\frac{V_f}{t} = Q \cdot \frac{V_T}{V_0} = Q \cdot \phi_T \tag{S7}$$

As the cross section of the fiber is almost circular, the fiber volume is approximated by the volume of a cylinder. Length l_f per time t determines the velocity v_f of the fiber respectively of the jet, since we assume that the speed is constant, when the solvent evaporates and only the diameter reduces.

$$\frac{V_f}{t} = \frac{\left(\frac{d_f}{2}\right)^2 \pi \cdot l_f}{t} = \left(\frac{d_f}{2}\right)^2 \pi \cdot v_f \tag{S8}$$

Combining eq. (S7) and eq. (S8), we achieve an expression to calculate the fiber diameter d_f.

$$\left(\frac{d_f}{2}\right)^2 \pi \cdot v_f = Q \cdot \frac{V_T}{V_0} \tag{S9}$$

$$d_f = \sqrt{\frac{4 \cdot \phi_T \cdot Q}{\pi \cdot v_f}} \tag{S10}$$

For a given concentration and hence, a predefined volume fraction ϕ_T of THV in the polymer solution, the fiber diameter d_f is only depending on the flow rate Q and the fiber velocity v_f.

$$d_f = \underbrace{\left(\frac{4 \cdot \phi_T}{\pi \cdot v_f}\right)^{1/2}}_{C} \cdot Q^{1/2} \tag{S11}$$

$$d_f = \underbrace{\left(\frac{4 \cdot \phi_T \cdot Q}{\pi}\right)^{1/2}}_{B} \cdot v_f^{-1/2} \tag{S12}$$

The velocity of the fiber is caused by the extensional gas flow of the compressed air accelerating the polymer solution inside the nozzle or by the drawing speed of the rotating spool stretching the fiber depending on which one is faster.

A connection between the jet velocity and the pressure difference can be made by Bernoulli's equation. For incompressible flows, the specific energy is constant at any arbitrary point along a streamline.

$$\underbrace{e}_{\substack{specific \\ energy}} = \underbrace{\frac{v^2}{2}}_{\substack{specific \\ kinetic \\ energy}} + \underbrace{\frac{p}{\rho}}_{\substack{specific \\ internal \\ energy}} + \underbrace{gz}_{\substack{specific \\ potential \\ energy}} = \text{constant} \tag{S13}$$

p: pressure

ρ: density of solution

g: acceleration due to gravity

z: height (z-coordinate)

Two states are distinguished: one inside the nozzle and the other inside the liquid jet.

$$\underbrace{e_n}_{\substack{specific\ energy \\ inside\ nozzle}} = \underbrace{e_j}_{\substack{specific\ energy \\ inside\ jet}} \tag{S14}$$

$$\frac{v_n^2}{2} + \frac{p_n}{\rho_0} + gz_n = \frac{v_j^2}{2} + \frac{p_j}{\rho_0} + gz_j \tag{S15}$$

When jetting horizontally, the potential energy is not changing ($z_n = z_j$).

$$\frac{v_n^2}{2} + \frac{p_n}{\rho_0} = \frac{v_j^2}{2} + \frac{p_j}{\rho_0} \tag{S16}$$

$$\frac{p_n}{\rho_0} - \frac{p_j}{\rho_0} = \frac{v_j{}^2}{2} - \frac{v_n{}^2}{2} \tag{S17}$$

The velocity inside the nozzle is much smaller than the velocity of the jet.

$$v_n \ll v_j \implies v_j{}^2 - v_n{}^2 \cong v_j{}^2 \tag{S18}$$

$$\frac{\Delta p}{\rho_0} = \frac{1}{2} v_j{}^2 \tag{S19}$$

$$\Delta p = \frac{1}{2} \rho_0 \cdot v_j{}^2 \tag{S20}$$

Δp: pressure difference between nozzle and jet ($\Delta p = p_n - p_j$)

The pressure difference determines the velocity of the jet.

$$v_j = \sqrt{\frac{2 \cdot \Delta p}{\rho_0}} \tag{S21}$$

We assume that the polymer solution is accelerated by the pressure difference first, while the density remains constant, and just afterwards, the evaporation of the solvent starts. Also, the loss of kinetic energy owing to viscous dissipation and surface tension is neglected.[1] Combining eq. (S21) and eq. (S10) gives eq. (S22), which describes the fiber diameter in dependence of the flow rate and the pressure difference applied to the nozzle device.

$$d_f = \left(\frac{8 \cdot \rho_0 \cdot \phi_T{}^2 \cdot Q^2}{\pi^2 \cdot \Delta p} \right)^{1/4} \tag{S22}$$

$$d_f = \underbrace{\left(\frac{8 \cdot \rho_0 \cdot \phi_T{}^2}{\pi^2 \cdot \Delta p} \right)^{1/4}}_{D} \cdot Q^{1/2} \tag{S23}$$

$$d_f = \underbrace{\left(\frac{8 \cdot \rho_0 \cdot \phi_T{}^2 \cdot Q^2}{\pi^2} \right)^{1/4}}_{A} \cdot \Delta p^{-1/4} \tag{S24}$$

Eq. (S22) differs just in the term $\sqrt{\phi_T}$ from the Gañán-Calvo equation[1] (eq. (S26)) for the jet diameter d_j when using the gas dynamic virtual nozzle-principle.

$$d_f = \sqrt{\phi_T} \cdot \underbrace{\left(\frac{8 \cdot \rho_0}{\pi^2 \cdot \Delta p} \right)^{1/4} \cdot Q^{1/2}}_{\substack{Ga\tilde{n}\acute{a}n-Calvo\ equation \\ for\ jet\ diameter\ d_j}} \tag{S25}$$

$$d_j = \left(\frac{8 \cdot \rho_0}{\pi^2 \cdot \Delta p} \right)^{1/4} \cdot Q^{1/2} \tag{S26}$$

The connection between the diameter of the jet and the fiber can also be shown by another simple consideration. The volume of the jet V_j diminishes due to evaporation of acetone.

$$V_f = V_j \cdot \phi_T \tag{S27}$$

$$\left(\frac{d_f}{2}\right)^2 \pi \cdot l_f = \left(\frac{d_j}{2}\right)^2 \pi \cdot l_j \cdot \phi_T \tag{S28}$$

The length of the jet stays constant when the solvent evaporates; just the diameter decreases $(l_f = l_j)$.

$$\implies \quad d_f = \sqrt{\phi_T} \cdot d_j \tag{S29}$$

5.7.3 Nozzle deformation during operation

For the calculation of the velocity inside the nozzle, it was necessary to determine the cross-sectional area of the nozzle. The microfluidic channel was cut orthogonally to the flow direction; subsequently, the width n_w and the height n_h of the nozzle were measured by SEM (see Table 1). However, as seen in Fig. S1, the PDMS channels are expanding when a pressure difference or flow rate is applied. The width of the nozzle could be measured during operation by means of an optical microscope. By applying the same expansion coefficient of the nozzle width to the nozzle height, the cross-sectional area during operation could be approximated (1037 µm²).
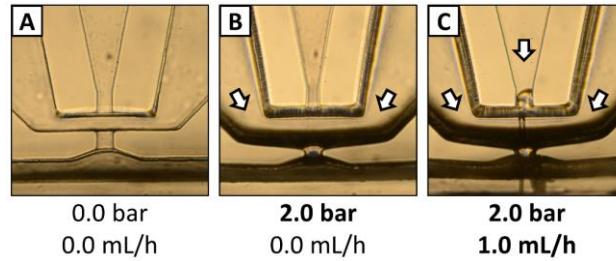
Figure S1: The microchannels of the nozzle are deforming during operation, since the device is made of PDMS elastomer. (A) Idle state, (B) with 2 bar pressure applied, (C) during operation with 1 mL/h and 2 bar.

5.7.4 Influence of working distances between nozzle and spool

The working distance d_s influences the fiber morphology rather than the fiber diameter. The distance d_s between the microfluidic chip and the spool for reeling off was reduced from 8 cm in steps of 1 cm. For a flow rate of 1 mL/h the minimal distance, where a steady fiber with a round cross-sectional shape could be spooled, was 2 cm. At a distance of 1 cm, the fibers fuse and build a network rather than individual fibers (see Fig. S2). Employing the velocity of the jet measured with high-speed cinematography, 3.3 ms are sufficient for the acetone to evaporate from the jetted solution. At flow rates of 2 mL/h and 3 mL/h a distance of 4 cm was needed, which equals a minimal jetting time of 6.5 ms.
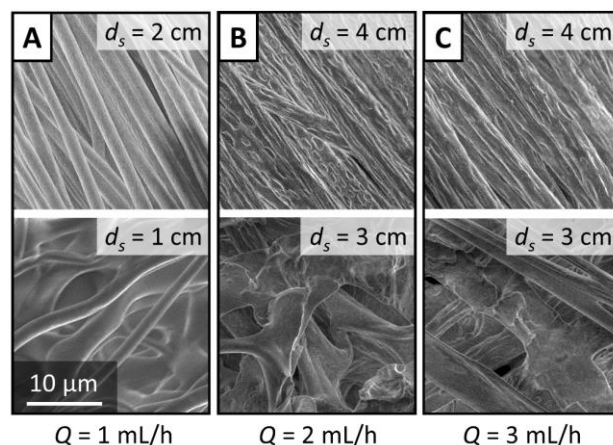
Figure S2: SEM images of bunches of individual fibers (top) and networks of fused fibers (bottom) at different flow rates. The working distance was reduced stepwise until the collected fibers fused into one network. The minimal travel time to form individual fibers could be estimated.

5.7.5 Influence of polymer concentration

The findings of other groups about the influence of polymer concentration on fiber morphology could be confirmed.[2–5] For a solution of a given polymer of a certain molecular weight, a continuous fibrous structure is only obtained above a critical concentration.[2,5] At low polymer concentrations, the formation of beaded fibers is favored.[2] The driving force is the surface tension, which causes oscillations within the jet due to Rayleigh instability.[3,6] Since the viscosity is too low and the chain entanglement density is poor, these oscillations cannot be attenuated.[4] Low surface tension and high evaporation rate would reduce the formation of beads. Higher concentrations also promote the formation of smooth fibers with uniform diameter, as viscoelastic forces retard the deformation of the jet.[3] When the concentration was increased even more, the viscosity got too high to produce fibers by solution blow spinning. Since uniform fibers were desirable for studying the fiber diameter, a reasonable high concentration was used.

Exemplary images for both morphologies can be found in Fig. 5 where the conditions are compared for making beaded and smooth polycaprolactone fibers. The THV fibers showed the same behavior when a solution of less than 20% (w/w) was used. For example, beaded fibers with thin segments of just a few hundred nanometers were obtained at 7–10% (w/w) THV in acetone.

5.7.6 Size distribution of fiber diameter

The uniformity of the fibers is also influenced by varied process parameters. An indicator for the degree of the fluctuation is the standard deviation (SD). Moreover, the relative SD is normalized to the fiber diameter, better illustrating a potential trend since the SD is naturally bigger for thicker fibers.

A close look at Fig. S3 reveals that the size distribution becomes wider when flow rate or drawing speed increases. The histograms confirm this trend which is in accordance to literature.[2] As mentioned before, the solvent needs more time to evaporate from bigger jets, allowing the instabilities to deform the developing fiber in the meantime. An unusually high relative standard deviation was noticed when the pressure difference was quite small being just 1 bar.
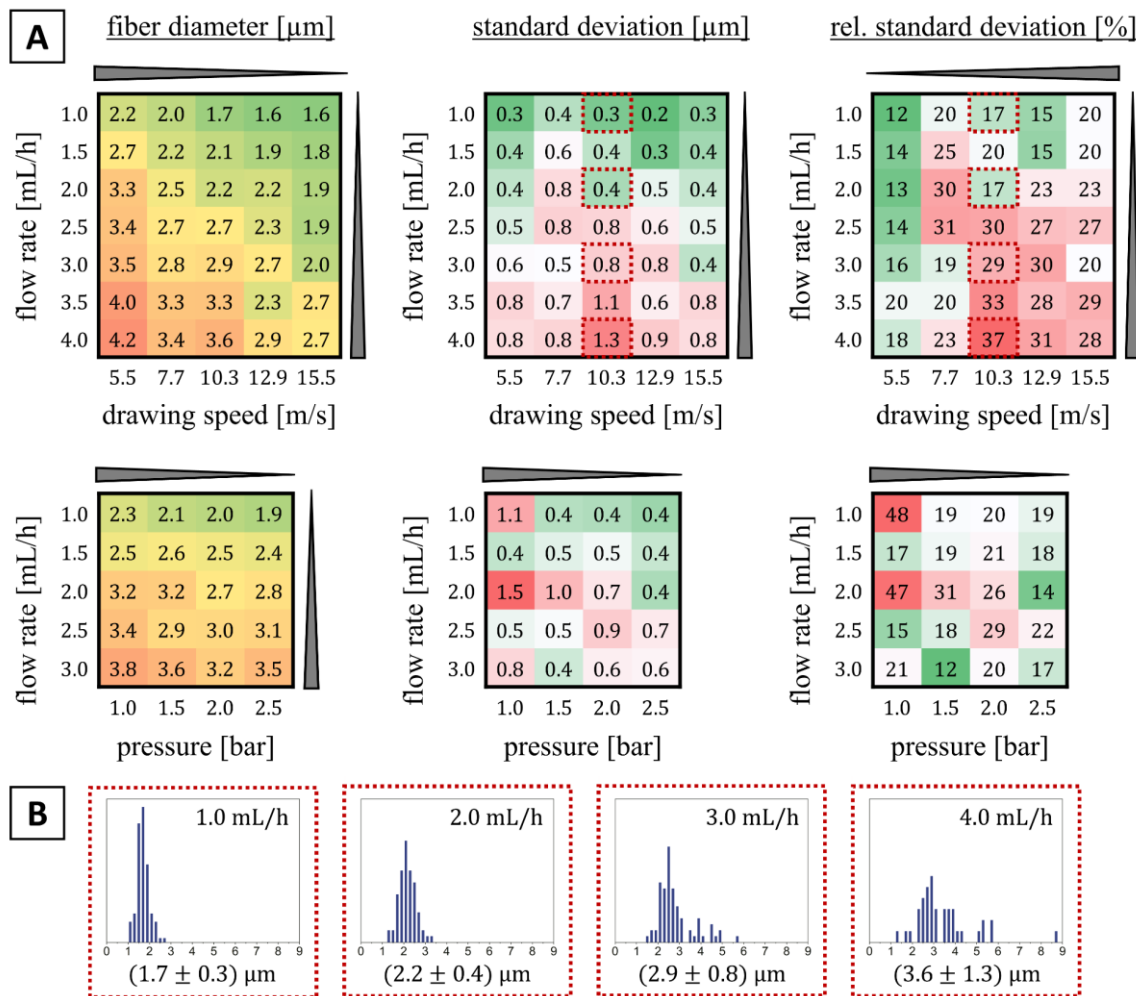
Figure S3: (A) Fiber diameter, standard deviation (SD) and relative SD of the THV fiber samples are presented in color-coded tables. Grey wedges indicate assumed trends in the data. (B) Histograms show exemplarily that the size distribution becomes wider when the flow rate increases. The color code only serves as a guide to the eye to visualize the general trends.

5.7.7   Practical guide for solution blow spinning

Microfluidic solution blow spinning may show similar difficulties as electrospinning since both techniques use a thin liquid jet of polymer solution. The following table lists some hints how to solve typical problems.[7]

Table S1: Some typical problems of solution blow spinning and possible adjustments are summarized in this table.

Problem	Possible solution
Spraying / no fiber at all	Increase weight concentration or molecular weight of the polymer
Formation of a beaded chain	Increase weight concentration
Fluctuating fiber diameter	Increase air pressure and decrease flow rate; decrease drawing speed; increase weight concentration; use another solvent with higher vapor pressure
Fusing of fibers / formation of network or film	Increase working distance between nozzle and collection spool; use another solvent with higher vapor pressure
Polymer solution extrudes from the nozzle	Decrease weight concentration of the polymer
Wetting and clogging of nozzle	Incompatible materials; try to switch polymer, solvent or chip to at least one fluorinated component

5.7.8   Literature

1   A. M. Gañán-Calvo, *Phys. Rev. Lett.*, 1998, **80**, 285–288.

2   J. E. Oliveira, E. A. Moraes, R. G. F. Costa, A. S. Afonso, L. H. C. Mattoso, W. J. Orts and E. S. Medeiros, *J. Appl. Polym. Sci.*, 2011, **122**, 3396–3405.

3   H. Fong, I. Chun and D.H. Reneker, *Polymer*, 1999, **40**, 4585–4592.

4   A. Baji, Y.-W. Mai, S.-C. Wong, M. Abtahi and P. Chen, *Composites Science and Technology*, 2010, **70**, 703–718.

5   S. L. Shenoy, W. D. Bates, H. L. Frisch and G. E. Wnek, *Polymer*, 2005, **46**, 3372–3384.

6   Rayleigh, *Proceedings of the London Mathematical Society*, 1878, **s1-10**, 4–13.

7   S. Agarwal, M. Burgard, A. Greiner and J. H. Wendorff, *Electrospinning. A practical guide to nanofibers*, De Gruyter, Berlin, Boston, 2016.

6 Controlling polymer microfiber structure by micro solution blow spinning[3]

Eddie Hofmann,[a,b] Kilian Krüger,[a,b] Martin Dulle,[a,b] Xiaojian Liao,[c] Andreas Greiner,[c] Stephan Förster[a,b]

[a] Department of Physical Chemistry I, University of Bayreuth, 95440 Bayreuth, Germany.

[b] Jülich Centre for Neutron Science (JCNS-1/ICS-1), Forschungszentrum Jülich GmbH, 52425 Jülich, Germany.

[c] Department of Macromolecular Chemistry II, University of Bayreuth, 95440 Bayreuth, Germany.

6.1 Abstract

Recent progress in microfluidic technology allows fabricating microfluidic devices to produce liquid microjets with unprecedented control of the jet diameter and velocity. Here it is demonstrated that microfluidic devices based on the gas dynamic virtual nozzle principle can be excellently used for micro solution blow spinning to continuously fabricate microfibers with excellent control of the fiber diameter and the internal crystalline alignment that determines the mechanical properties. Fiber spinning experiments with small- and wide-angle X-ray scattering are combined to directly relate the macroscopic spinning conditions to the bulk and molecular structure of the resulting fibers. The elongational rate is shown as the relevant parameter that transduces the nozzle flow conditions to the local macromolecular structure and orientation, and thus the mechanical properties of the resulting fiber. It is observed that the spinning process results in very uniform microfibers with a well-defined shish–kebab crystal structure, which evolves into an extended chain crystal structure upon plastic deformation. Thus, the presented microfluidic spinning methodology has great implications for a precisely controlled production of microfibers using miniaturized spinning devices.

6.2 Introduction

Solution blow spinning (SBS) was introduced by Medeiros *et al.* in the year 2009.[1] By combining conceptual elements from dry spinning, melt blowing and electrospinning, SBS produces micro-scale fibers in a simple one-step process using a small, compact, and portable spinning device.[2,3] In the device, the polymer spinning dope solution is surrounded by a high-velocity air flow and thereby focused into a thin liquid jet. After the evaporation of the solvent, the resulting fiber can either be spooled or collected as a non-woven fabric.[1] The produced nanofiber mats and scaffolds are of great interest for biomedical applications like drug delivery and tissue engineering,[4–6] with the possibility of direct application onto wounds or tissues.[1,7]

Previous investigations on SBS have focused on empirical and qualitative relationships between specific process parameters (gas pressure, flow rate), solution parameters (solvent, polymer solution concentration, molecular weight), and fiber diameter.[1,3,8–11] In a more detailed study, X-ray diffraction was employed to determine crystallinity, *d*-spacing and crystallite size of SBS-produced fibers in comparison to electrospun fibers and casted films.[7] However, a complete and quantitative relation between the main blow spinning parameters and the structure of the resulting fiber is still lacking.

In this study, we use a lithographically produced microfluidic nozzle device to produce fibers at controlled spinning conditions. The design of the microfluidic device was introduced recently.[12] It allows controlling the velocity and diameter of the exiting liquid

jet with high precision. Here we demonstrate using continuous microfluidic solution blow spinning (μSBS) together with small- and wide-angle X-ray scattering (SAXS, WAXS) that this microfluidic device enables unique quantitative control of the spinning conditions to suitably tailor the microfiber diameter and its internal macromolecular alignment. It thus has great implications for a quantitatively controlled production of microfibers using highly miniaturized spinning devices.

6.3 Experimental Section

6.3.1 Fabrication of microfluidic devices

The nozzle devices for μSBS were produced using standard photolithography and soft lithography techniques. The complete procedure was described in detail in a previous publication.[12] By using photolithography, a microstructured master was produced and afterward casted with poly(dimethylsiloxane) (PDMS, Sylgard 184 kit, Dow Corning Corp.). Two individually structured PDMS halves were combined to create a 3D-focusing nozzle device. The nozzle design is schematically shown in Figure 1.

6.3.2 Microfluidic solution blow spinning and sample collection

For the spinning process, a 20% w/w polymer solution of 3M Dyneon THV 221GZ (3M Deutschland GmbH) in acetone was used (η = 1.0 Pa s). This concentration was sufficiently high to achieve stable fiber spinning conditions. The macromolecular structure and thermal properties of the polymer have already been characterized.[13,14] Accordingly, the polymer has a chemical composition of 43.8 mol% tetrafluoroethylene (TFE), 46.0 mol% vinylidene fluoride (VDF), and 10.2 mol% hexafluoropropylene (HFP), a molecular weight of 4100 g mol^{-1}, and a broad melting temperature range between 365 and 400 K. The spinning solution was filled into a glass syringe (1.0 mL, Gastight 1000 Series, Hamilton Company), which was connected via LDPE tubing (0.38 mm I.D., 1.09 mm O.D., Science Commodities Inc.) to the microfluidic nozzle device. Precise pumping of the spinning solution at constant flow rates between 0.5 and 4.0 mL h^{-1} was ensured by using a syringe pump (neMESYS 290N, Cetoni GmbH). Inside the nozzle, the spinning solution was focused by a constant air flow, which was adjusted by a pressure controller with a manometer to a value between 0.5 and 3.0 bar. The fiber spinning was conducted at ambient conditions of 23 °C room temperature and a relative humidity in the range of 45–55%.
Fiber samples were collected on a cork spool driven by a rotary tool (Proxxon GmbH). The distance between nozzle and spool as well as the rotational speed were continuously adjustable. The drawing speed could be calculated by using the diameter of the cork spool (61.8 mm). The advantage of the cork material was that the fibers did not adhere to it and could be bundled easily into a strand of fibers. Several representative images, taken by a

scanning electron microscope (SEM, JSM-6510LV, JEOL GmbH), were statistically analyzed using ImageJ software (National Institutes of Health) to determine the quadratic mean and the standard deviation of the fiber diameter for each sample.

6.3.3 SAXS measurement and tensile testing

The SAXS measurements were performed in-house at a GANESHA (SAXSLAB) instrument equipped with a micro-focusing rotating anode (copper anode, $\lambda = 0.154$ nm, MicroMax 007 HF, Rigaku) and a Pilatus 300K detector (DECTRIS). The fiber samples were measured at a sample-detector distance of 0.44 m.

Using a custom-built tensile apparatus, fiber samples were manually stretched to a certain strain value and fixed for SAXS measurements at constant strains of 50%, 100%, 150%, 200%, 300%, 400%, and 600%. The tensile tests of strands of fibers were performed by using a universal testing machine Zwick/Roell Z0.5 (BT1-FR0.5TN.D14, Zwick GmbH & Co. KG) equipped with a load cell KAF-TC (nominal load: 200 N, Zwick GmbH & Co. KG).

6.4 Results

6.4.1 Principle of microfluidic solution blow spinning

In this study, we investigated the correlation between the spinning parameters and the microstructure of THV fibers obtained from SBS. THV is a fluoroplastic terpolymer, poly(TFE-*co*-HFP-*co*-VDF) composed of TFE, HFP, and VDF. μSBS utilizes the gas dynamic virtual nozzle (GDVN) principle[15] to produce micron-sized fibers from a polymer solution in a continuous and stable process. Inside the nozzle of a microfluidic device a steady flow of pressurized air focuses the polymer solution from orthogonal directions so that a fine liquid jet is produced (Figure 1A). A complete 3Dfocusing is achieved by using a multi-layer architecture of the PDMS device as schematically shown in Figure1B, where the upper half of the microfluidic device is masked out for the image. The pressurized air approaches from all sides and encase the liquid jet entirely. The fabrication of the microfluidic device and the spinning process is described in detail in a previous publication.[12] An SEM image of the spun THV fibers is shown in Figure 1C.

6.4.2 Fiber spinning hydrodynamics

With the developed microfluidic nozzle device, it is possible to uniquely control all parameters that define the molecular and macroscopic fiber properties. The most important parameters are the velocities v and diameters d of i) the solution inside the nozzle, ii) the liquid jet, and iii) the emerging fiber before and iv) after drawing. In the following, we outline the basic equations that relate the velocities to the jet and fiber diameters.
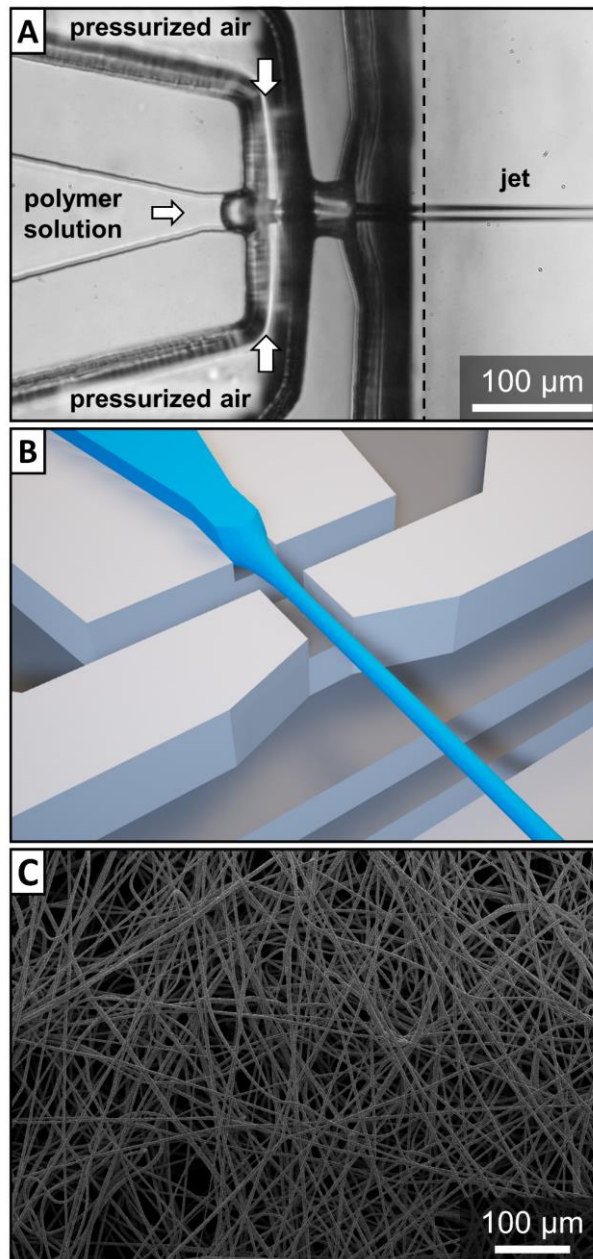
Figure 1: A) Microscopic image and B) 3D model of the nozzle which is used to produce a liquid jet of polymer solution. Due to different focal planes image (A) is composed of two photos indicated by a dashed line. To reveal the 3D architecture of the microfluidic device, just the lower half of the device is shown in image (B). C) SEM-image of the produced fibers.

For incompressible fluids, flow volume conservation relates velocities v and diameters d to the volumetric flow rate Q as

$$Q = A \cdot v = \frac{d^2 \pi \cdot v}{4} \tag{1}$$

where A is the cross-sectional area, which is assumed to be circular with a diameter d. In the experiment the three variable control parameters that determine jet and fiber formation are the volumetric flow rate Q, the pressure difference Δp, and the spooling rotational velocity v_s.

We consider four positions that are relevant for jet and fiber formation: i) the flowing polymer solution in the microfluidic channel just before the channel exit with flow velocity v_n and channel diameter d_n, ii) the free fluid jet after exiting the nozzle with a jet velocity v_j and a jet diameter d_j, iii) the free fiber after evaporation of the solvent with a fiber velocity v_f and a diameter d_f, and iv) the spooled and thereby stretched fiber with a velocity v_s and a final diameter d_s.

i) The flow velocity v_n of the polymer solution in the microfluidic channel exit can be calculated from the channel dimensions as

$$v_n = \frac{Q}{w_n \cdot h_n} \tag{2}$$

where w_n is the width and h_n the height of the channel. Their values are fixed for a given microfluidic device. In the present example the values are $w_n = 34.6\ \mu m$ and $h_n = 30.0\ \mu m$ (Table 1).

ii) The velocity of the free jet is determined by Bernoulli's law as[12]

$$v_j = f_j \cdot \sqrt{\frac{2 \cdot \Delta p}{\rho_0}} \tag{3}$$

where ρ_0 is the density of the solution and Δp the pressure difference. In our setup, the pressure difference could not be measured at the nozzle directly. Experimentally, by using high speed cameras to measure the jet velocity,[12] we found that the free jet velocity is lower due to pressure losses in the tubing, internal friction in the microfluidic device, and viscous dissipation during jet formation, which all reduce the jet velocity. Yet, we found that for a given microfluidic device there is a constant proportionality factor f_j for all pressure differences Δp, which in the present case has a value of $f_j = 0.29$. The jet diameter can then be calculated from Equation 1 as

$$d_j = \left(\frac{8 \cdot \rho_0}{\pi^2 \cdot f_j{}^2 \cdot \Delta p}\right)^{1/4} \cdot Q^{1/2} \tag{4}$$

iii) The volumetric flow rate Q^* after evaporation of the solvent is given by the volume fraction of the polymer in the polymer solution

$$Q^* = \phi_T \cdot Q \tag{5}$$

This leads to a reduction of the diameter of the free fiber d_f

$$d_f = \sqrt{\phi_T} \cdot d_j \tag{6}$$

iv) The spool accelerates the fiber to the new velocity v_s, which results in a final diameter of the spooled fiber

$$d_s = \sqrt{\frac{4 \cdot Q^*}{\pi \cdot v_s}} \tag{7}$$

where the velocity v_s is given by the radius and rotation speed of the spool, that is

$$v_s = d_{spool}\pi \cdot v_{spool} \tag{8}$$

where d_{spool} is the diameter of the spool and v_{spool} the rotational frequency (cycles per second). The relevant equations are summarized in Table 1.

Table 1: Relations between jet and fiber diameters to the flow velocity in each of the four sections relevant for fiber formation.

Section	Diameter	Velocity	Remarks
Nozzle exit	$w_n = 34.6 \ \mu m$ $h_n = 30.0 \ \mu m$	$v_n = \dfrac{Q}{w_n \cdot h_n}$	Diameter set by nozzle design
Free jet	$d_j = \sqrt{\dfrac{4 \cdot Q}{\pi \cdot v_j}}$	$v_j = f_j \cdot \sqrt{\dfrac{2 \cdot \Delta p}{\rho_0}}$	Velocity set by pressure
Free fiber	$d_f = \sqrt{\phi_T} \cdot d_j$	$v_f = v_j$	Assuming complete evaporation
Spooled fiber	$d_s = \sqrt{\dfrac{4 \cdot \phi_T \cdot Q}{\pi \cdot v_s}}$	$v_s = d_{spool}\pi \cdot v_{spool}$	Velocity set by spool

The factor that greatly affects the molecular orientation and the resulting macroscopic fiber properties is the extensional rate

$$\dot{\varepsilon} = \frac{\Delta v}{\Delta x} = \frac{v_s - v_j}{\Delta x} \tag{9}$$

which influences crystallization and crystal orientational order. Δx is the distance over which the emerging, mechanically still susceptible fiber is accelerated, which corresponds to the distance over which solvent evaporates and a solid fiber is formed. It can be calculated as

$$\Delta x = \left(\frac{v_s + v_j}{2}\right) \cdot t_{evap} \tag{10}$$

where t_{evap} is the evaporation time. For spherical droplets it is given by

$$t_{evap} = \frac{d_j^2}{c} \tag{11}$$

where c is a constant given by the evaporation rate of the solvent as (see SI)

$$c = \frac{8 \cdot M \cdot D_v \cdot \Delta p}{\rho \cdot R \cdot T} \approx 8.8 \cdot 10^{-8} \, \frac{m^2}{s} \tag{12}$$

where M is the molecular weight of the solvent (acetone: $M = 58.1$ g mol^{-1}), ρ is the density of the solvent (acetone: $\rho = 0.784$ g mL^{-1}), R is the gas constant (R = 8.314 J K^{-1} mol^{-1}), T is the temperature ($T = 298$ K), and D_v is the diffusivity of the solvent vapor (acetone: $D_v = 1.24 \cdot 10^{-5}$ m^2 s^{-1}). This results in a constant c $\approx 8.8 \cdot 10^{-8}$ m^2 s^{-1}. For cylindrical jets we expect the constant to be smaller, yet still of the same order of magnitude. Thus, for jet diameters in the range of a few micrometers evaporation times are in the millisecond range and with jet velocities in the range of up to 10 m s^{-1} the orientational distance Δx is of the order of tens to hundreds of micrometers and therefore in a relevant range for the experiments.

In terms of the control parameters that are varied in the experiment (Q, Δp, v_{spool}) the extensional rate according to Equations 9–12 is given by

$$\dot{\varepsilon} = \frac{\Delta v}{\Delta x} = \frac{v_s - v_j}{\left(\dfrac{v_s + v_j}{2}\right) \cdot \dfrac{d_j^{\,2}}{c}} \tag{13}$$

Taking into account the proportionalities $d_j^{\,2} \propto \frac{Q}{\sqrt{\Delta p}}$ (Equation 4) and $v_j \propto \sqrt{\Delta p}$ (Equation 3), we obtain the relation

$$\dot{\varepsilon} \propto \frac{v_s - v_j}{v_s + v_j} \cdot \frac{v_j}{Q} \tag{14}$$

which will be considered in the experiments. It shows that for large v_s/v_j ratios and small jet diameters the extensional rates are large. As shown in the Supporting Information, from Equation 14 follows an optimal ratio $\left(v_s/v_j\right)_{max} = r^* = \left(\sqrt{2} - 1\right)^{-1} \approx 2.4$, for which the extensional rate $\dot{\varepsilon}$ has a maximum. We expect that under this condition macromolecular chains will align well along the fiber axis, which should lead to high values of the orientational order parameter of the resulting polymer fiber.

6.4.3   Small-angle X-ray scattering

SAXS was used to study the influence of the spinning parameters on the microstructure of the THV fiber. For the measurements, the fibers were assembled into a filament yarn and were aligned vertically with respect to the X-ray beam. We observe that the obtained 2D scattering patterns show two distinct features,[16] an oval-shaped pattern along the equator, and two diffuse reflections along the meridian, as can be seen in Figure 2A.
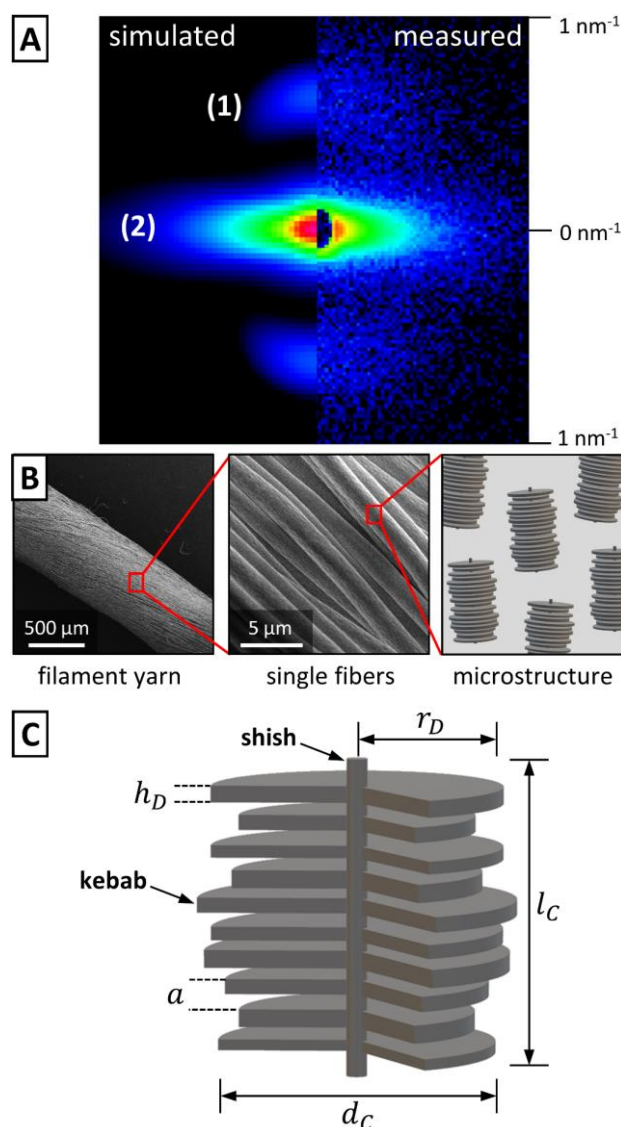
Figure 2: A) Simulated and measured 2D SAXS pattern for THV fibers ($Q = 1$ mL h^{-1}, $v_s = 7.7$ m s^{-1}, $\Delta p = 2.0$ bar, $d_s = 8$ cm); 1) meridional reflection due to lamellar disks perpendicular to fiber axis and 2) equatorial scattering due to cylindrical structure in fiber direction. The maximum scattering vector is $q_{max} = 1.0$ nm^{-1}. B) The shish–kebab model is proposed as morphology of the semicrystalline THV polymer fibers. C) Designation of the structural parameters for the shish–kebab model, which are described in Table S1, Supporting Information.

The equatorial pattern arises from cylindrical or primary fibril structures, which are aligned along the fiber axis. The meridional reflexes originate from stacks of lamellar disks, which are orientated perpendicular to the fiber axis according to the well-known shish–kebab model. The dimensions and orientation of the cylinders and disks are determined by simulating 2D scattering patterns that match the measured 2D-SAXS patterns. For the calculation of the simulated scattering patterns the freely available software *Scatter* was used.[17,18]

The proposed model for the semicrystalline polymer is a shish–kebab structure as schematically shown in Figure 2C.[19] The scattering patterns for the shish–kebab structure

were calculated by assuming a model consisting of thin cylinders, representing the shishs which are oriented in fiber direction, and stacks of disks representing the kebabs. The scattering intensity is then calculated as the sum of the contribution from the cylinders and from the disk stacks as

$$I(\mathbf{q}) = (\Delta b)^2 \rho_N \big(\phi_C F_C^2(\mathbf{q}) + \phi_D F_D^2(\mathbf{q}) S(\mathbf{q}) \big) \tag{15}$$

where Δb is the scattering length difference between the crystalline and the amorphous phase, $F_C(\mathbf{q})$ is the scattering amplitude of the cylinders, $F_D(\mathbf{q})$ is the scattering amplitude of the disks, ϕ_C and ϕ_D are the volume fractions of the cylinders and disks, $\rho_N = N/V$ is the number density of the particles, $S(\mathbf{q})$ is the lattice factor describing the spatial distribution of the disks, and $\mathbf{q}$ is the scattering vector.
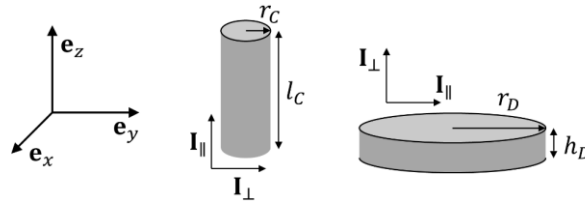
Figure 3: Different shapes used for SAXS pattern calculation together with definition of directions for cylinders and disks to calculate the longitudinal and cross-sectional formfactors.

The scattering amplitude $F_C(\mathbf{q}, \mathbf{l_C}, \mathbf{r_C})$ for cylindrical particles of cross-sectional radius r_C and length l_C can be factorized into[18]

$$F_C(\mathbf{q}, \mathbf{l_C}, \mathbf{r_C}) = F_{C\parallel}(\mathbf{q}, \mathbf{l_C}) \cdot F_{C\perp}(\mathbf{q}, \mathbf{r_C}) \tag{16}$$

where $F_{C\parallel}(\mathbf{q}, \mathbf{l_C})$ is the longitudinal contribution parallel to the cylinder axis, and $F_{C\perp}(\mathbf{q}, \mathbf{r_C})$ is the contribution from the cross-section of the cylinder. $\mathbf{l_C} = l_C \cdot \mathbf{I}_\parallel$ is a vector with length l_C and a direction given by the unit vector parallel to the cylinder axis $\mathbf{I}_\parallel$. $\mathbf{r_C} = r_C \cdot \mathbf{I}_\perp$ is a vector with length r_C and a direction given by the unit vector perpendicular to the cylinder axis $\mathbf{I}_\perp$. The directions are shown in Figure 3. The longitudinal and cross-sectional contributions for cylinders are given by

$$F_{C\parallel}(\mathbf{q}, \mathbf{l_C}) = \frac{\sin(\mathbf{q} \cdot \mathbf{l_C}/2)}{\mathbf{q} \cdot \mathbf{l_C}/2} \tag{17}$$

$$F_{C\perp}(\mathbf{q}, \mathbf{r_C}) = \frac{2 \cdot J_1(\mathbf{q} \cdot \mathbf{r_C})}{\mathbf{q} \cdot \mathbf{r_C}} \tag{18}$$

where $J_1(z)$ is the Bessel function of the first kind.

The structure of disks can be described by their lateral radius r_D and the thickness h_D as shown in Figure 3. The longitudinal and cross-sectional contributions for the disks are given by

$$F_D(\mathbf{q}, \mathbf{h_D}, \mathbf{r_D}) = F_{D\parallel}(\mathbf{q}, \mathbf{r_D}) \cdot F_{D\perp}(\mathbf{q}, \mathbf{h_D}) \tag{19}$$

where $F_{D\parallel}(\mathbf{q}, \mathbf{r_D})$ is now the contribution in the lateral direction and $F_{D\perp}(\mathbf{q}, \mathbf{h_D})$ is the contribution from the cross-section of the disk. The normal and cross-sectional contributions for disks are

$$F_{D\parallel}(\mathbf{q}, \mathbf{r_D}) = \frac{2 \cdot J_1(\mathbf{q} \cdot \mathbf{r_D})}{\mathbf{q} \cdot \mathbf{r_D}} \tag{20}$$

$$F_{D\perp}(\mathbf{q}, \mathbf{h_D}) = \frac{\sin(\mathbf{q} \cdot \mathbf{h_D}/2)}{\mathbf{q} \cdot \mathbf{h_D}/2} \tag{21}$$

The structure factor is given by

$$S(\mathbf{q}) = 1 + \beta(\mathbf{q})(Z(\mathbf{q}) - 1)G(\mathrm{q}) \tag{22}$$

where $\beta(\mathbf{q}) = \langle F(\mathbf{q}) \rangle^2 / \langle F^2(\mathbf{q}) \rangle$, $G(\mathrm{q})$ is the Debye-Waller factor, and $Z(\mathbf{q})$ is the lattice factor. For a simple 1D periodic stacking of disks, the lattice factor is given by

$$Z(\mathbf{q}, \mathbf{g_h}) = \frac{2\pi}{a} \sum_{h=1}^{\infty} L_h(\mathbf{q}, \mathbf{g_h}) \tag{23}$$

where a is the repeat distance of the disk stack, h the Miller index, and $\mathbf{g_h} = \frac{2\pi}{a}\mathbf{a}^*$, where $\mathbf{a}^*$ is the reciprocal lattice vector in the stack direction.

For the calculation of the scattering patterns the form factors were averaged over the distribution of lengths l_C and radii r_C the for the cylinders, and over the distribution of the disk radii r_D and thicknesses h_D for the disks. The form factors and structure factors were further averaged over an orientational distribution with the mean direction parallel to the fiber direction. Details of the calculations are outlined in the Supporting Information and in ref. 18. From the orientational distribution function that describes the scattering patterns quantitatively we derive the orientational order parameter S, which is defined as

$$S = \frac{1}{2} < 3\cos^2\theta - 1 > \tag{24}$$

The experimentally determined values of the order parameter can then be directly related to the flow conditions during fiber spinning. The measured and simulated SAXS patterns together with a table of fit parameters is provided in the Supporting Information.

6.4.4   Fiber spinning and orientational order

In the experiments we clearly observe increasing alignment of the crystalline domains for high draw ratios v_s/v_j. This is observed in the measured SAXS patterns shown in Figure 4, and summarized in Table 2, where for a constant jet velocity v_j the drawing speed v_s was varied. At draw ratios $v_s/v_j > 2$ values of the orientational order parameter of up to $S = 0.95$ can be achieved. This draw ratio value is in good agreement with the value of $r^* \approx 2.4$, for which a maximum elongational rate is calculated. The full set of scattering patterns together with the simulated patterns is compiled (Figures S1–S4, Supporting Information). For draw ratios slightly below 1, the orientational order is clearly decreasing, since the fiber is only stretched for $v_s > v_j$. Similarly, in Tables 3 and 4 results are reported for constant drawing speed, where the pressure difference Δp and thus the jet velocity v_j was varied. Also, here the highest draw ratios resulted in the highest orientational order.
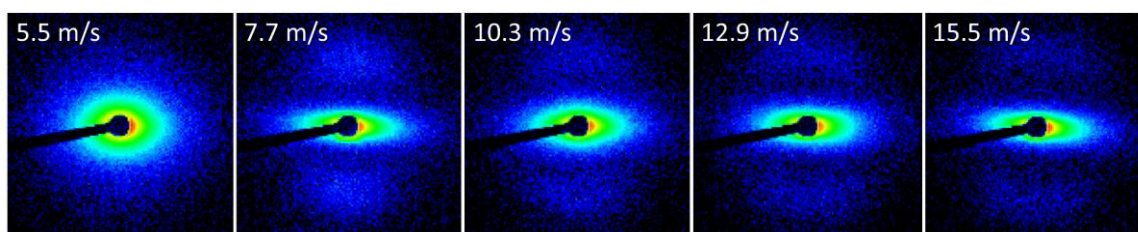
Figure 4: Measured SAXS patterns at increasing drawing speeds v_s, indicated at the upper left of each image, at a flow rate of $Q = 1.5$ mL h^{-1} and a pressure difference of $\Delta p = 2.0$ bar. The increasing drawing speed leads to an increasing anisotropy in the equatorial scattering and the appearance of two broad meridional reflections due to formation of a shish–kebab crystal structure. The maximum scattering vector is $q_{max} = 1.0$ nm^{-1} for all scattering patterns.

Table 2: Orientation parameters S of fiber samples at varied drawing speeds v_s and flow rates Q (pressure difference $\Delta p = 2.0$ bar, corresponding to jet velocity v_j of 6.1 m s^{-1}, nozzle-spool distance $d_s = 8$ cm).

drawing speed v_s	5.5 m/s	7.7 m/s	10.3 m/s	12.9 m/s	15.5 m/s
draw ratio v_s/v_j	0.9	1.3	1.7	2.1	2.5
1.0 mL/h	0.79	0.91	0.92	0.94	0.93
1.5 mL/h	0.77	0.90	0.91	0.86	0.92
2.0 mL/h	0.76	0.90	0.90	0.88	0.86
2.5 mL/h	0.77	0.88	0.90	0.92	0.93
3.0 mL/h	0.76	0.90	0.89	0.92	0.94
3.5 mL/h	0.74	0.88	0.88	0.92	0.93
4.0 mL/h	0.74	0.89	0.86	0.93	0.95

Table 3: Orientation parameters S of fiber samples at varied flow rates Q and pressure differences Δp (drawing speed v_s = 7.7 m s^{-1}, nozzle-spool distance d_s = 8 cm).

pressure difference Δp	1.0 bar	1.5 bar	2.0 bar	2.5 bar
jet velocity v_j	4.3 m/s	5.3 m/s	6.1 m/s	6.8 m/s
draw ratio v_s/v_j	1.8	1.5	1.3	1.1
1.0 mL/h	0.92	0.92	0.93	0.90
1.5 mL/h	0.90	0.90	0.86	0.85
2.0 mL/h	0.90	0.89	0.84	0.84
2.5 mL/h	0.89	0.86	0.84	0.84
3.0 mL/h	0.89	0.86	0.84	0.84

Table 4: Orientation parameters S of fiber samples at varied flow rates Q and pressure differences Δp (drawing speed v_s = 5.5 m s^{-1}, nozzle-spool distance d_s = 8 cm).

pressure difference Δp	1.0 bar	2.0 bar	3.0 bar
jet velocity v_j	4.3 m/s	6.1 m/s	7.4 m/s
draw ratio v_s/v_j	1.3	0.9	0.7
1.0 mL/h	0.85	0.82	0.79
2.0 mL/h	0.85	0.80	0.75

The nozzle-spool distance d_s has a major influence on the orientation parameter S and the fiber morphology, because it needs to be sufficiently long to allow solvent evaporation. Below a critical distance of 2 cm for 1.0 mL h^{-1}, respectively 4 cm for 2.0 mL h^{-1} and 3.0 mL h^{-1}, the fibers fuse and form a network rather than individual fibers, because there is insufficient time for the solvent to evaporate from the jetted polymer solution (Figure 5c).[12] Table 5 shows the orientation parameter S for varied nozzle-spool distances d_s at a constant draw ratio x_s of 1.3. If extensional forces are absent while the fiber solidifies, the polymer chains partially lose their orientation.

Table 5: Orientation parameters S of fiber samples at varied flow rates Q and nozzle–spool distances d_s (pressure difference Δp = 2.0 bar, drawing speed v_s = 7.7 m s^{-1}).

nozzle-spool distance d_s	8 cm	6 cm	5 cm	4 cm	3 cm	2 cm	1 cm
1.0 mL/h	0.93	0.89		0.89		0.89	0.79
2.0 mL/h	0.86	0.86		0.86	0.82	0.79	
3.0 mL/h	0.86	0.86	0.86	0.79	0.79		

Figure 5 illustrates schematically the solidification and orientation process during solvent evaporation and fiber formation. Orientation occurs in the liquid jet state indicated by the light blue cone in Figure 5. Once the fiber solidifies, it moves with the velocity of the spool v_s and is no longer accelerated. At higher flow rates it takes more time for the solvent

to diffuse to the surface of the bigger jets, as illustrated in Figure 5a–c. Consequently, the distance Δx between the nozzle and the solidification point of the liquid jet increases, leading to a decreasing strain rate $\dot{\varepsilon}$. This effect can be observed for the fiber samples in Tables 2–4, when the nozzle-spool distance stays constant and the flow rate is varied. It is known that high strain rates promote the formation of microfibrils of extended chain crystals, whereas lamellar kebabs of folded-chain crystals are less developed.[20] This can be observed by a less pronounced meridional scattering for higher v_s/v_j-ratios in Figures S1–S3, Supporting Information.
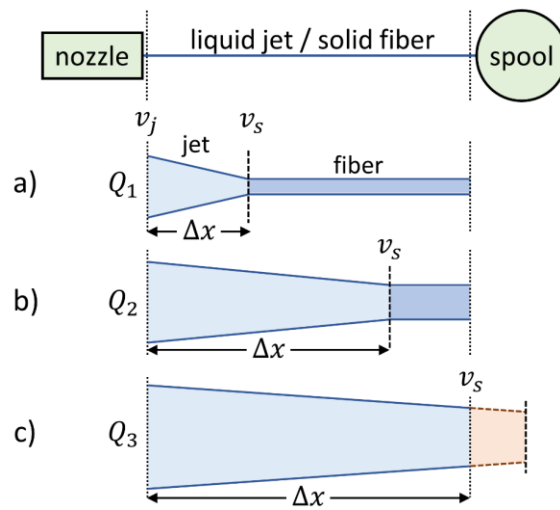
Figure 5: The theoretical progression of the diameter of the jet and subsequently the fiber is shown in this schematic diagram. The initial velocity of the jet v_j and the velocity of the spool v_s remain constant while the flow rate Q is changed ($Q_1 < Q_2 < Q_3$) causing a shift of the solidification of the jetted polymer solution. c) The nozzle–spool distance d_s is not sufficient for a complete evaporation of the solvent at flow rate Q_3.

The quantitative relation between the macroscopic flow parameters that determine the extensional rate (Equation 14) and the degree of molecular orientation of the microfibers is shown in Figure 6. There, the values for the order parameter S determined from the scattering patterns are plotted against $\frac{v_s-v_j}{v_s+v_j} \cdot \frac{v_j}{Q}$ which is proportional to the elongation rate $\dot{\varepsilon}$ as given by Equation 14. We observe that despite noticeable scatter of the data, they seem to indicate a systematic relation. This is indicated by the solid line which shows a constant base level of the orientational order, when there is no additional stretching of the fiber ($v_s < v_j$). For $v_s > v_j$, the orientational order increases until it reaches a nearly constant plateau value of S ≈ 0.94 above a value of $\frac{v_s-v_j}{v_s+v_j} \cdot \frac{v_j}{Q} \approx 1$. This shows that the extensional rate is the central parameter that relates the macroscopic flow parameters to the local macromolecular alignment. This furthermore shows the excellent control of the fiber properties by variation of the three flow parameters v_s, v_j, and Q.
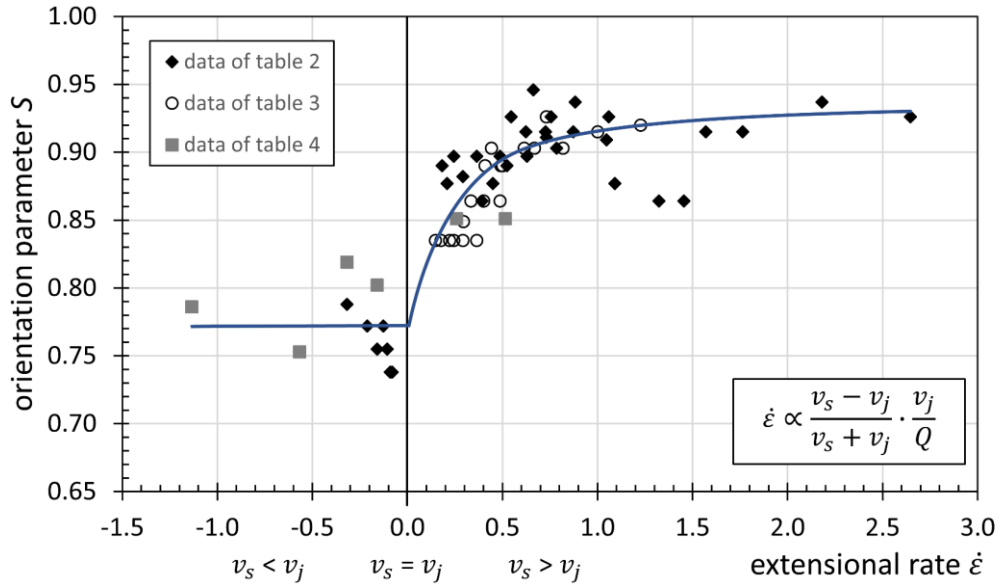
Figure 6: Plot of the orientational order parameter S versus $\frac{v_s-v_j}{v_s+v_j}\cdot\frac{v_j}{Q}$, which is proportional to the elongation rate $\dot{\varepsilon}$ (Equation 14). The values are taken from Tables 2–4. We observe a systematic increase of the orientational order parameter for $v_s > v_j$ until $\frac{v_s-v_j}{v_s+v_j}\cdot\frac{v_j}{Q} \approx 1$, above which a nearly constant plateau value is reached. The line is a guide to the eye.

So far, there have been only a few studies on the structure-property relation of THVs.[21-25] The extensional flow-induced changes of the local macromolecular orientation appears to be very similar to the well-investigated ultra-high molecular weight polyethylene,[26] polycaprolactone,[20] isotactic polypropylene,[27] and poly(vinylidene fluoride) (PV-DF).[28] Chain orientation, crystal nucleation, and growth first lead to the formation of a shish–kebab structure.[19,29,30]

6.4.5 Mechanical and microstructural properties during elongation

The fluorocopolymer THV was selected as a model polymer system because it could be well spun into microfibers from an acetone solution by continuous SBS using the newly developed GDNV microfluidic nozzle device. We observed that elongation is an important factor controlling the macromolecular assembly and alignment of the emerging fiber. We therefore studied the correlation between macroscopic elongation and mechanical response to molecular scale alignment by tensile stress-strain experiments accompanied by SAXS and WAXS. For the tensile experiments, fiber bundles were produced at the optimum spinning conditions to achieve high macromolecular orientation, that is, a flow rate of $Q = 1.0$ mL h^{-1}, a pressure difference of $\Delta p = 2.0$ bar, a drawing speed of $v_s = 7.7$ m s^{-1}, a working distance of $d_s = 8$ cm, with a collection time of $t_c = 300$ s. Every fiber bundle consists of about 37 500 single fibers. The SAXS and WAXS measurements were performed with the fiber bundles fixed at selected strain values.
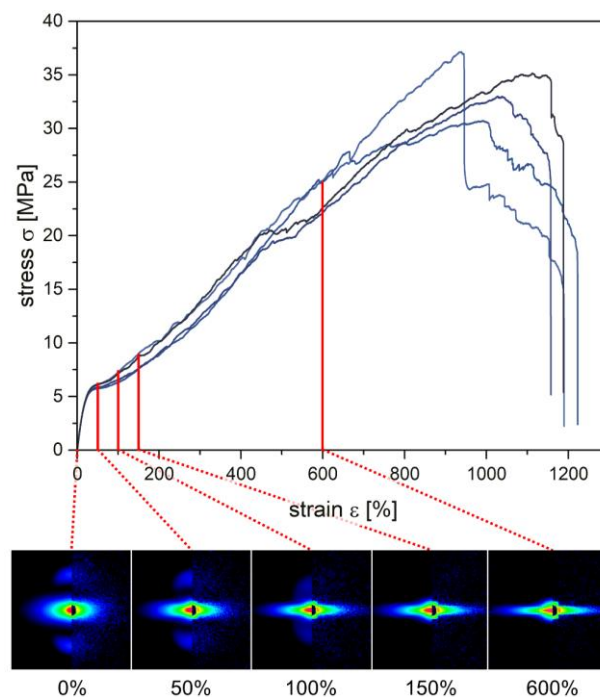
Figure 7: Engineering stress-strain curves for four different fiber bundles together with the SAXS patterns (right: experiment, left: simulation) measured at selected strains. All fiber bundles were produced at the same experimental conditions as described in the main text, leading to high macromolecular orientation.

Fig. 7 shows the measured stress-strain curves for four different fiber bundles together with the SAXS patterns measured at selected strains. From the initial slope we obtain a value of Young's modulus of 31 MPa, which is in a typical range for rubbery materials. At strains >50% we observe a pronounced yielding and plastic deformation behavior, until for strains between 1000–1200% the fibers rupture. The maximum tensile strength is equal to 31 MPa, which is in the typical range of fluoropolymers, that is, between 10 MPa for PTFE and 46 MPa for PVDF. These and further measured mechanical properties are summarized in Table S3, Supporting Information. The mechanical properties are ideal for applications as seal tapes.

Of particular relevance are the observed microstructural changes during deformation, which can be derived from the measured 2D SAXS patterns. The measured SAXS patterns together with the simulated SAXS patterns are shown in the lower panel in Figure 7. The parameters used to simulate the SAXS patterns are summarized in Table S2, Supporting Information. Before elongation, the fibers are characterized by a weak anisotropic equatorial low-q scattering, together with two Bragg peaks located on the meridian and corresponding to the disk or "kebab" lamellar spacing. Upon elongation to 50%, the intensity of the Bragg peaks decreases, while the peak position shifts to lower q. This indicates an increase in the disk spacing together with a disappearance of disks. This results from a transformation of the lamellae of folded chains within the disks into fibrils of

extended chains.[26-28] The increase of the disk spacing is ascribed to the extension of the amorphous layers between the crystalline lamellae of the kebabs.[28]

Further elongation of the fibers to 100–150% leads to a further low-q shift of the Bragg peaks, until they completely vanish. From the model calculations we conclude that the disk spacing increases from 9.8 to 12.0 nm (Table S2, Supporting Information), until the disks have completely disappeared. Concomitantly, the equatorial low-q scattering becomes highly anisotropic and elongated along the equator. This can be related to a reduction of the primary fiber diameter. According to simulations of the low-q scattering, the primary fiber diameter decreases from 62 to 36 nm with a concomitant increase in the order parameter from 0.84–0.99. This indicates that during elongation the shish–kebab structure is transformed into an extended chain crystal structure, which can be plastically deformed up to high elongations.
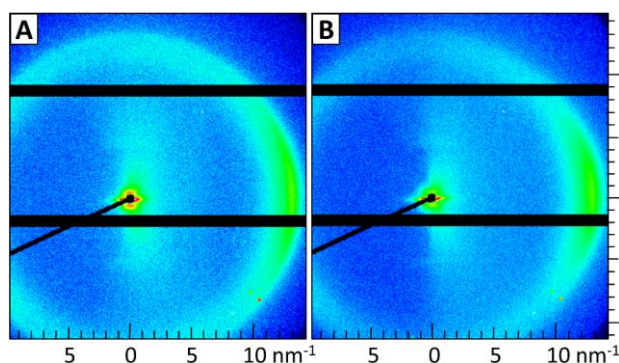
Figure 8: Comparison of WAXS reflex at 13 nm^{-1} for A) an unstretched fiber sample and B) the same sample at a strain of 500%. The reflex on the equator gets more defined. Horizontal black bars result from interstices between detector modules.

The crystallinity in the fibers is apparent by the WAXS. Figure 8 compares the scattering pattern of an unstretched fiber sample (A) to the same sample at a strain of 500% (B). The circular arc at $q = 13$ nm^{-1} corresponds to structural features at a length scale of $d = 2\pi/q \approx$ 0.5 nm, which corresponds well to the cross-sectional dimension of the fluoropolymer backbone. Upon stretching, the arc scattering intensity sharpens toward the equator, indicating an increased crystalline orientation along the fiber axis.

6.5   Conclusions

We developed a microfluidic nozzle device for μSBS to produce uniform microfibers in a highly controlled manner. The method benefits from the GDVN principle, which offers a precise control of the liquid jet diameter and velocity. We performed fiber spinning experiments together with SAXS and WAXS to relate macroscopic spinning conditions to the bulk and molecular structure of the resulting fibers. In our experiments, we demonstrate

that the control provided by the GDVN-microfluidic device enables a precise control of the final fiber diameter and the fiber properties. We show that the elongational rate is the relevant parameter that relates the macroscopic flow properties to the local macromolecular structure and orientation and thus the mechanical properties of the fiber. We observe that the spinning process results in a well-defined shish–kebab crystal structure of the fiber, which evolves into an extended chain crystal structure upon plastic deformation, similar to well-investigated crystalline polymer fibers.

Supporting Information

Supporting Information is available from the Wiley Online Library or from the author.

Acknowledgements

Conflicts of Interest

The authors declare no conflict of interest.

Keywords

microfibers, microfluidics, small-angle X-ray scattering, solution blow spinning

6.6   References

1   E. S. Medeiros, G. M. Glenn, A. P. Klamczynski, W. J. Orts, L. H. C. Mattoso, *J. Appl. Polym. Sci.* 2009, **113**, 2322.

2   J. L. Daristotle, A. M. Behrens, A. D. Sandler, P. Kofinas, *ACS Appl. Mater. Interfaces* 2016, **8**, 34951.

3   J. E. Oliveira, E. A. Moraes, R. G. F. Costa, A. S. Afonso, L. H. C. Mattoso, W. J. Orts, E. S. Medeiros, *J. Appl. Polym. Sci.* 2011, **122**, 3396.

4   X. Zhuang, L. Shi, B. Zhang, B. Cheng, W. Kang, *Macromol. Res.* 2013, **21**, 346.

5   J. E. Oliveira, E. S. Medeiros, L. Cardozo, F. Voll, E. H. Madureira, L. H. C. Mattoso, O. B. G. Assis, *Mater. Sci. Eng., C* 2013, **33**, 844.

6   A. M. Behrens, B. J. Casey, M. J. Sikorski, K. L. Wu, W. Tutak, A. D. Sandler, P. Kofinas, *ACS Macro Lett.* 2014, **3**, 249.

7   J. E. Oliveira, L. H. C. Mattoso, W. J. Orts, E. S. Medeiros, *Adv. Mater. Sci. Eng.* 2013, **2013**, 409572.

8   M. Wojasiński, M. Pilarek, T. Ciach, *Pol. J. Chem. Technol.* 2014, **16**, 43.

9   J. Oliveira, G. S. Brichi, J. M. Marconcini, L. H. Capparelli Mattoso, G. M. Glenn, E. Souto Medeiros, *J. Eng. Fibers Fabr.* 2014, **9**, 117.

10 D. D. da Silva Parize, J. E. de Oliveira, M. M. Foschini, J. M. Marconcini, L. H. C. Mattoso, *J. Appl. Polym. Sci.* 2016, **133**, 43379.

11 D. D. da Silva Parize, M. M. Foschini, J. E. de Oliveira, A. P. Klamczynski, G. M. Glenn, J. M. Marconcini, L. H. C. Mattoso, *J. Mater. Sci.* 2016, **51**, 4627.

12 E. Hofmann, K. Krüger, C. Haynl, T. Scheibel, M. Trebbin, S. Förster, *Lab Chip* 2018, **18**, 2225.

13 S. Ok, B. Hartmann, H. Duran, H. Eickmeier, M. Haase, U. Scheler, M. Steinhart, *J. Polym. Sci., Part B: Polym. Phys.* 2019, **57**, 1402.

14 S. Ok, S. Sadaf, L. Walder, *High Perform. Polym.* 2014, **26**, 779.

15 A. M. Gañán-Calvo, *Phys. Rev. Lett.* 1998, **80**, 285.

16 D. R. Salem, *Structure Formation in Polymeric Fibers*, Hanser Gardner Publications, Cincinnati 2001.

17 S. Förster, L. Apostol, W. Bras, *J. Appl. Crystallogr.* 2010, **43**, 639.

18 S. Förster, S. Fischer, K. Zielske, C. Schellbach, M. Sztucki, P. Lindner, J. Perlich, *Adv. Colloid Interface Sci.* 2011, **163**, 53.

19 R. H. Somani, L. Yang, L. Zhu, B. S. Hsiao, *Polymer* 2005, **46**, 8587.

20 C. T. Lim, E. P. S. Tan, S. Y. Ng, *Appl. Phys. Lett.* 2008, **92**, 141908.

21 J. Stange, S. Wächter, H. Münstedt, H. Kaspar, *Macromolecules* 2007, **40**, 2409.

22 S. Begolo, G. Colas, J.-L. Viovy, L. Malaquin, *Lab Chip* 2011, **11**, 508.

23 H. Teng, *Appl. Sci.* 2012, **2**, 496.

24 S. Ebnesajjad, *Fluoroplastics: The Definitive User's Guide and Databook*, Vol. **2**, 2nd ed., Elsevier, Amsterdam 2015.

25 J. G. Drobny, *Technology of Fluoropolymers*, 2nd ed., CRC Press, Boca Raton, FL 2008.

26 M. An, H. Xu, Y. Lv, Q. Gu, F. Tian, Z. Wang, *RSC Adv.* 2016, **6**, 51125.

27 F. Zuo, J. K. Keum, X. Chen, B. S. Hsiao, H. Chen, S.-Y. Lai, R. Wevers, J. Li, *Polymer* 2007, **48**, 6867.

28 H. Guo, Y. Zhang, F. Xue, Z. Cai, Y. Shang, J. Li, Y. Chen, Z. Wu, S. Jiang, *CrystEngComm* 2013, **15**, 1597.

29 A. J. Pennings, J. M. A. A. Mark, H. C. Booij, *Kolloid Z. Z. Polym.* 1970, **236**, 99.

30 M. Cakmak, A. Teitge, H. G. Zachmann, J. L. White, *J. Polym. Sci., Part B: Polym. Phys.* 1993, **31**, 371.

6.7 Supporting Information

6.7.1 Derivation of the optimum velocity ratio

We start by Eq. (14) which describes the proportionality between the elongation rate $\dot{\varepsilon}$, the spool velocity v_s , and the liquid jet velocity v_j as

$$\dot{\varepsilon} = \frac{v_s - v_j}{v_s + v_j} \cdot \frac{v_j}{Q} \tag{S1}$$

Taking the derivative with respect to v_j yields:

$$\frac{\partial \dot{\varepsilon}}{\partial v_j} = \frac{v_s^2 - 2 v_s v_j - v_j^2}{Q \cdot \left(v_s + v_j\right)^2} \tag{S2}$$

Setting the derivative to zero yields the solution $v_{j,m} = v_s\left(\pm\sqrt{2} - 1\right)$, from which the optimal ratio can be calculated:

$$r^* = \frac{v_s}{v_{j,m}} = \frac{1}{\sqrt{2} - 1} \sim 2.41 \tag{S3}$$

6.7.2 Evaporation times

The solvent evaporation time is a decisive parameter. The rate of decrease of the diameter D of a spherical drop in air due to evaporation can be described by

$$\frac{\mathrm{d}D}{\mathrm{d}t} = \frac{-4 \cdot M \cdot D_v \cdot \Delta p_v}{D \cdot \rho \cdot \mathrm{R} \cdot T} \tag{S4}$$

where M is the molar mass of the evaporating liquid, ρ is the density of the liquid, D_v is the diffusion coefficient for the solvent vapor, $\mathrm{R} = 8.3144$ J/K·mol is the gas constant, T the temperature (298 K), and Δp_v the difference of the vapor pressure between drop surface and ambient atmosphere. For acetone $M = 0.05808$ kg/mol, $\rho = 784$ kg/m^3, $D_v = 1.24 \cdot 10^{-5}$ m^2/s. The vapor pressure p^0 of pure acetone is 30 kPa. Thus, we have for the constant

$$\mathrm{a} = \frac{4 \cdot M \cdot D_v \cdot \Delta p_v}{\rho \cdot \mathrm{R} \cdot T} \approx 4.4 \cdot 10^{-8} \, \frac{\mathrm{m}^2}{\mathrm{s}} \tag{S5}$$

assuming $\Delta p_v \sim p^0$.

Eq. (S4) can be solved to obtain the lifetime of the droplet to be

$$t = \frac{D^2}{2\mathrm{a}} \tag{S6}$$

which gives Eq. (11) for c $= 2$a.

Thus, for a 10 μm diameter droplet we would expect an evaporation time of 1.1 ms. We will see that due to the presence of solvent vapor around the fiber Δp_v is reduced by a factor of ~10, which gives with Eq. (11) a consistent description of the solvent evaporation times under all experimental conditions.

6.7.3 Calculation of scattering patterns

As outlined in the main text, the scattering intensity is calculated as the sum of the contribution from the cylinders and from the disk stacks as

$$I(\mathbf{q}) = (\Delta b)^2 \rho_N \left(\phi_C \langle\langle F_C^2(\mathbf{q}) \rangle\rangle_{or} + \phi_D \langle\langle F_D^2(\mathbf{q}) S(\mathbf{q}) \rangle\rangle_{or} \right) \tag{S7}$$

Where the average $\langle ... \rangle$ denotes the average over the particle size distribution, $\langle ... \rangle_{or}$ denotes the average over the orientational distribution.

For the calculation of the averages over the size distribution of lengths l_C, thicknesses h_D, and radii r_C and r_D, the scattering amplitudes can be factorized and integrated with respect to each of the variables $X = l_C, h_D, r_C, r_D$. In many cases, the Schulz-Zimm distribution is a useful size distribution function. Then the measured z-averages of the functions $f(q, X)$ are given by

$$\langle f(q, X) \rangle_X = \int_0^\infty f(q, X) X^m h(X) \mathrm{d}X \tag{S8}$$

with

$$h(X) = \frac{(z+1)^{z+m+1} X^z}{\bar{X}^{z+m+1} \Gamma(z+m+1)} \exp\left[-(z+1)\frac{X}{\bar{X}} \right] \tag{S9}$$

with m the weighting factor for the variable X, the average $\bar{X}$, and the relative standard deviation $\sigma_x = (z+1)^{-1/2}$. The distribution is normalized such that $\int_0^\infty X^m h(X) \mathrm{d}X = 1$. The weighting factor relates to the measured intensity being the z-average, such that for spheres $m = 6$, for cylinders $m = 2$ for the length, and $m = 4$ for the cross-sectional radius, and for disks $m = 2$ for the thickness and $m = 4$ for the lateral disk radius.

The orientational distribution of the particles can be obtained by averaging the scattering amplitudes $\langle F_C(\mathbf{q}, \mathbf{l_C}, \mathbf{r_C}) \rangle_{l_C, r_C}$, $\langle F_C^2(\mathbf{q}, \mathbf{l_C}, \mathbf{r_C}) \rangle_{l_C, r_C}$, $\langle F_D(\mathbf{q}, \mathbf{h_D}, \mathbf{r_D}) \rangle_{h_D, r_D}$ and $\langle F_D^2(\mathbf{q}, \mathbf{h_D}, \mathbf{r_D}) \rangle_{h_D, r_D}$ over a distribution of angles β between the cylinder axis or lateral direction of the disk, $\mathbf{I}_\parallel$, and the scattering vector $\mathbf{q}$. The relevant scalar products are $\mathbf{q l_C} = l_C \mathbf{q I}_\parallel = q l_C \cos\beta$, $\mathbf{q r_C} = r_C \mathbf{q I}_\perp = q r_C \sin\beta$, $\mathbf{q h_D} = h_D \mathbf{q I}_\perp = q h_D \cos\beta$ and $\mathbf{q r_D} = r_D \mathbf{q I}_\parallel = q r_D \sin\beta$. The orientational averages are then calculated as:

$$\langle \langle F_C(\mathbf{q}, \mathbf{l_C}, \mathbf{r_C}) \rangle^2_{l_C, r_C} \rangle_{or}$$

$$= \int_0^{\pi/2} \langle F_{C\parallel}(q l_C \cos\beta(\delta)) \rangle^2_{l_C} \langle F_{C\perp}(q r_C \sin\beta(\delta)) \rangle^2_{r_C} h(\delta) \sin\delta \, d\delta \qquad (S10)$$

$$\langle \langle F_C^2(\mathbf{q}, \mathbf{l_C}, \mathbf{r_C}) \rangle_{l_C, r_C} \rangle_{or}$$

$$= \int_0^{\pi/2} \langle F_{C\parallel}^2(q l_C \cos\beta(\delta)) \rangle_{l_C} \langle F_{C\perp}^2(q r_C \sin\beta(\delta)) \rangle_{r_C} h(\delta) \sin\delta \, d\delta \qquad (S11)$$

$$\langle \langle F_D(\mathbf{q}, \mathbf{h_D}, \mathbf{r_D}) \rangle^2_{h_D, r_D} \rangle_{or}$$

$$= \int_0^{\pi/2} \langle F_{D\parallel}(q r_D \sin\beta(\delta)) \rangle^2_{r_D} \langle F_{D\perp}(q h_D \cos\beta(\delta)) \rangle^2_{h_D} h(\delta) \sin\delta \, d\delta \qquad (S12)$$

$$\langle \langle F_D^2(\mathbf{q}, \mathbf{h_D}, \mathbf{r_D}) \rangle_{h_D, r_D} \rangle_{or}$$

$$= \int_0^{\pi/2} \langle F_{D\parallel}^2(q r_D \sin\beta(\delta)) \rangle_{r_D} \langle F_{D\perp}^2(q h_D \cos\beta(\delta)) \rangle_{h_D} h(\delta) \sin\delta \, d\delta \qquad (S13)$$

Details of this calculation are outlined in Ref. 16 of the main publication.

For the calculations we need to specify the orientational distribution of the cylinders and disks, $h(\delta)$, which is defined by the angle δ between a director given by the unit vector $\mathbf{n}$ and the direction $\mathbf{I}_\parallel$. For the distribution $h(\delta)$ simple approximations can be made which involve Gaussian, Onsager, Boltzmann, or Maier-Saupe distribution functions. These functions are given by

$$h(\delta) = \begin{cases} \exp\left[-\sin\delta/\bar{\delta}\right] & \text{, Onsager} \\ \exp\left[-\delta/\bar{\delta}\right] & \text{, Boltzmann} \\ \exp\left[\left(\cos\delta/\bar{\delta}\right)^2\right] - 1 & \text{, Maier-Saupe} \\ \exp\left[-\left(\delta/\bar{\delta}\right)^2\right] & \text{, Gaussian} \end{cases} \qquad (S14)$$

with $0 \le \bar{\delta} < \infty$. A value of 0 corresponds to a uniform orientation of all cylinders in the direction of the director $\mathbf{n}$, whereas a value of $\bar{\delta} \to \infty$ corresponds to an isotropic distribution. If the distribution function is known, the orientational order parameter S is defined as

$$S = \left\langle \left| \frac{3\cos^2 \delta - 1}{2} \right| \right\rangle \tag{S15}$$

For most of the scattering patterns a combination of a Gaussian-type and exponential orientation distribution of the cylinders gave the best agreement between experiment and simulation. An isotropic orientation distribution was assumed for the lamellar disks.

6.7.4   Measured and simulated SAXS patterns

Table S1: Relation between structural parameters and scattering features.

Structural parameter	Symbol	Scattering feature
Length of cylinder	l_C	Width of equatorial scattering along the meridian
Diameter of cylinder	d_C	Guinier slope of equatorial scattering
Thickness of disk	h_D	Height of meridional reflection
Radius of disk	r_D	Azimuthal width of meridional reflection
Lamellar spacing	a	Position of lamellar meridional reflection
Volume fraction	ϕ_C, ϕ_D	Intensity of the respective feature
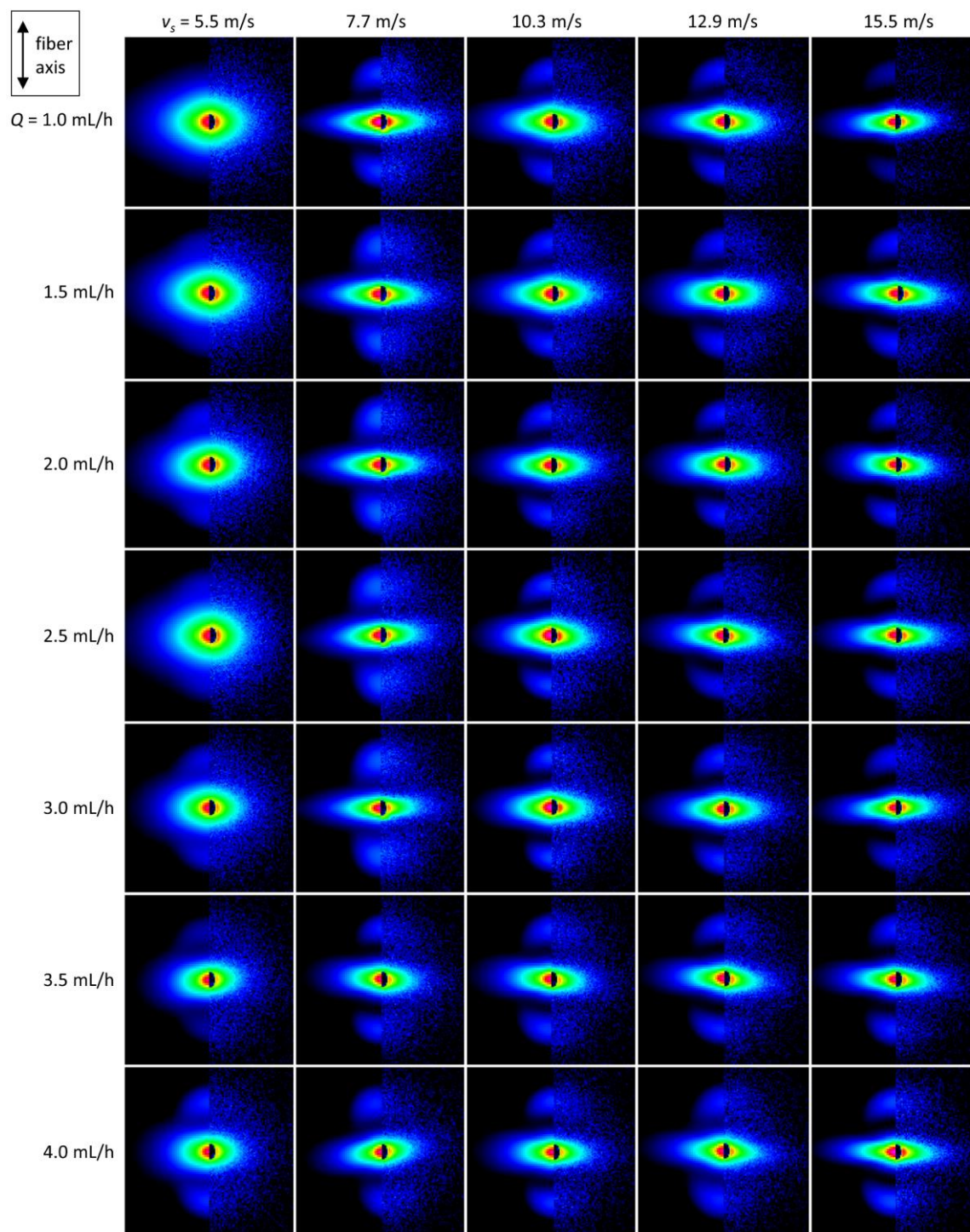
Figure S1: Measured (right) and simulated (left) SAXS patterns to Table 2, pressure difference $\Delta p = 2.0$ bar, jet velocity $v_j = 6.1$ m/s, nozzle-spool distance $d_s = 8$ cm.
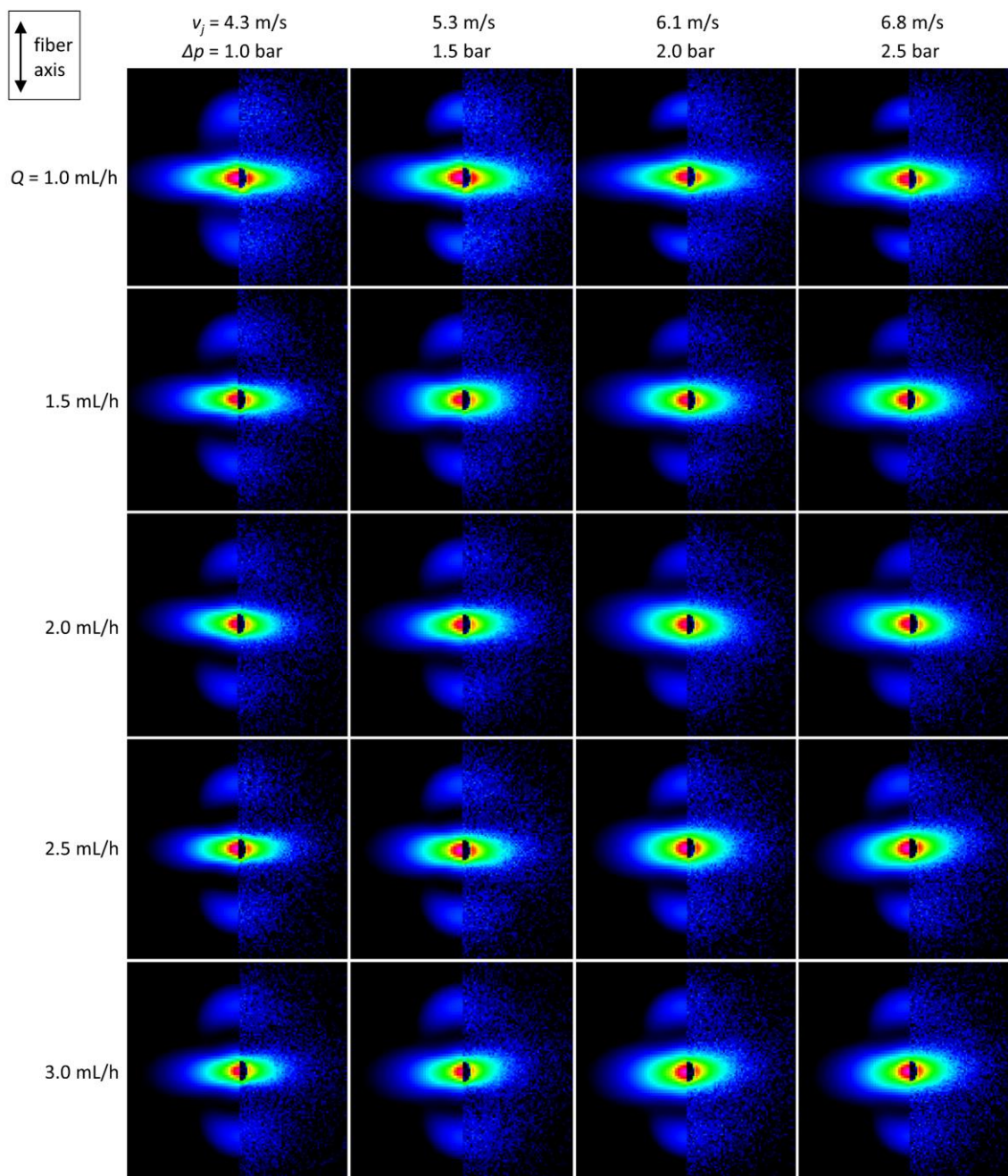
Figure S2: Measured (right) and simulated (left) SAXS patterns to Table 3, drawing speed $v_s = 7.7$ m/s, nozzle-spool distance $d_s = 8$ cm.
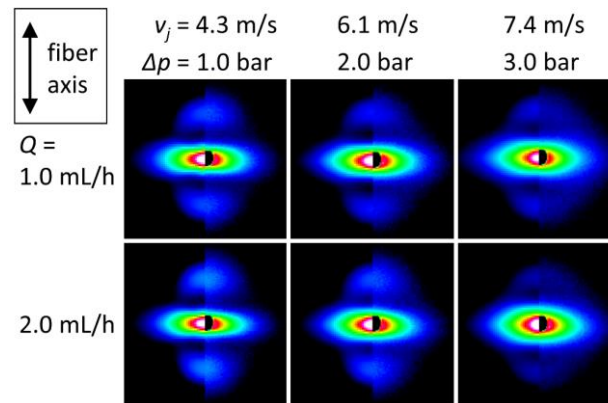
Figure S3: Measured (right) and simulated (left) SAXS patterns to Table 4, drawing speed $v_s = 5.5$ m/s, nozzle-spool distance $d_s = 8.0$ cm.
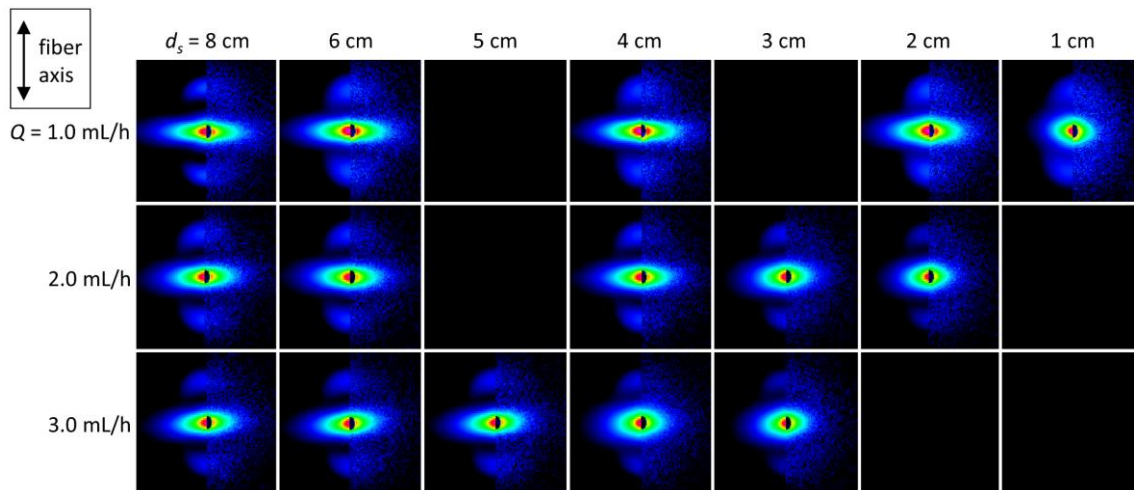
Figure S4: Measured (right) and simulated (left) SAXS patterns to Table 5, pressure difference $\Delta p = 2.0$ bar, drawing speed $v_s = 7.7$ m/s.

6.7.5 SAXS patterns during tensile deformation
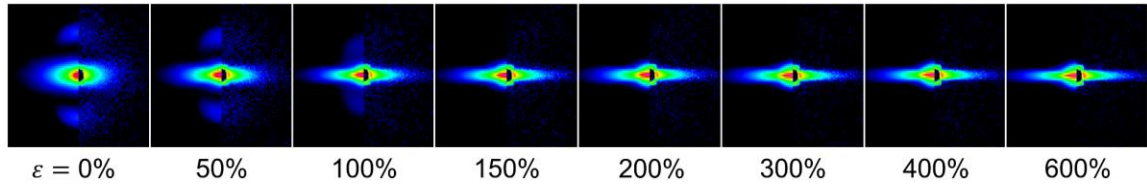
Figure S5: Measured (right) and simulated (left) SAXS patterns during tensile experiments.

Table S2: Parameters for simulation of 2D-SAXS patterns in Fig. 6, which is showing tensile testing of bunches of THV fibers (flow rate $Q = 1.0$ mL/h, pressure difference $\Delta p = 2.0$ bar, drawing speed $v_s = 7.7$ m/s, working distance $d_s = 8$ cm).

strain: ε [%]	0	50	100	150	200	300	400	600
Phase 1 (Gaussian ODF)	0.5	1.0	1.0	1.0	1.0	1.0	1.0	1.0
Phase 2 (lamellar disks)	0.011	0.007	0.004	0.000	0.000	0.000	0.000	0.000
Phase 3 (exponential ODF)	0.5	0.0	0.0	0.0	0.0	0.0	0.0	0.0
cylinder diameter: d_c [nm]	62	47	44	42	40	38	36	36
cylinder length: l_c [nm]	125	300	400	400	450	500	600	600
orientation parameter: S	0.835	0.955	0.978	0.981	0.981	0.984	0.986	0.991
unit cell: a [nm]	9.8	10.5	12.0	0.0	0.0	0.0	0.0	0.0
disk thickness: h_d [nm]	4	4	4	0	0	0	0	0
disk diameter: d_d [nm]	62	47	44	0	0	0	0	0

6.7.6 Mechanical properties of THV fibers

Table S3: Mechanical parameters of tensile tested bunches of THV fibers ($Q = 1.0$ mL/h, $\Delta p = 2.0$ bar, $v_s = 7.7$ m/s, $d_s = 8$ cm, $t_c = 300$ s).

	Young's modulus	max. strain	toughness	tensile strength
	GPa	%	mJ	MPa
mean value	0.0309	1190	332	33
standard deviation	0.0003	27	12	3

Acknowledgements / Danksagungen

Mannschaftskammeraden vom SCR Bayreuth, meine Noobs vom Gaming-Clan der Hardcore Noobs und alle anderen, die mich unterstützt haben und die an dieser Stelle nicht namentlich erwähnt sind. Vielen Dank auch für euer Verständnis, wenn ich mal keine Zeit hatte, etwas mit euch zu unternehmen.

Zum Schluss möchte ich mich bei meiner Familie, meiner Mutter Carmen, meinem verstorben Vater Roland, meiner Schwester Billie und meiner Großmutter Waltraud bedanken, die immer für mich da gewesen sind, mich bei allen Vorhaben unterstützt und immer an mich geglaubt haben.

Mein innigster Dank gilt meiner Frau Isabel für ihren Rückhalt, ihr Verständnis, ihre Nachsicht und die mir entgegengebrachte Liebe. Ich freue mich darauf, nun die nächsten Kapitel in meinem Leben mit dir gemeinsam anzugehen.

Declarations / Erklärungen

(§ 8 Satz 2 Nr. 3 PromO Fakultät)

Hiermit versichere ich eidesstattlich, dass ich die Arbeit selbständig verfasst und keine anderen als die von mir angegebenen Quellen und Hilfsmittel benutzt habe (vgl. Art. 64 Abs. 1 Satz 6 BayHSchG).

(§ 8 Satz 2 Nr. 3 PromO Fakultät)

Hiermit erkläre ich, dass ich die Dissertation nicht bereits zur Erlangung eines akademischen Grades eingereicht habe und dass ich nicht bereits diese oder eine gleichartige Doktorprüfung endgültig nicht bestanden habe.

(§ 8 Satz 2 Nr. 4 PromO Fakultät)

Hiermit erkläre ich, dass ich Hilfe von gewerblichen Promotionsberatern bzw. –vermittlern oder ähnlichen Dienstleistern weder bisher in Anspruch genommen habe noch künftig in Anspruch nehmen werde.

(§ 8 Satz 2 Nr. 7 PromO Fakultät)

Hiermit erkläre ich mein Einverständnis, dass die elektronische Fassung der Dissertation unter Wahrung meiner Urheberrechte und des Datenschutzes einer gesonderten Überprüfung unterzogen werden kann.

(§ 8 Satz 2 Nr. 8 PromO Fakultät)

Hiermit erkläre ich mein Einverständnis, dass bei Verdacht wissenschaftlichen Fehlverhaltens Ermittlungen durch universitätsinterne Organe der wissenschaftlichen Selbstkontrolle stattfinden können.

……………………………………………………………………………………………………

Ort, Datum, Unterschrift